# X-ray diagnostics of ultra compact X-ray binaries

**Filippos Koliopanos**

München 2015

# X-ray diagnostics of ultra compact X-ray binaries

**Filippos Koliopanos**

Dissertation
an der Physik
der Ludwig–Maximilians–Universität
München

vorgelegt von
Filippos Koliopanos
aus Athina, Attiki, Hellas

München, den 13 März 2015

# Contents

# List of Figures

# List of Tables

# Summary

This dissertation is focused on the study of accreting binary systems with compact donors, better known as ultra compact X-ray binaries (UCXBs). We use analytical and numerical methods, along with X-ray observations in order to place constraints on the chemical composition of their donor star. We study a luminosity dependent change of the emission diagram of the accretion column in X-ray pulsar 4U 1626-67 presenting spectroscopic evidence of this phenomenon for the first time.

Ultra-compact X-ray binaries are a subset of low mass X-ray binaries (LMXBs), identified by their extremely short orbital periods of less than 1h. This implies such tight orbits that only hydrogen-depleted, post main sequence, compact objects would fit. Most likely, UCXBs consist of a Roche lobe filling white dwarf, or a helium star that is accreting onto a neutron star companion. Depending on the particular evolutionary path through which UCXBs form, they may have a variety of donors ranging from non-degenerate helium stars to C/O, O/Ne/Mg, or He white dwarfs. It is critically important to distinguish between these possibilities, in order to understand the processes that lead to UCXB formation and control their evolution.

In the second chapter of this dissertation we show that X-ray reflection spectra of UCXBs and in particular the iron K$\alpha$ fluorescent line, can be used as a diagnostic of the chemical composition of their accretion disk and hence the donor star. We show that the most dramatic and easily observable consequence of a C/O-rich accretion disk is the more than tenfold decrease of the strength of the K$\alpha$ line of iron (consistently detected in the spectra of typical LMXBs with main sequence or red giant donors). This is caused by screening of the presence of iron by oxygen – in the C/O dominated material the main interaction process for a $E \approx 7$ keV photon is absorption by oxygen rather than by iron, contrary to the solar composition case. The increase of the equivalent width (EW) of the K$\alpha$ lines of carbon and oxygen, on the

other hand, saturates at rather moderate values. Screening by He is less important, due to its low ionization threshold and because in the accretion disk it is mostly ionized. Consequently, in the case of the He-rich donor, the iron line strength remains close to its nominal value, determined by the iron abundance in the accretion disk. The importance of this effect is demonstrated by analytical calculations in the single scattering approximation and detailed numerical simulations, using Monte Carlo methods. This is the first time X-ray reflection off a C/O or O/Ne/Mg dominated disk has ever been investigated.

In the third chapter we analyze observations of well known UCXBs in order to verify our theoretical predictions and demonstrate the use of our model as a novel method to determine the chemical composition of the donor star in UCXBs. We investigate high resolution spectra of five UCXBs – using archival data from the XMM-Newton orbital observatory – searching for the Fe K$\alpha$ line in their spectra. In the case of two UCXB systems with a donor star of known composition, our analysis was in agreement with the results of our theoretical calculations. We identify the donor star of three more UCXBs, whose chemical composition has never been determined before. This work opens up the prospect for the use of our method, as a tool for determining the nature of the donor star in UCXBs.

In X-ray binaries in which the accretor is a neutron star with a high magnetic field, the accretion disk is disrupted by the strong magnetic field. As a result, it is truncated far away from the neutron star, at a distance of the order of a few$\times 10^3$ stellar radii from the neutron star. The accreting material is then collimated by the magnetic field, towards the magnetic poles of the neutron star. As the gas approaches the surface of the neutron star, it is compressed and heated, forming the so called accretion column. The emission of the accretion column is highly anisotropic. Theoretical calculations showed that at low to moderate luminosity ($L < 10^{37}$ erg/sec) the emission is beamed along the axis of the accretion column. This is known as pencil-beam emission. At higher mass accretion rate and hence higher luminosity (exceeding $\sim 10^{37}$ erg/sec), the emission diagram of the accretion column changes dramatically. Opacity along the magnetic field axis increases significantly and photons can only escape from the sides of the accretion funnel. This results in a beamed emission that is oriented perpendicular to the magnetic field axis and is known as fan-beam emission. As the neutron star rotates rapidly, the beamed emission is observed in the form of characteristic pulses in the light curve of the source. Emission with a pencil-beam pattern is usu-

ally associated with single pulsed light curves, while the fan beam pattern is mostly related with characteristic double peaked pulse profiles.

In the final chapter of this thesis, we discover a luminosity dependent change of the emission diagram in X-ray pulsar 4U 1626-67. Spectroscopic analysis of a recent observation of 4U 1626-67 – using data from simultaneous observations by the Chandra and RXTE space observatories – revealed the presence of a narrow Fe K$\alpha$ emission line. The observation was performed when the source was in a high luminosity ($> 10^{37}$erg/s) state. This feature was not present in earlier observations, performed with XMM-Newton, when the source was in a low luminosity regime. Timing analysis of both sets of data revealed a major change in the pulse profile of the source. The pulse profile during the high luminosity observation has a characteristic double peaked shape that is radically different from the pulse profile during the low luminosity observation when the Fe line was not present. We argue that the appearance of the line and the change in the shape of the pulse profile have a common cause. They are the result of a modification of the emission diagram of the accretion column, from a pencil-beam to a fan-beam dominated pattern, caused by the increase in mass accretion rate. The change in the direction of the beamed emission resulted in increased flux towards the disk, leading to the appearance of the line.

The exceptional spectral resolution of the high energy grating spectrometer aboard Chandra, allowed us to accurately calculate the centroid energy, width and strength of the iron emission line and demonstrate that it originates at a distance of $\sim 2000$ stellar radii, which corresponds to the magnetospheric radius for a field of the order of a few$\times 10^{12}$ G. Lastly, we show that the relative faintness of the iron emission line is consistent with reflection off a C/O rich disk. The latter estimation confirms previously published works that suggested that this source is a UCXB with a C/O white dwarf donor.

# Zusammenfassung

Schwerpunkt dieser Dissertation ist die Untersuchung von akkretierenden Binärsystemen, welche aus zwei kompakten Partnern bestehen, besser bekannt als ultrakompakte Röntgen- doppelsterne oder *ultra compact X-ray binaries*(UCXBs). Analytische und numerische Methoden in Kombination mit Beobachtungen im Röntgenbereich werden benutzt um Rückschlüsse auf die chemische Zusammensetzung des Masse verlierenden Sterns zu ziehen. Die von der Leuchtkraft abhängige Änderung im Emissionsdiagramm der Akkretionssäule des Röntgenpulsars 4U 1626-67 wird untersucht und erstmals ein spektroskopischer Nachweis dieses Phänomens präsentiert.

Ultrakompakte Röntgendoppelsterne sind eine Untergruppe der massearmen Röntgen-doppelsterne (*low mass X-ray binaries*, LMXBs), welche anhand ihrer extrem kurzen Umlaufzeiten von weniger als einer Stunde identifiziert werden. Dies impliziert derart enge Umlaufbahnen, dass nur wasserstoffarme, kompakte Post-Hauptreihenobjekte in Frage kommen. Höchstwahrscheinlich bestehen UCXBs aus einem, die Roche-Grenze ausfüllenden, weißen Zwerg oder einen Heliumstern, der Material an einen Neutronenstern abgibt. Abhän-gig von der jeweiligen Entstehungsgeschichte der UCXBs, können sie verschiedenste Masse verlierende Partner haben: von nicht-entarteten Heliumsternen bis hin zu C/O, O/Ne/Mg- oder He-dominierten weißen Zwergen. Es ist von entscheidender Bedeutung zwischen diesen Möglichkeiten zu unterscheiden, um jene Prozesse zu verstehen, die zur Entstehung eines UCXB führen und seine Entwicklung bestimmen.

Das erste Kapitel dieser Arbeit zeigt, dass Röntgenreflexionsspektren von UCXBs, insbesonders die Eisen-K$\alpha$-Fluoreszenzlinie, als Unterscheidungsmerkmal der chemischen Zusammensetzung der Akkretionsscheibe, und damit des Masse verlierenden Sterns, genutzt werden können. Die drastischste und am leichtesten zu beobachtende Konsequenz einer C/O-reichen Akkretionsscheibe ist die mehr als zehnfache Abschwächung der K$\alpha$-Linie des

Eisens (konsistent in den Spektren typischer LMXBs mit Hauptreihensternen oder roten Riesen als Masse verlierenden Stern nachgewiesen). Diese wird durch die Abschirmung des Eisens durch Sauerstoff verursacht. Im Gegensatz zum Fall solarer Zusammensetzung, ist in der C/O-dominierten Materie Absorption durch Sauerstoff anstatt durch Eisen der dominante Wechselwirkungsprozess für ein Photon mit $E \approx 7\,\mathrm{keV}$. Andererseits erreicht der Anstieg der Äquivalentbreite (*equivalent width*, EW) der K$\alpha$-Linien von Kohlen- und Sauerstoff bei recht moderaten Werten seine Sättigung. Auf Grund seiner niedrigen Ionisationsschwelle und dem Umstand, dass es in der Akkretionsscheibe vorwiegend ionisiert vorliegt, ist die Abschirmung durch Helium von geringerer Bedeutung. Folgerichtig bleibt im Fall des heliumreichen, Masse verlierenden Partners die Stärke der Eisenlinie nah an ihrem nominalen Wert, der durch den Eisenreichtum der Akkretionsscheibe bestimmt ist. Die Bedeutung dieses Effekts wird anhand analytischer Berechnungen in der Näherung einmaliger Streuung und detaillierter numerischer Simulationen unter Verwendung von Monte-Carlo-Methoden demonstriert. Dies ist das erste Mal, dass Röntgenreflexion an C/O- oder O/Ne/Mg-dominierten Scheiben untersucht wird.

Das zweite Kapitel behandelt die Analyse von Beobachtungen von hinlänglich bekannten UCXBs um unsere theoretischen Vorhersagen zu verifizieren und demonstriert den Nutzen unseres Modells als neuartige Methode zur Bestimmung der chemischen Zusammensetzung des Masse verlierenden Sterns in UCXBs. Unter Verwendung von Archivdaten des Satelliten XMM-Newton, werden hochaufgelöste Spektren von fünf UCXBs nach der Fe-K$\alpha$-Linie untersucht. Für zwei UCXB-Systeme mit einem Masse verlierenden Stern bekannter Zusammensetzung stimmt unsere Analyse mit den Ergebnissen unserer theoretischen Berechnungen überein. Die Masse verlierenden Sterne in drei weiteren UCXBs, deren chemische Zusammensetzung niemals zuvor bestimmt wurde, werden ebenfalls identifiziert. Diese Arbeit eröffnet die Möglichkeit unsere Methode zur Bestimmung der Natur des Masse verlierenden Sterns in UCXBs zu nutzen.

In Röntgendoppelsternsystemen, in denen das akkretierende Objekt ein Neutronenstern mit starkem Magnetfeld ist, wird die Akkretionsscheibe durch selbiges zerrissen. Infolgedessen ist die Scheibe in weiter Entfernung vom Neutronenstern, in der Größenordnung einiger $10^3$ Sternradien, abgeschnitten. Das akkretierende Material wird dann durch das Magnetfeld in Richtung der magnetischen Pole des Neutronensterns gebündelt. Während sich das Gas der Oberfläche des Neutronensterns nähert wird es komprimiert

und erhitzt und formt dabei die sogenannte Akkretionssäule. Die Emission der Akkretionssäule ist hochgradig anisotrop. Theoretische Berechnungen haben gezeigt, dass die Emission bei niedriger bis mittlerer Leuchtkraft ($L < 10^{37}$ erg/cm) kollimiert entlang der Achse der Akkretionssäule erfolgt. Dies ist als *pencil beam emission* bekannt. Bei höherer Akkretionsrate und damit höherer Leuchtkraft (über $\sim 10^{37}$ erg/cm) ändert sich das Emissionsdiagramm der Akkretionssäule drastisch. Die Opazität entlang der Magnetfeldachse erhöht sich deutlich und Photonen können nur an den Seiten des Akkretionstrichters entkommen. Dies führt zu einer kollimierten Emission die senkrecht zur Magnetfeldachse ausgerichtet ist, der sogenannten *fanbeam emission*. Auf Grund der schnellen Rotation des Neutronensterns wird die kollimierte Emission in Form charakteristischer Pulse in der Lichtkurve beobachtet. Emission mit einem pencil-beam Muster wird üblicherweise mit einzelnen Pulsen der Lichtkurve assoziiert, während fan-beam Muster meist mit charakteristischen Doppelpulsen in Verbindung gebracht werden.

Das letzte Kapitel dieser Arbeit beschreibt eine von der Leuchtkraft abhängige Änderung des Emissionsdiagramms des Röntgenpulsars 4U 1626-67. Unter Verwendung von Daten simultaner Beobachtungen durch die Weltraumteleskope Chandra und RXTE hat die spektroskopische Analyse von einer vor kurzem erfolgten Beobachtungen von 4U 1626-67 die Anwesenheit einer schmalen Fe K$\alpha$-Linie sichtbar gemacht. Die Beobachtungen wurden durchgeführt, als sich die Quelle in einem Zustand hoher Leuchtkraft ($> 10^{37}$ erg/cm) befand. Als die Quelle in niedrigen Leuchtkraftbereichen lag, war dieses Merkmal in früheren Beobachtungen durch XMM-Newton nicht vorhanden. Eine Analyse des zeitlichen Verlaufs beider Datensätze zeigte eine große Veärnderung im Pulsprofil der Quelle. Das Pulsprofil während der Beobachtungen bei hoher Leuchtkraft hat eine charakteristische Doppelspitzenform, die sich radikal vom Pulsprofil während Beobachtungen bei niedriger Leuchtkraft unterscheidet, als die Fe-Linie nicht vorhanden war. Das Erscheinen der Linie und die Änderung der Form des Pulsprofils haben eine gemeinsame Ursache. Sie sind das Ergebnis einer Änderung des Emissionsdiagramms der Akkretionssäule, von einem pencil-beam- zu einem fan-beam-dominierten Muster, ausgelöst durch einen Anstieg der Akkretionsrate. Die Änderung der Kollimationsrichtung der Emission resultierte in einem gesteigertem Fluss in Richtung der Scheibe, was zum Erscheinen der Linie führte.

Die außergewöhnliche spektrale Auflösung des Hoch-energie-gitter-spektrometers an Bord von Chandra erlaubt die genaue Berechnung von Schwerpunktsenergie, Breite und Stärke der Eisen-Emissionslinie und zeigt, dass diese bei

einer Entfernung von $\sim 2000$ Sternradien ihren Ursprung hat, was dem Magnetosphärenradius für ein Feld der Größenord-nung einiger $10^{12}\,$G entspricht. Schließlich wird gezeigt, dass die relative Schwäche der Eisen-Emissionslinie mit Reflexion an einer C/O-reichen Scheibe konsistent ist. Letztere Abschätzung bestätigt frühere Veröffentlichungen, die nahelegten, dass es sich bei dieser Quelle um ein UCXB mit einem C/O-reichen weißen Zwerg als Masse spendenden Stern handelt.

# Chapter 1

# Introduction

## 1.1   X-ray Astronomy

Since the first detection of X-rays from the Sun's corona in 1949 by Herber Friedman and his group and the first detection of a galactic X-ray source, thirteen years later by Giacconi et al. (1962), X-ray astronomy has revealed some of the most violent and energetic phenomena in the Universe. There is a large variety of physical phenomena and astronomical objects that can be primarily (or exclusively) observed in the X-ray spectrum. Advancements in the instrumentation of X-ray observatories and development of the theoretical description of high energy emission processes have allowed for the study and interpretation of numerous sources, ranging from Supernovae (SN) explosions and accretion of matter on to neutron stars (NS's) or black holes (BH's), to galaxy mergers and hot intergalactic gas emission. In the present dissertation, we study the emission processes of accreting NS's and BH's in binary stellar systems, better known as X-ray binaries (XRBs). Our work focuses on a subset of XRBs, called Ultra Compact X-ray Binaries (UCXBs), including a particularly interesting UCXB that features a pulsating X-ray emission. This last type of source is better known as an X-ray pulsar.

## 1.2   X-ray Binaries

XRBs are binary stellar systems in which a donor star is losing mass, that is being accreted onto an evolved, compact companion, a relativistic star that is either a NS or a BH. Material is predominantly lost through the inner
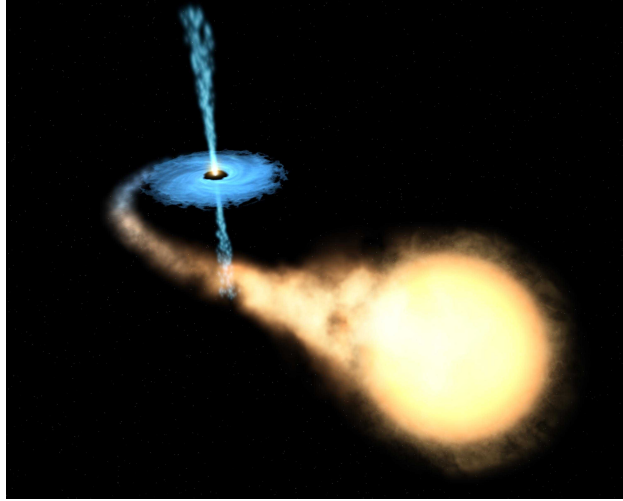
Figure 1.1: An artist's impression of an accreting Low Mass X-ray Binary. The donor star fills its Roche lobe and its material overflows the inner Lagrangian points and accretes on the relativistic star (in this case a black hole). Due to the large angular momentum of the infalling material an accretion disk is formed around the compact object.

Lagrangian point - the point on the line connecting the two stars, where the forces of gravity and the centrifugal force balance each other out. The material of the donor star will flow through this point and will fall into the gravitation potential well of the relativistic star, initiating the process which is called accretion. Due to its large angular momentum, the infalling matter may form an accretion disk around the relativistic object (Fig. 1.1). The classical theory of accretion disks around black holes and neutron stars was developed by Nikolai Shakura and Rashid Sunyaev in 1973. Due to the small size of the relativistic object ($\sim$15 km for a neutron star and $\sim$30 km for a black hole), the gravitational energy released during accretion constitutes a significant fraction of the rest mass energy of the accreting material, typically about 5-20%. This makes these systems very luminous sources of X-ray emission, with luminosities usually ranging from $\sim 10^{34}$ to $\sim 10^{38}$ erg/sec but can exceed $10^{39}$erg/sec (e.g. Bachetti et al., 2014).

Depending on the type of the donor star XRBs are divided into two broad categories each of which contains different subgroups.

- XRBs in which the donor star is a massive star, usually an O or B star,

a Be star, or a blue supergiant, are called High Mass X-ray Binaries (HMXBs). Mass loss from the donor star, in HMXBs, occurs primarily via strong stellar winds. Due to the short lifespan ( $\sim 10^{6-7}$ yrs) of their donors HMXBs are associated with younger stellar populations.

- XRBs in which the donor star is a low mass, main sequence or red giant star are called Low Mass X-ray binaries (LMXBs). Mass loss from the donor star in LMXBs, occurs when the separation between the relativistic object and the donor star becomes comparable to the size of the donor. In this case it may overfill its Roche lobe – the region of space where dynamics of matter are dominated by the gravitational attraction of the star – and starts to transfer its material onto its compact companion, through its inner Lagrangian point. LMXBs are associated with older populations of X-ray sources. UCXBs are a subset of LMXBs, in which the donor star is an evolved star, most likely a white dwarf or a helium star.

Since this work is focused on LMXBs (more precisely UCXBs), we briefly describe the main emission processes and observational characteristics of LMXBs.

## 1.2.1 Emission processes in LMXBs

**Thermal emission**

The primary emission of LMXBs originates in the accretion disk that is formed by in-falling material, around the central compact object. Described by Shakura & Sunyaev (1973) the accretion produces ample amounts of radiation with a broad photon energy range and a spectrum that can be described by a multitemperature black body distribution. The total luminosity of the Shakura-Sunyaev disk scales as L $\sim$ T$^4$ were T is the disk's maximum effective temperature which scales $\sim$ R$_{\text{in}}^{-3/4}$ where R$_{\text{in}}$ is the disk inner radius. Since the inner disk radius can reach all the way to the surface of the NS or the last stable orbit of the BH, it can be as small as a few tenths of km. Therefore, the inner parts of accretion disks in LMXBs, can reach temperatures exceeding $10^6$ K and produce copious amounts of X-ray radiation.

In the case of NS-binaries an extra thermal component may be added to the primary emission. As the rapidly spinning disk reaches the (more) slowly rotating NS, a layer of hot gas – known as the boundary layer – is formed
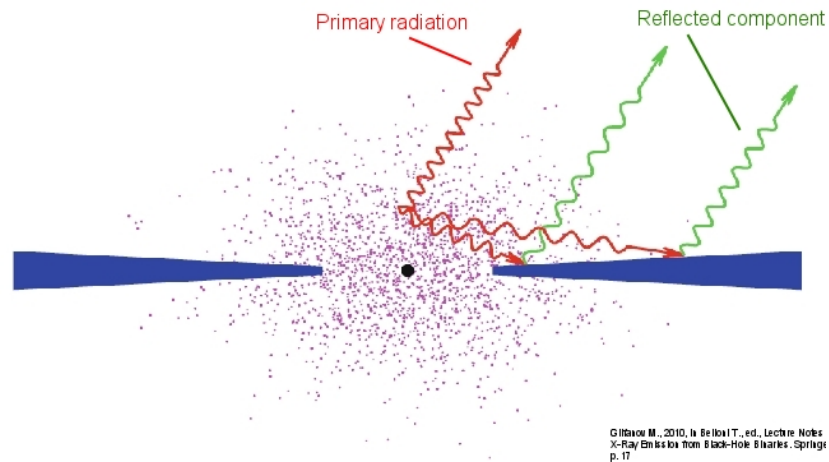
Figure 1.2: A schematic representation of the innermost part ($\sim$1000 gravitational radii) in a low mass X-ray binary in the so called hard state. The inner part of the accretion flow is filled with hot and tenuous, optically thin plasma. Comptonization of the low frequency radiation in the plasma cloud is the main mechanism of the spectral formation in this state. Some fraction of this radiation illuminates the surface of the accretion disk and of the donor star. It is reprocessed by the material of the accretion disk and of the donor star giving rise to the so called "reflected component", depicted in Fig. 1.3. Credit: Gilfanov M., 2010, in Belloni T., ed., Lecture Notes in Physics, Vol. 794, The Jet Paradigm. Springer-Verlag, Berlin, p. 17.

(Sunyaev & Shakura, 1986; Popham & Sunyaev, 2001). The boundary layer is a powerful source of X-ray radiation, with a spectrum that is most often modeled as a black body with a temperature of a few keV. This radiation is a significant component of the X-ray emission of NS-LMXBs, in the so called soft state. The soft state of LMXBs is defined as a phase during which the mass accretion rate increases and thermal emission dominates the observed spectrum. During, the soft state LMXB spectra may also include a less prominent non-thermal, power-law tail component, at energies above $\sim 10$ keV. While this component is energetically insignificant during the soft-state, it dominates LMXB spectra during the so called hard state.

**Non-thermal emission**

During the hard state, emission is dominated by a non-thermal, optically thin component that has a power-law shape. The power law spectrum extends to energies exceeding $50$ keV, before its flux drops exponentially. While the details of the exact mechanism responsible for this phase are still discussed (see e.g. Done, Gierliński & Kubota, 2007, and references therein), the most widely accepted scenario for the origin of the power-law component is thermal Comptonization of soft thermal photons (Sunyaev & Titarchuk, 1980). Namely, in the hard state, the accretion disk is truncated up to $\sim$50-100 Schwarzschild radii away from the relativistic star and gravitational energy is primarily released in a hot inner flow. This results in the formation of a hot diffuse corona with temperatures of the order of $100$ keV. Soft thermal photons originating in the outer parts of the disk, are intercepted by the corona and are subsequently scattered into higher energies by the process of inverse Compton. The resulting spectrum has a power-law shape with a spectral index ranging from $\sim$1.5 to $\sim$2.5, depending on the source parameters. Its high energy exponential cutoff, reveals the temperature of the Comptonizing corona.

**Reflected emission**

A fraction of the emission produced near the compact object illuminates the surface of the accretion disk and the donor star (Fig. 1.2) and is reprocessed by their material. This reprocessed emission is known as the "reflected component". In addition to the continuum produced by the Compton scatterings off electrons in the accretion disk, the reflected component also contains a

number of characteristic emission lines. They are the result of K-shell fluorescence from the different elements present in the accreting material. K-shell fluorescence is the emission of a characteristic (fluorescent) photon, by an atom that has been excited by an incident X-ray photon which is subsequently "absorbed". Namely, if the incident photon is energetic enough it can dislodge a K-shell electron from the atom of a given element. If the resulting vacancy is filled by an electron from another shell, then a fluorescent photon may be emitted. The energy of the fluorescent photon depends on the particular element whose atom is affected as well as its ionization state. Every element produces a K-shell fluorescent photon with a characteristic and well known energy (Bambynek et al., 1972). The shape and relative strength of the emission lines carry information about the geometry of the accretion flow and chemical composition of the accreting material. An example of a reflection spectrum is shown in Fig. 1.3. This particular spectrum was created using our Monte Carlo simulations of disk reflection described in Chapter 2.

When observing LMXBs, the reflected emission is registered along with the primary. Therefore, the reflected component is heavily diluted by the primary emission and the fluorescent lines of most of the elements appear very weak and usually are impossible to detect. Except for the fluorescent line of iron, which in the case of neutral iron is located at 6.4 keV. Thanks to the high fluorescent yield and abundance of iron, this is the brightest spectral feature in an otherwise relatively smooth continuum. The majority of LMXB spectra feature this bright  easily detectable  Fe K$\alpha$ emission line.

## 1.2.2   The case of Ultra Compact X-ray Binaries

There is a small group of XRBs that have orbital periods of less than one hour. So small orbital periods, suggest such tight orbits that a main sequence star (or a red giant) cannot fit. Ultra compact X-ray binary systems are comprised of two evolved, compact stars. The most likely configuration for UCXBs involves a C/O or O/Ne/Mg white dwarf (WD), a He-WD, or a non-degenerate He star, that has filled its Roche lobe and is accreting onto a NS or a BH (Nelson, Rappaport & Joss, 1986; Bildsten & Deloye, 2004).

The extreme environment of two compact degenerate stars orbiting each other at such close proximity, provides an excellent opportunity to study a variety of interesting physical processes. Apart from the fact that UCXBs are expected to be strong gravitational wave sources (e.g. Roelofs et al., 2006),
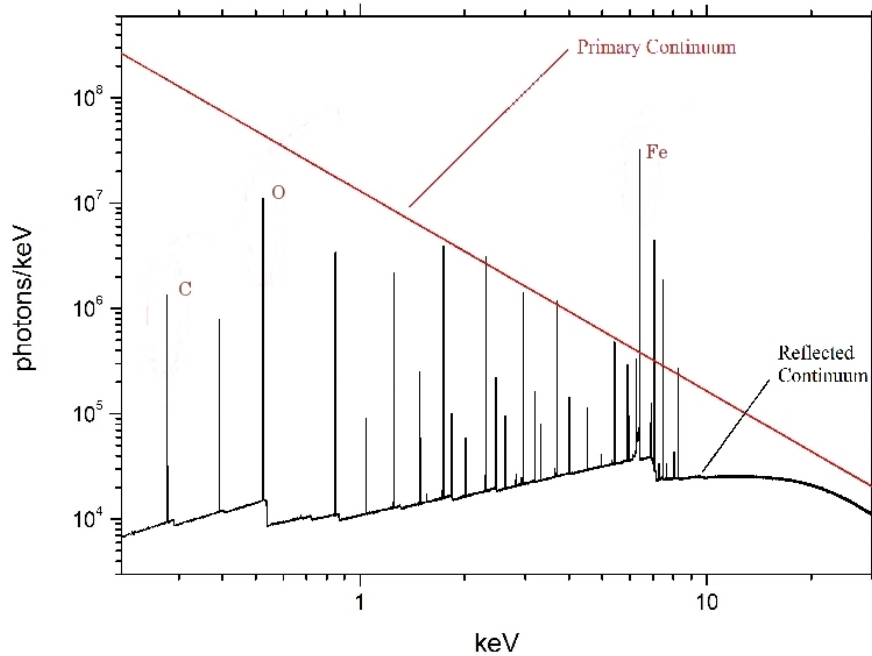
Figure 1.3: The spectrum of the reflected component for an accretion disk of solar abundance. Superposed on top of the reflected continuum produced by Compton scatterings on electrons, are absorption edges and fluorescence lines of various elements. Also shown is the Comptonized continuum produced by the hot plasma cloud in the vicinity of the compact object (see Fig. 1.2). An observer near Earth will observe the sum of the two components.

they are also ideal "laboratories" for the study of binary evolution. Furthermore, as material from the compact donor is accreted onto its companion, we can have a rare view of the interior of evolved, compact stellar remnants.

Depending on which evolutionary path leads to their creation, UCXBs can feature a variety of donors. Ranging from C/O or O/Ne/Mg WDs to He WDs or non degenerate He- stars. Starting life as a close binary system of two hydrogen fusing stars, they go through at least one, most likely two – so called – common envelope phases. Namely, as the more massive star proceeds to the red giant phase, its outer layers expand. Due to its close proximity, the less massive companion is engulfed by the expanding layers. This interaction affects the evolution of both stars. As the less massive star spirals inwards, its massive companion gradually sheds its outer layers, resulting in a system consisting of the core of the giant and a refreshed main sequence companion. If mass transfer begins immediately after the spiral-in, the exposed He core of the massive star becomes the donor star (e.g. Savonije, de Kool & van den Heuvel, 1986). If mass transfer ensues at a later stage, the donor star will evolve into a C/O or O/Ne/Mg WD (e.g. Yungelson, Nelemans & van den Heuvel, 2002). In both cases, due to significant orbital decay, caused by friction-induced angular momentum loss, the resulting binary system will have a much shorter period.

If the less massive star also evolves into the (sub)giant phase, the binary will undergo a second common envelope phase before it becomes a supernova. If the system remains bounded after the less massive star becomes a supernova, it will develop into an accreting binary comprised of a NS or BH accretor and a WD or He-star donor. In figure 1.4 we present an artist's depiction of a known UCXB with the Sun and the Earth included in scale for easy size comparison.

Determining the chemical composition of the donor star in UCXBs is a crucial step towards understanding the details of the evolution of double degenerate systems. This task can be achieved through X-ray and optical spectroscopy, but also indirectly, by studying the sources' bursting activity. The different observational methods are briefly discussed in Chapter 3. The present work focuses on X-ray spectroscopy, and particularly X-ray reflection. We use both theoretical and observational methods to determine the chemical composition of the accretion disk and donor star in UCXBs. Namely, in Chapter 2 we developed an X-ray reflection model, using Monte Carlo techniques, in order to study the effects of different disk abundances on the reflection spectrum. This is the first time in which X-ray reflection
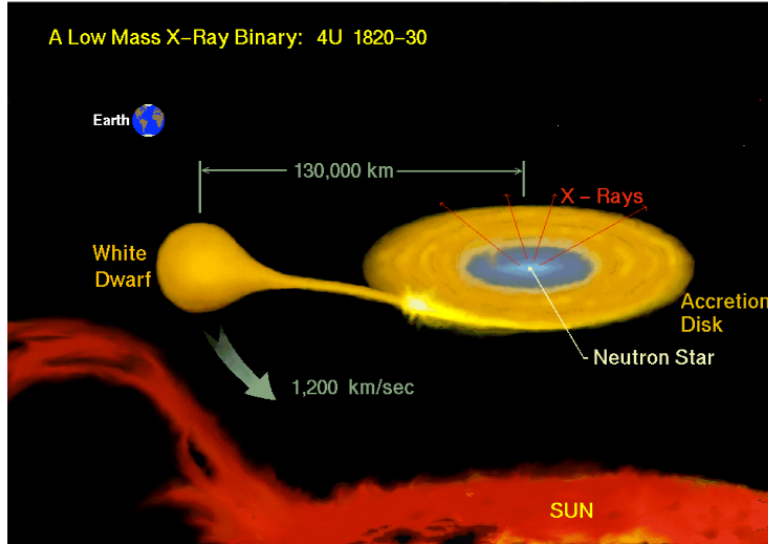
Figure 1.4: Artist's impression of UCXB 4U 1820-30. The Sun and Earth are shown for an easy comparison of size. Figure courtesy: Dany P. Page.

from a hydrogen poor, C/O-rich disk has been modeled. The main features of our code are described in section 1.3. A more rigorous discussion follows in Chapter 2. In Chapter 3 we apply our predictions to X-ray observations of known UCXBs, in order to place constraints on the chemical composition of their accretion disks.

### 1.2.3   X-ray Pulsars

Accreting XRBs in which the compact object is a NS with a high magnetic field are known as X-ray pulsars. Strong magnetic fields (of the order of $10^{12}$ Gauss) are common in younger neutron stars. Therefore, X-ray pulsars are mostly associated with younger populations. In HMXBs, the evolution timescale of the binary is determined by the stellar evolution time scale of the donor star. Since, the donor is a massive star, the time scale will not exceed a few tens of Myrs (Verbunt & van den Heuvel, 1995). On the other hand, evolution of LMXBs is determined by the progression of the loss of the system's orbital angular momentum, or by the stellar evolution of the low mass donor. In both these scenarios the time scale ranges between 1-
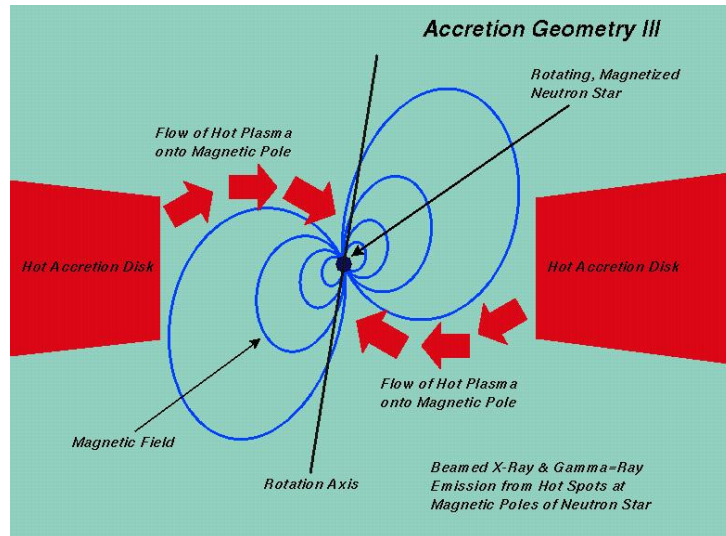
Figure 1.5: Schematic representation of the accretion process in X-ray pulsars. Source: www.astro.msfc.nasa.gov/xray/openhouse/ns/

10 Gyrs (Verbunt & van den Heuvel, 1995). Therefore, HMXBs have the highest likelihood of having a young, high magnetic field NS accretor and so, most X-ray pulsars are also HMXBs. Nevertheless, there at least five known LMXB pulsars (e.g. Bildsten et al., 1997) and one confirmed UCXB pulsar (e.g. Schulz et al.). This unique X-ray pulsar – named 4U 1626-67 – is discussed in the final chapter of this thesis.

The process of accretion onto highly magnetized neutron stars deviates from the "nominal" case of accretion onto black holes and low field neutron stars, described above. When the accretion disk reaches the NS magnetosphere (at a distance of $\sim$ a few$\times 10^3$ stellar radii from the surface of the NS, depending on the strength of the magnetic field) it is disrupted by the strong magnetic field. After this point the accreting gas is channeled by the magnetic field towards the poles of the neutron star. As the gas approaches the magnetic poles it is heated and compressed, forming an accretion column (Figures: 1.5, 1.6).

When the free falling material reaches the surface of the neutron star most of its gravitation energy is released as low energy radiation, mostly via the bremsstrahlung process. The low energy photons are Compton upscattered into X-rays, inside the accretion column (e.g. Lewin, van Paradijs & van den
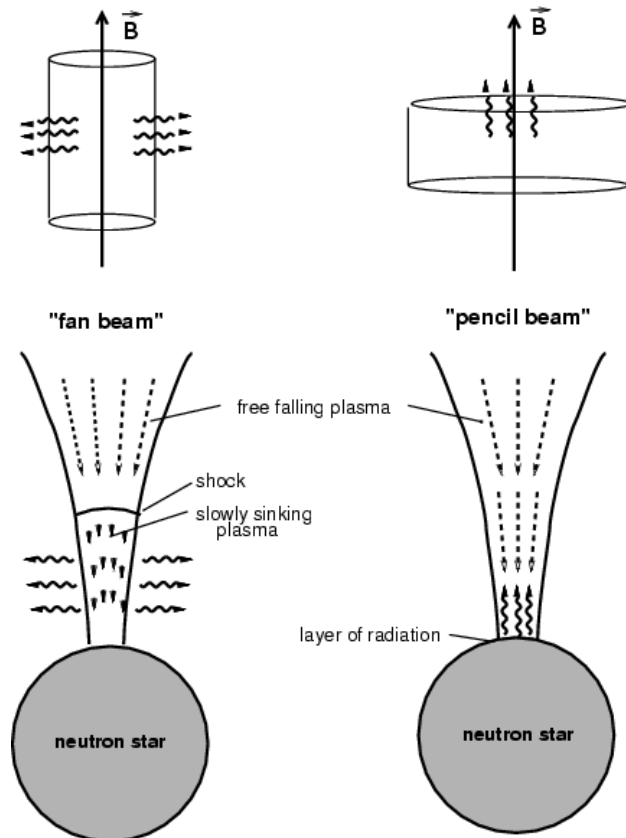
Figure 1.6: A simplified sketch of the accretion column near the surface of the neutron star's polar caps. The drawing depicts the change in the direction of the beamed emission as the the source luminosity exceeds $\sim 10^{37}$erg/sec and the emission diagram changes from a pencil-beam to a fan-beam pattern. Source: Schönherr et al. (2007)
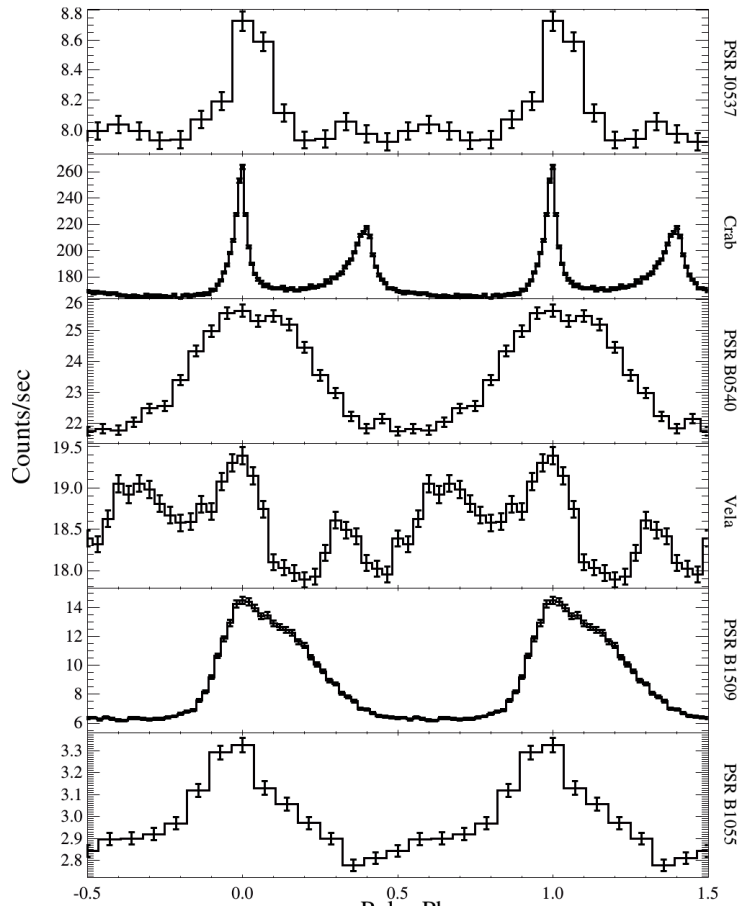
Figure 1.7: A sample of different pulse profile shapes from various X-ray pulsars. Source: Martin-Carrillo et al. (2012)

Heuvel, 1995). Due to the high anisotropy of the scattering cross-sections, in the presence of the high magnetic field, the emission of the accretion column will be strongly beamed. Depending on the mass accretion rate, the beamed emission may be oriented parallel or perpendicular to the magnetic field lines (Fig. 1.6). The emission diagram in these two cases is described by two distinctive patterns, known as pencil-beam emission (when parallel to the field lines) and fan-beam emission (when perpendicular to the field lines). The details of the underlying mechanism, responsible for this behavior, have been established by Basko & Sunyaev (1975, 1976) and are briefly discussed in Chapter 4.

The combination of the neutron star rotation and the beaming of the emission of the accretion column, results in the creation of characteristic pulses in the light curves of these sources. Depending on the direction and the shape of the emission diagram of the accretion column, there can be single or double peaked pulses. Obscuration effects due to the presence of the accreting material, as well as general relativistic effects can further complicate the shape of the pulse profiles (e.g. Mészáros, 1992). This complexity is demonstrated in a sample of different observed shapes of the pulse profiles presented in Fig. 1.7. The shape of the pulse profile can provide valuable insights into the geometry of accretion, the existence of possible obscuring structures or additional emission sources (e.g. accretion hot spots). Combined with an estimation of the luminosity of the source, it can also provide indication for the shape of the emission diagram of the accretion column. Namely, whether it is better described by the pencil-beam or fan-beam scenario. Nevertheless, due to the inherent complexity of the accretion process – which is further convoluted by the presence of the strong magnetic field – the shape of the pulse profile cannot provide anything more than an indication for the emission diagram pattern. In the fourth chapter of this thesis, we discover the appearance of an iron K$\alpha$ emission line, taking place contemporaneously with a major change in the pulse profile of X-ray pulsar 4U 1626-67 and a considerable increase of its luminosity. We show that this combination of events is the strongest confirmation of the fan beam - pencil beam mechanism, discovered so far.

## 1.3  Observations of X-ray sources

Due to the opaqueness of the Earth's atmosphere to all radiation with wavelengths shorter than $\sim 300\,\mathrm{nm}$, UV, X-ray and $\gamma$-ray observations can only be accomplished above $\sim 150\,\mathrm{km}$ from the surface of the Earth. Early X-ray observations, in the 50s and the 60s were carried out by X-ray detectors aboard rockets. It was through these observations that the first galactic source was discovered (Sco X-1 by Giacconi et al., 1962) along with an intense, uniformly distributed – seemingly diffuse – X-ray background (Gursky et al., 1963). The next major step in X-ray astronomy was the launch of the UHURU X-ray observatory, that – among others – provided the first survey of the X-ray sky (Fig. 1.8). The Einstein X-ray observatory was the first telescope with imaging capabilities and also contained one of the first X-ray
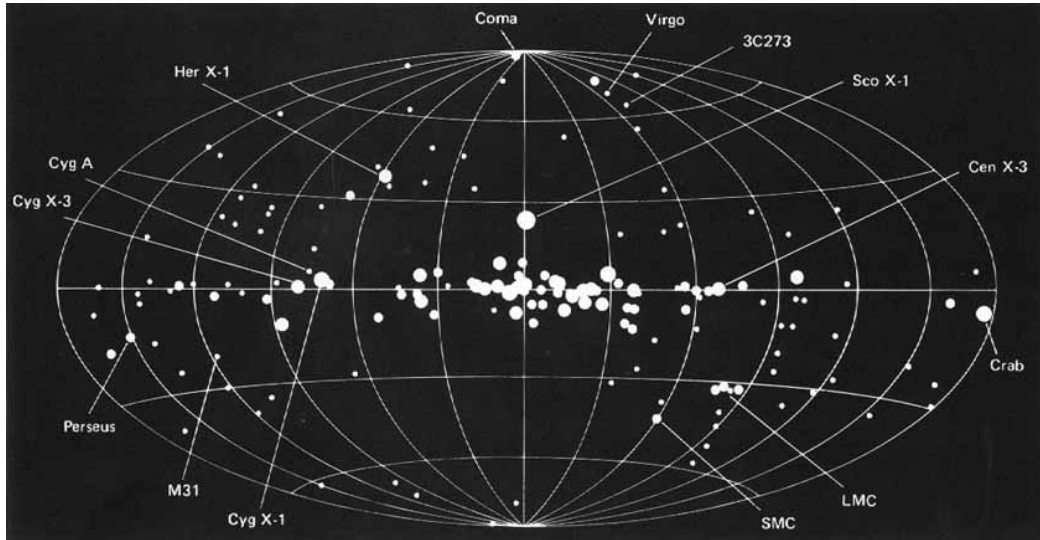
Figure 1.8: X-ray map of the Milky Way as composed by the UHURU X-ray observatory. Source: NASA archive

spectrometers. Other missions followed, with increasing sensitivity, timing and spectral resolution, culminating in modern X-ray observatories capable of conducting high resolution X-ray spectroscopy and detecting ultra-fast variability. In the present thesis, we study the spectral and timing properties of several X-ray sources, using data from the XMM-Newton, Chandra, and RXTE observatories. Below, we briefly discuss the interaction of X-ray emission with matter and the constraints it places on detectors and telescopes. We also review key aspects of these three missions.

### 1.3.1   X-rays and matter

When X-rays traverse through the interstellar material, they are attenuated exponentially. If $I_o$ is the intensity of the X-ray emission at the location of the source, it will be attenuated by a factor of $e^{-\sigma\,N_H}$, when observed from Earth. $N_H$ is an astronomical term called column density. It is the number of atoms contained in a 1-cm$^2$ column between the observer and the source. $\sigma$ is the absorption cross-section. In the energy range between 0.1-10 keV absorption is mostly due to the photoelectric effect. The absorption cross-section for the photoelectric effect varies as $\sim A_z\,Z^3\,E^{-3}$, where $A_z$ is
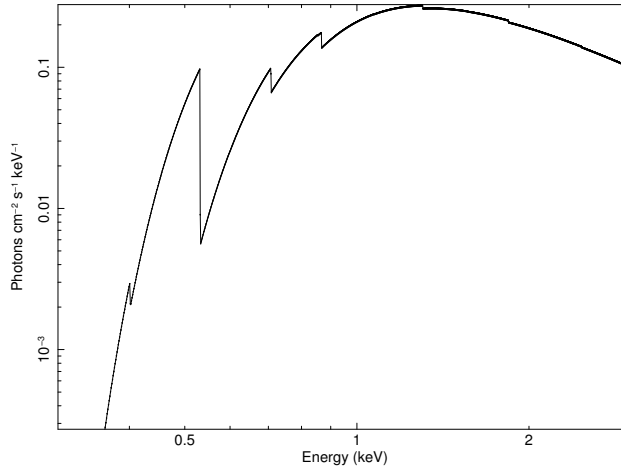
Figure 1.9: Model of a power law spectrum observed through material with column density of $5 \times 10^{21}\ cm^2$. The abundances of the different elements in the material are taken from Grevesse & Sauval (1998)

the abundance of Z-element, Z is the atomic number and $E$ is the energy of the X-ray photon. Therefore, lower energy photons are more likely to be absorbed and heavier elements are stronger absorbers. The absorption cross-section of each element increases abruptly near the photon energy threshold, above which, it can dislodge a K or an L-shel electron. This results in the creation of absorption edges on the observed continuum (Fig. 1.9).

In addition to being absorbed, X-ray photons can also be Compton scattered by bound or free electrons in the material. During the scattering, the photon transfers some of its energy to the electron (see eq. 2.26). In low energies, this energy loss is insignificant. However, more energetic photons (e.g. above $100\,\mathrm{keV}$) can lose a substantial fraction of their energy to Compton scattering.

## 1.3.2   X-ray telescopes

X-ray photons can be reflected off smooth surfaces if they are incident at – so called – grazing angles ($< 1^o$). The efficiency of X-ray reflection is very close to unity for angles that are smaller than a critical angle $\theta_c = c\sqrt{\rho}/E$, where $\rho$ is the density of the reflective material and $E$ is the energy of the
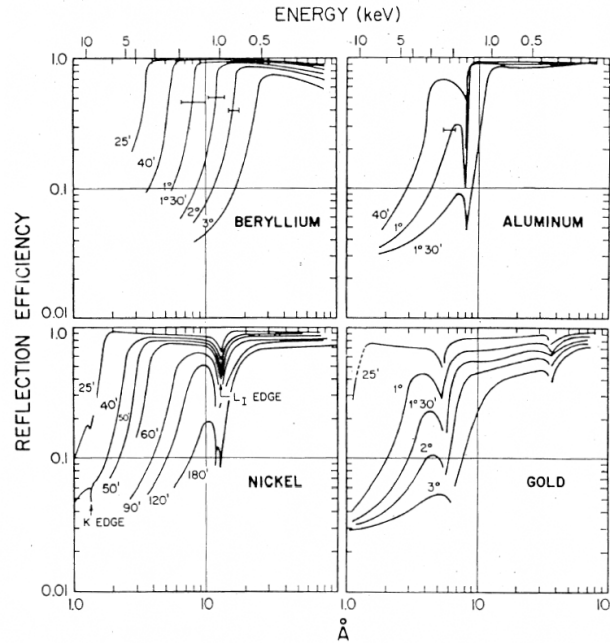
Figure 1.10: Reflection efficiencies of X-ray photons for beryllium, aluminum, nickel and gold (Seward 1977).

incident photon. Therefore, high-Z elements have larger critical angles and the reflection efficiency of X-ray telescope mirrors have high energy cutoffs. Namely, the reflection efficiency of different elements drops abruptly when the incident photons exceed an energy threshold above which the critical angle becomes smaller than the reflection angle. E.g nickel and gold for a reflection angle of $0.5^o$ have an efficiency cutoff at $\approx 6$ and $\approx 9$ keV respectively (Fig. 1.10). By taking advantage of X-ray reflection[1], X-ray photons can be guided and focused, in order to produce images.

In 1952 Hans Wolter demonstrated that a combination of hyperboloid and paraboloid mirrors can be used to form an X-ray image. Further development of Wolter's ideas (e.g. Giacconi & Rossi, 1960) led to the development of contemporary mirrors with the – so called – Wolter-I configuration. In Wolter-I type telescopes (Fig. 1.11) X-rays are initially reflected off the in-

---

[1]This reflection is entirely different from the astrophysical "X-ray reflection" described in 1.2.1. In the astrophysical context, X-rays are reprocessed by the material, resulting in partial absorption and remission.
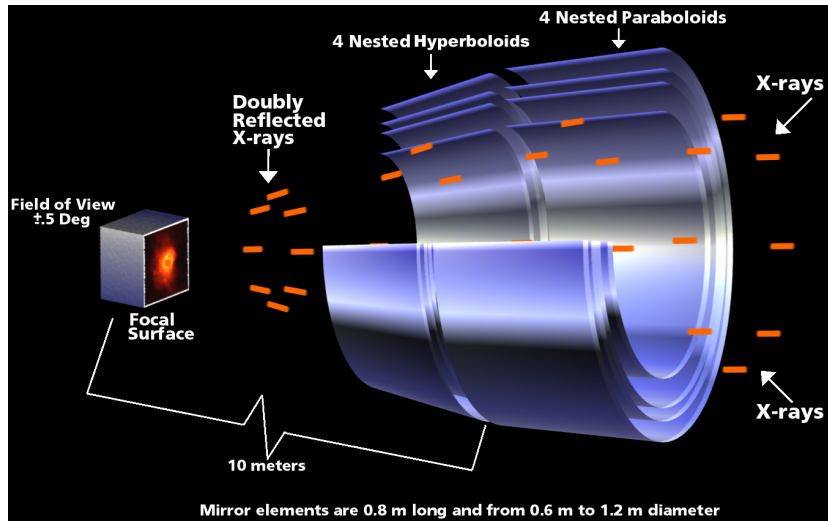
Figure 1.11: Schematic illustration of a the Wolter-I type mirrors composing the telescope on board Chandra observatory. Source: NASA/CXC/D. Berry 2010

side of a parabolic surface and then from the inside of a hyperboloid surface, resulting in image focused on an X-ray detector. Multiple mirrors can be concentrically nested in order to increase the effective area of the telescope.

## 1.3.3   X-ray detectors

### Proportional counter

The proportional counter is an X-ray detector that also measures the energy of the detected photons. The detector consists of an ion chamber, a sealed environment filled with inert gas, often a mixture of argon and methane or xenon and propane. When an X-ray photon enters the gas it interacts with one of its atoms creating an electron and a positively charged ion. As the photoelectron traverse through the gas chamber, it creates a trail of electron - ion pairs. Their number is proportional to the energy of the X-ray photon. Namely, voltage is applied to the ion chamber that is low enough, so that it can still act as an ion chamber, but strong enough to prevent recombination. As the photoelectrons approach the anode a Townsend avalanche (e.g. Knoll, 2000) is produced, resulting in a surge of electrons that are collected by the wire (Fig. 1.12). The output of the detector comes in the form of a "pulse
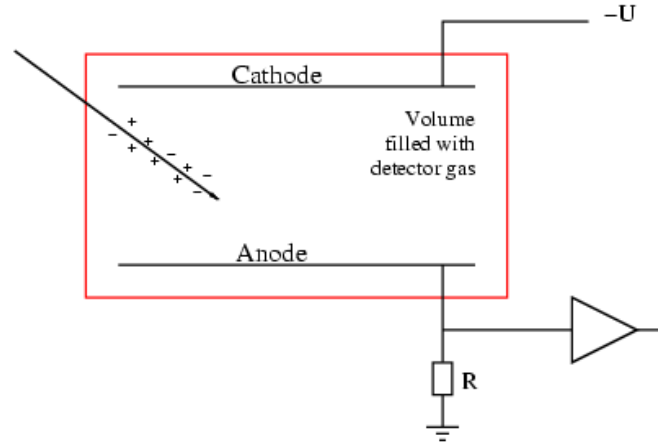
Figure 1.12: Simple diagram of a proportional counter. The space between the cathode and anode is filled with inert gas. Incident photons ionize the gas. Each event and its corresponding energy level is registered by the counter.

height" spectrum, which is linearly related to the energy of the incident photon. Proportional counters are used for X-ray spectroscopy and imaging, albeit with a low to moderate energy resolution (e.g. $\Delta E/E \sim 18\%$, at $6\,\mathrm{keV}$) and low angular resolution. On the other hand, they have very fast read-out, high quantum efficiency and large effective area and can provide spectra ranging from 0.1-90 keV.

**Charge-coupled devices**

Charge-coupled devices (CCDs) have revolutionized imaging technology and are widely used in observational astronomy. In X-ray astronomy, compared to proportional counters, CCDs provide significantly improved energy (e.g. $\Delta E/E \sim 2.5\%$, at $6\,\mathrm{keV}$) and spatial resolution. Detection of X-ray photons by CCDs is achieved through absorption of the X-ray photon by solid state material (silicon). When an X-ray photon is absorbed by the depletion region of the CCD, it creates multiple electron-hole (e-h) pairs (Fig. 1.13). The electrons and holes are separated by an internal electric field, with the holes rapidly recombining, while the electrons remain trapped in the pixel in which they were generated, until they are read out. The relation between the number of generated photoelectrons and the energy of the absorbed photons
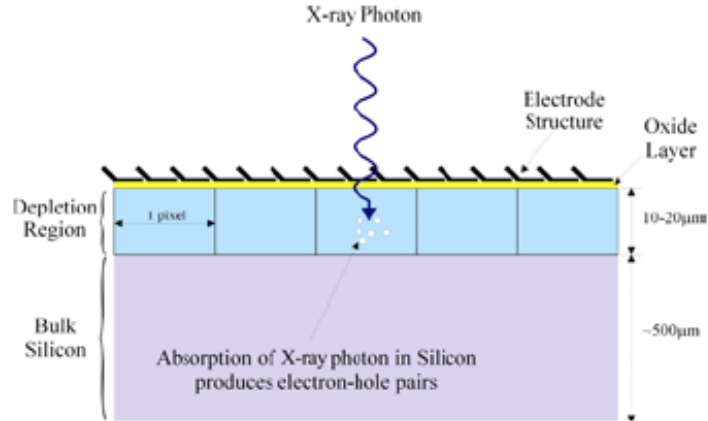
Figure 1.13: Simple diagram of a charge-coupled device. As X-ray photons enter the CCD depletion region electron-hole pairs are created. The electrons remain trapped in each pixel until they are read out. Upon this the position and energy of each incident photon is recorded.

is $N_E \sim E/3.68\,\text{eV}$, with slight variations depending in the temperature of the CCD. CCDs offer high detection efficiency, excellent linearity between photon energy and detected charges, variable exposure times and improved spectroscopic and imaging capabilities. Nevertheless, they also have shortcomings, among which the most important is the – so called – "pileup effect". Namely, if the flux from the observed source is high enough, two or more photons may be absorbed by the same pixel before it's read out. The resulting charge is, consequently, recorded as a single event of higher energy. In sources with high count rates, the pileup effect may result in significant distortion of the spectrum, mostly causing an artificial hardening of the X-ray continuum.

## 1.3.4 X-ray observatories

In the present dissertation we made extensive use of observational data, acquired from three major X-ray observatories, XMM-Newton, Chandra and RXTE. Below, we briefly describe the main aspects of these three, very important missions.
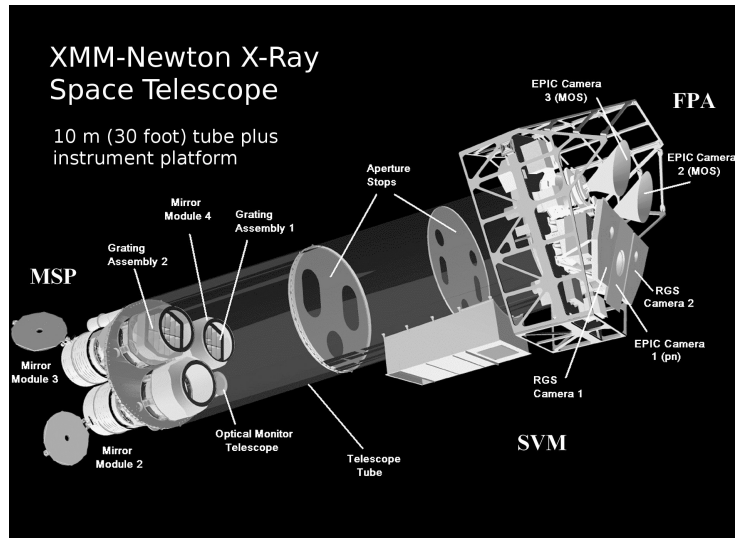
Figure 1.14: A schematic diagram of the XMM-Newton space observatory and its various parts. Source: ESA / AOES Medialab

**XMM-Newton observatory**

Orbiting the Earth at a 48 h, highly eccentric orbit, at an altitude ranging from 114000 km (apogee) to 7000 km (perigee), the XMM-Newton space observatory (Jansen et al., 2001) is the cornerstone of the European Space Agency's (ESA) Horizon 2000 program, and one of the major X-ray telescopes available today. XMM-Newton is equipped with three identical telescopes, each consisting of 58 gold-coated mirrors, with a focal length of 7.5 m. In figure 1.14 a schematic illustration of XMM-Newton is presented, featuring its various components.

Approximately half of the emission collected by the two of the three telescopes is diverted towards a reflection grating spectrometer (RGS: den Herder et al., 2001) that is best suited for high resolution spectroscopy ( $\Delta E/E \sim 0.2\%$, at 0.5 keV) in the 0.2-2 keV range. Since RGS data are not used in this thesis, the RGS system is not discussed further.

At the focal point of each telescope, one of three different CCD imaging cameras are placed. The two telescopes equipped with the gratings of RGS have two Metal Oxide Semiconductor (MOS) CCD arrays at their focal point. At the focal point of the third telescope lies an array of pn-CCDs. All three cameras comprise the European Photo Imaging Camera (EPIC).
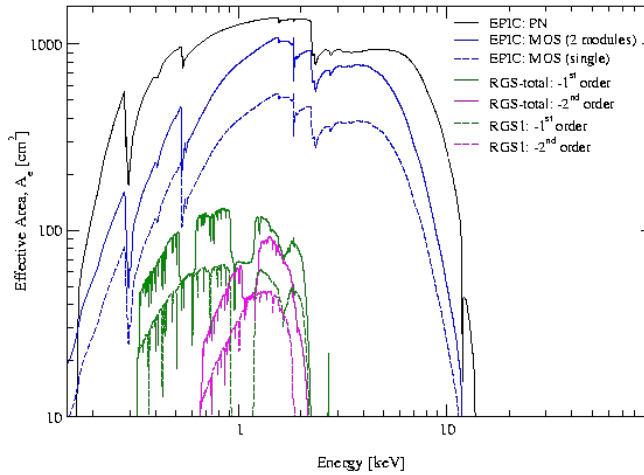
Figure 1.15: Effective area vs energy for all XMM-Newton detectors. Source: ESA

The EPIC-pn camera (Strüder et al., 2001) is comprised of 12 pn-CCD chips, consisting of 200 rows and 64 columns of $150\times150\mu$m pixels. When operated in "Imaging Mode" the EPIC-pn camera has high sensitivity and a short time frame of 73.3 ms. However, it is susceptible to pileup, when observing sources with a high count rate. When switched to "Timing Mode" photon coordinates are resolved one dimensionally, along the column axis, this results in a read out time of 0.03 ms. In this setting pileup is significantly mitigated. At the time of launch, the spectral resolution of EPIC-pn varied from 111 eV (Full Width at Half Maximum, FWHM) at 1 keV to 162 at 6 keV (Strüder et al., 2001). These values degrade at $\sim$2.5 eV/yr due to radiation damage.

The EPIC-MOS cameras (MOS1 and MOS2: Turner et al., 2001) consist of seven MOS-type CCDs with $600\times600$, $\mu$m pixels each. They have a higher energy resolution than EPIC-pn ($\sim$80 eV at 1 keV and $\sim$150 eV at 6 keV), but because they are placed at the focal point of the two telescopes equipped with the RGS gratings, they only receive $\sim$ 44% of the incident flux and, therefore, have a smaller effective area than EPIC-pn (Fig. 1.15). Furthermore, the MOS detectors have a longer integration time (of 2.6s) and as a result are
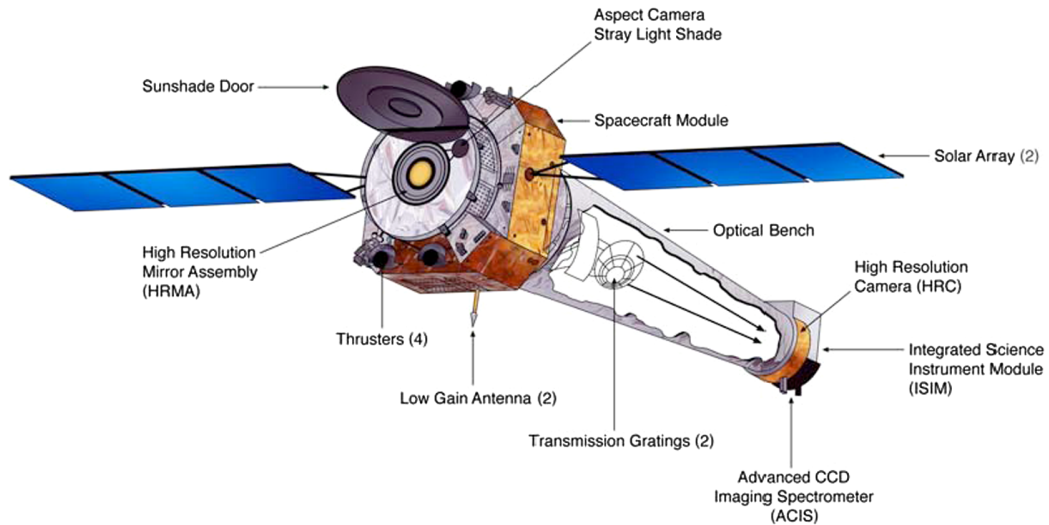
Figure 1.16: A schematic diagram of the Chandra space observatory and its various parts. Source: NASA

more susceptible to pileup. Nevertheless, EPIC-MOS can also be operated in timing mode, thus improving time resolution and alleviating the effects of pileup.

**Chandra X-ray observatory**

The Chandra X-ray observatory was launched in July 1999. It has a 64 h eccentric orbit at a distance varying from 16000 km at perigee to 133000 km at apogee. Its telescope consists of four pairs of Wolter-I type mirrors (Fig. 1.11) with a 10 m focal length. At its focal point, four different detectors are placed (Fig. 1.16). The High Resolution Camera (HRC: Murray et al., 1997), the Advanced CCD Imaging Spectrometer (ACIS: Garmire et al., 2003) and the high resolution spectrometers HETGS (High Energy Transmission Grating Spectrometer) and LETGS (Low Energy Transmission Grating Spectrometer). Below, we briefly, discuss the details of HETGS, whose science products are used in this thesis.

The HETG consists of two grating spectrometers, the MEG (Medium Energy Grating) and the HEG (High Energy Grating), covering a combined energy range between 0.1 and 10 keV. The HETGS operates on the principle of spectral separation through diffraction of X-rays by fine gratings. Namely,
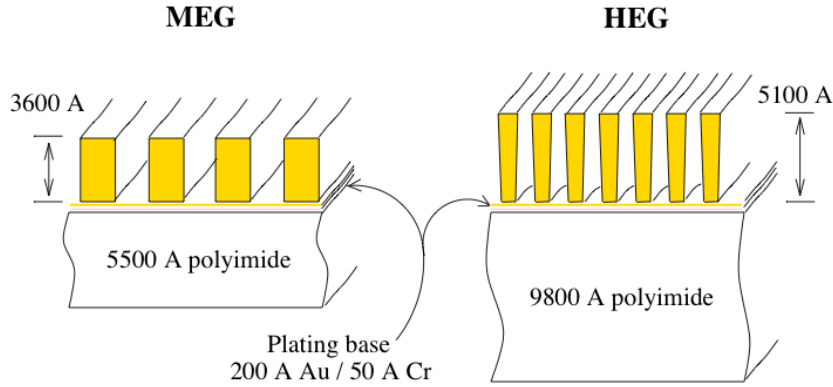
Figure 1.17: Schematic illustration of the cross-sections of the MEG and HEG membranes. All units are in Angstrom. Source: NASA

incident X-ray photons are diffracted by an angle $\theta$ given by:

$$\sin\theta = \frac{m\,\lambda}{d} \tag{1.1}$$

where m is the integer number signifying the order of diffraction (m=0 represents an non-dispersed image), d is the distance between two slits and $\lambda$ is the wavelength of the incident photon. In order to displace a 2.07Å (corresponding to 6 keV) X-ray photon by 1 cm over the 10 m focal length, the required constructive interference will have to be at an angle of $\approx 3'$. Therefore, according to equation 1.1, the slit spacing $d$, must be $\approx 0.21\mu$m. The spacings of the Chandra gratings are 0.2, 0.4 and 1 $\mu$m wide (Fig. 1.17). Since the gratings need to be opaque to X-rays, they are made of high-Z material, in this case gold. The time resolution of the HETGS is not high enough (3.2s) to detect ultra-fast variability and conduct light curve analysis in the order of seconds and milliseconds. However, the fine gratings of HEG and MEG (Fig. 1.17) provide unprecedented spectral resolution, with a $\Delta E/E$ as high as $\sim 0.07\%$, in the 0.2-10 keV range.

### RXTE

The Rossi X-ray Timing Explorer (RXTE) was launched in 1995 and remained operational for 16 years until January 23 2012. From the discovery of kHz QPOs (van der Klis et al., 1996) and numerous X-ray pulsars, to the study of the innermost regions of accreting black holes, to measurements of

**XTE Spacecraft**
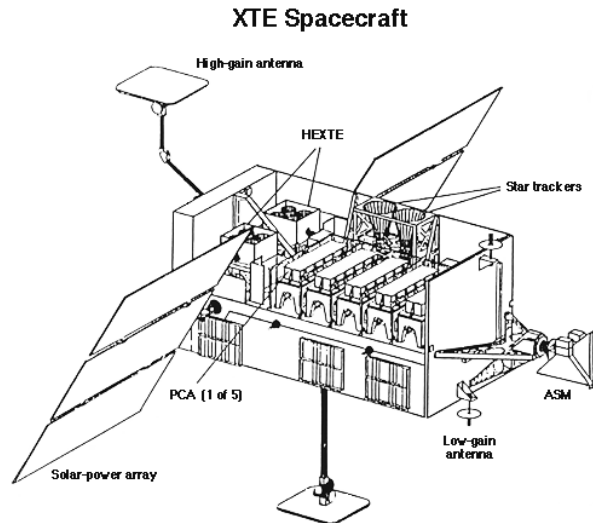


Figure 1.18: Schematic illustration of RXTE and all of its components. Source: NASA

the spectrum of the cosmic X-ray background (Revnivtsev et al., 2003) and the discovery of the origins of the Galactic ridge X-ray emission (Revnivtsev et al., 2006), RXTE has contributed immensely to the study of the X-ray sky.

RXTE was equipped with three different scientific instruments (Fig. 1.18). The proportional counter array (PCA: Jahoda et al., 1996), operating in the 2-60 keV range, with an energy resolution of 18% at 6 keV and a time resolution of the order of $\mu$s. The High Energy X-ray Timing Experiment (HEXTE: Rothschild et al., 1998), with an energy range of 15-250 keV and spectral resolution of 15% at 60 keV and a time resolution of 8 $\mu$s. The All Sky Monitor (ASM: Levine et al., 1996), consisting of three wide angle cameras, equipped with proportional counters. The ASM had a 2-12 keV energy range and would resolve 80% of the sky every 90 minutes.

The combined properties of the instruments on board RXTE, resulted in an unparalleled ability to study fast and ultra-fast X-ray variability and to probe X-ray sources across a wide energy range. Furthermore, the extensive ASM catalog is an invaluable source of data, covering long term variability of hundreds of X-ray sources. In this thesis we use the PCA's timing and spectral capabilities to make an important discovery, regarding X-ray pulsar 4U 1626-67.

## 1.4   Outline of the thesis

This dissertation features the results of three studies. In Chapter 2 we study effects of X-ray reflection off C/O or O/Ne/Mg dominated disks in UCXBs. We use analytical and numerical methods to predict the effects of the anomalous C/O abundance of the disk material, on the strength of the Fe K$\alpha$ emission line. An emission line that is usually observed in the spectra of nominal LMXBs with accretion disks of solar-like composition. Our results and predictions were published in the Monthly Notices of the Royal Astronomical Society (MNRAS: Koliopanos, Gilfanov & Bildsten, 2013). In Chapter 3 we follow up on our theoretical predictions, looking to confirm them and also demonstrate our model as a useful diagnostic for the chemical composition of the accretion disk and donor star in UCXBs. For this purpose we investigate the spectra of well known UCXBs, in search for the Fe K$\alpha$ emission line. The results of this study were also published by MNRAS (Koliopanos et al., 2014). In the 4th and final chapter of this thesis we discover a luminosity dependent change in the emission diagram of the accretion column of X-ray pulsar 4U 1627-67. In this work we provide – for the first time – spectroscopic evidence of a phenomenon that was theoretically predicted forty years ago. Our results have been submitted to MNRAS for publication.

# Bibliography

Bachetti M. et al., 2014, Nature, 514, 202

Bambynek W., Crasemann B., Fink R. W., Freund H.-U., Mark H., Swift C. D., Price R. E., Rao P. V., 1972, Reviews of Modern Physics, 44, 716

Basko M. M., Sunyaev R. A., 1975, A&A, 42, 311

Basko M. M., Sunyaev R. A., 1976, MNRAS, 175, 395

Bildsten L. et al., 1997, ApJS, 113, 367

Bildsten L., Deloye C. J., 2004, ApJ, 607, L119

den Herder J. W. et al., 2001, A&A, 365, L7

Done C., Gierliński M., Kubota A., 2007, A&A Rev., 15, 1

Frank J., King A., Raine D. J., 2002, Accretion Power in Astrophysics: Third Edition

Garmire G. P., Bautz M. W., Ford P. G., Nousek J. A., Ricker, Jr. G. R., 2003, in Society of Photo-Optical Instrumentation Engineers (SPIE) Conference Series, Vol. 4851, X-Ray and Gamma-Ray Telescopes and Instruments for Astronomy., Truemper J. E., Tananbaum H. D., eds., pp. 28–44

Giacconi R., Gursky H., Paolini F. R., Rossi B. B., 1962, Physical Review Letters, 9, 439

Giacconi R., Rossi B., 1960, J. Geophys. Res., 65, 773

Grevesse N., Sauval A. J., 1998, Space Sci. Rev., 85, 161

Gursky H., Giacconi R., Paolini F. R., Rossi B. B., 1963, Physical Review Letters, 11, 530

Jahoda K., Swank J. H., Giles A. B., Stark M. J., Strohmayer T., Zhang W., Morgan E. H., 1996, in Society of Photo-Optical Instrumentation Engineers (SPIE) Conference Series, Vol. 2808, EUV, X-Ray, and Gamma-Ray Instrumentation for Astronomy VII, Siegmund O. H., Gummin M. A., eds., pp. 59–70

Jansen F. et al., 2001, A&A, 365, L1

Knoll G. F., 2000, Radiation detection and measurement

Koliopanos F., Gilfanov M., Bildsten L., 2013, MNRAS, 432, 1264

Koliopanos F., Gilfanov M., Bildsten L., Trigo M. D., 2014, MNRAS, 442, 2817

Levine A. M., Bradt H., Cui W., Jernigan J. G., Morgan E. H., Remillard R., Shirey R. E., Smith D. A., 1996, ApJ, 469, L33

Lewin, W. H. G., van Paradijs, J., & van den Heuvel, E. P. J. 1995, X-ray Binaries,

Martin-Carrillo A. et al., 2012, A&A, 545, A126

Mészáros P., 1992, High-energy radiation from magnetized neutron stars.

Murray S. S. et al., 1997, in Society of Photo-Optical Instrumentation Engineers (SPIE) Conference Series, Vol. 3114, EUV, X-Ray, and Gamma-Ray Instrumentation for Astronomy VIII, Siegmund O. H., Gummin M. A., eds., pp. 11–25

Nelson L. A., Rappaport S. A., Joss P. C., 1986, ApJ, 311, 226

Popham R., Sunyaev R., 2001, ApJ, 547, 355

Pozdnyakov L. A., Sobol I. M., Sunyaev R. A., 1983, Astrophysics and Space Physics Reviews, 2, 189

Revnivtsev M., Gilfanov M., Sunyaev R., Jahoda K., Markwardt C., 2003, A&A, 411, 329

Revnivtsev M., Sazonov S., Gilfanov M., Churazov E., Sunyaev R., 2006, A&A, 452, 169

Roelofs G. H. A., Groot P. J., Nelemans G., Marsh T. R., Steeghs D., 2006, MNRAS, 371, 1231

Rothschild R. E. et al., 1998, ApJ, 496, 538

Savonije G. J., de Kool M., van den Heuvel E. P. J., 1986, A&A, 155, 51

Shakura N. I., Sunyaev R. A., 1973, A&A, 24, 337

Strüder L. et al., 2001, A&A, 365, L18

Sunyaev R. A., Shakura N. I., 1986, Soviet Astronomy Letters, 12, 117

Sunyaev, R. A., & Titarchuk, L. G. 1980, A&A, 86, 121

Turner M. J. L. et al., 2001, A&A, 365, L27

Wolter H., 1952, Annalen der Physik, 445, 94

van der Klis, M., Swank, J. H., Zhang, W., et al. 1996, ApJ, 469, L1

Verbunt, F., & van den Heuvel, E. P. J. 1995, X-ray Binaries, 457

Yungelson L. R., Nelemans G., van den Heuvel E. P. J., 2002, A&A, 388, 546

# Chapter 2

# X-ray diagnostics of chemical composition of the accretion disk and donor star in ultra-compact X-ray binaries

Koliopanos, Gilfanov & Bildsten

## 2.1 Introduction

Ultra compact X-ray binaries (UCXBs) are a sub-group of X-ray binaries with orbital periods of less than 1 hour. Their small orbital periods do not allow for a hydrogen rich, main sequence donor (e.g. Rappaport & Joss 1984; Nelson, Rappaport, & Joss 1986). The most likely scenarios for their formation (for details see e.g. Tutukov & Yungelson, 1993; Iben, Tutukov, & Yungelson, 1995; Nelemans, 2005) predict that the donor star in such systems is a white dwarf (WD) or a helium star. Driven by the loss of the orbital angular momentum due to gravitational wave radiation, UCXBs are often observed as persistent and relatively luminous X-ray sources with luminosities in the $10^{36} - 10^{38}\text{erg s}^{-1}$ range (Nelson, Rappaport & Joss, 1986; Bildsten & Deloye, 2004).

Given the nature of the donor star, the accreting material in UCXBs should have a chemical composition consistent with the ashes of H burning (mostly He and $^{14}$N), He burning (mostly C/O) or carbon burning (mostly O/Ne). Depending on the binary's formation channel, it can vary from C/O-rich to He-rich. Indeed, optical observations of several UCXBs, for example, 4U 0614+091, 4U 1543-624 and 2S 0918-549 suggest accretion of C/O-rich material (Nelemans et al. 2004; Nelemans, Jonker, & Steeghs 2006; Werner et al. 2006). On the other hand, in the case of 4U 1916-05 they reveal evidence pointing to a He-rich donor (Nelemans, Jonker & Steeghs, 2006). Modeling of type I X-ray bursts from 4U 1820-30 suggest that the accreting material in this system is also helium dominated (Bildsten, 1995; Cumming, 2003).

X-ray spectra of X-ray binaries usually contain the so called reflected component (e.g Gilfanov, 2010, and references therein). This component is produced due to reprocessing of primary emission by the optically thick Shakura-Sunyaev accretion disk and by the surface of the donor star facing the compact object. The primary emission may originate in a hot optically thin corona, in the accretion disk itself or, in the case of a NS accretor, in the boundary layer on the surface of the star, and carries most of the energy. Depending on its origin, the spectrum of the primary emission may vary from soft thermal to hard power law-like spectrum. Although the reflected component is energetically insignificant, it carries information about the geometry of the accretion flow (e.g. Gilfanov, Churazov, & Revnivtsev, 1999) and, via fluorescent lines and absorption edges of metals, about the chemical composition, ionization state and kinematics of the accretion disk material.

Reprocessing of X-ray radiation by the accretion disk and by the surface

of the donor star has been studied extensively by many authors, starting from the seminal paper by Basko, Sunyaev, & Titarchuk (1974). The shape and strength of the iron $K_\alpha$ fluorescent line has been investigated by Basko (1978) and Bai (1979). Semi-analytical expressions for reflection spectra including the effects of both photoionization and Compton scattering, have been derived by Lightman & White (1988) and White, Lightman, & Zdziarski (1988), and formulated in terms of K-shell fluorescence and the characteristic Compton hump between 10 keV and 300 keV. Later on, the effect of ionization of the accreting material on reflected spectra has been included (e.g. Ross & Fabian 1993; Zycki et al. 1994; Nayakshin, Kazanas, & Kallman 2000). The need for better accuracy and more realistic and complex geometries has led to application of Monte-Carlo (MC) methods that complimented and enhanced analytical calculations. Many authors have computed detailed models based on Monte-Carlo techniques (e.g. George & Fabian, 1991; Matt, Fabian, & Ross, 1993; Ballantyne, Ross, & Fabian, 2001).

Despite of the amount of effort invested in studying reflection of X-ray emission from optically thick media, all prior work concentrated on the $\sim$ solar abundance case, with only moderate variations of the element abundances considered in some of the papers. On the other hand, in the case of UCXBs, we expect that accreting material may have significantly non-solar abundances, for example with all hydrogen and helium being converted to carbon and oxygen. Such drastic abundance modifications should lead to strong changes in the properties of the reflected spectrum, especially in its fluorescent line content. This problem is investigated in the present paper. The composition of the accreting material is discussed in Section 2.2. In Sections 2.3–2.5, we consider an idealized case of an optically thick slab of neutral material in order to identify main trends and then (Section 2.6) discuss modifications to this picture which may be introduced by gravitational settling of heavy elements in the white dwarf envelope and ionization of the accretion disk material by viscous heating and irradiation. We use simple analytical calculations (Section 2.3 and Section 2.4) to illustrate the physical origin of the main dependencies and then utilize the Monte-Carlo technique to compute reflected spectra for strongly non-solar abundances of the type expected in the donor stars in UCXBs (Section 2.5). We mainly focus on the strengths of fluorescent lines of the elements expected to be abundant in different formation scenarios of UCXBs.

Table 2.1: Abundances of elements for different types of white dwarfs used throughout the paper.

| Element | He Pandey et.al. | C/O García Berro et.al. | O/Ne Gil-Pons &, García Berro |
|---|---|---|---|
| H | $1.99 \cdot 10^{-6}$ | - | - |
| He | $0.997$ | - | - |
| C | $1.58 \cdot 10^{-3}$ | $0.563$ | - |
| O | $3.97 \cdot 10^{-4}$ | $0.422$ | $0.649$ |
| Ne | $3.66 \cdot 10^{-4}$ | $1.37 \cdot 10^{-2}$ | $0.262$ |
| Na | $6.06 \cdot 10^{-6}$ | $2.08 \cdot 10^{-5}$ | $4.93 \cdot 10^{-2}$ |
| Mg | $1.08 \cdot 10^{-4}$ | $3.69 \cdot 10^{-4}$ | $3.88 \cdot 10^{-2}$ |
| Si | $1.01 \cdot 10^{-4}$ | $3.44 \cdot 10^{-4}$ | $4.43 \cdot 10^{-4}$ |
| S | $4.59 \cdot 10^{-5}$ | $1.57 \cdot 10^{-4}$ | $2.02 \cdot 10^{-4}$ |
| Ar | $1.27 \cdot 10^{-5}$ | $4.34 \cdot 10^{-5}$ | $5.58 \cdot 10^{-5}$ |
| Cr | $1.33 \cdot 10^{-6}$ | $4.54 \cdot 10^{-6}$ | $5.84 \cdot 10^{-6}$ |
| Mn | $6.94 \cdot 10^{-7}$ | $2.38 \cdot 10^{-6}$ | $3.06 \cdot 10^{-6}$ |
| Fe | $9.18 \cdot 10^{-5}$ | $3.14 \cdot 10^{-4}$ | $4.04 \cdot 10^{-4}$ |
| Co | $2.36 \cdot 10^{-7}$ | $8.07 \cdot 10^{-7}$ | $1.04 \cdot 10^{-6}$ |
| Ni | $5.04 \cdot 10^{-6}$ | $1.73 \cdot 10^{-5}$ | $2.22 \cdot 10^{-5}$ |
| Cu | $4.59 \cdot 10^{-8}$ | $1.57 \cdot 10^{-7}$ | $2.02 \cdot 10^{-7}$ |
| Zn | $1.13 \cdot 10^{-7}$ | $3.86 \cdot 10^{-7}$ | $4.96 \cdot 10^{-7}$ |

Abundances are by number of particles. The references to the original abundance calculations are given in the column titles. The numbers written in italics are from these calculations. Abundances of other elements were fixed at the solar values in mass units and then converted to concentration abundances.
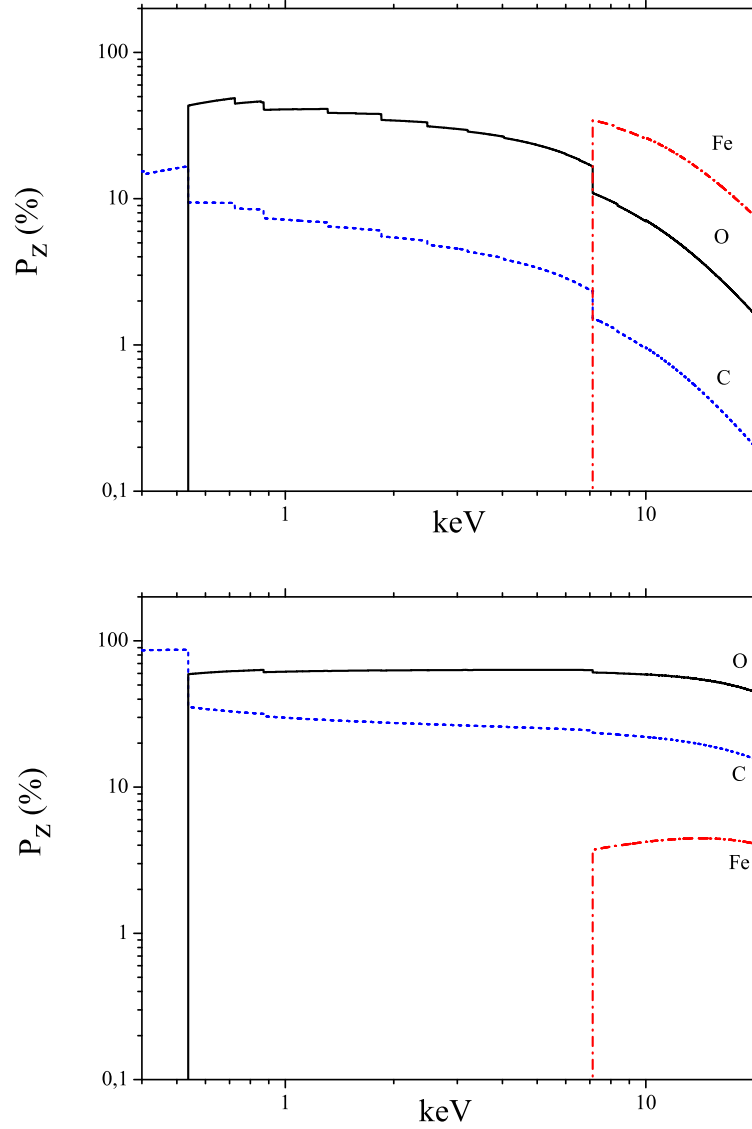
Figure 2.1: The probability $P_Z(E)$ (eq.(2.1)) for an incident photon to be absorbed due to K-shell ionization of carbon (blue dashed line), oxygen (black solid line) and iron (red dash-dotted line), in the solar abundance case (upper panel) and for the composition of a C/O white dwarf as tabulated in Table 2.1 (lower panel).

## 2.2   Composition of the accreting material

Different initial parameters and the environment of UCXB progenitors may lead to a variety of donors (e.g Savonije, de Kool, & van den Heuvel, 1986; Podsiadlowski, Rappaport, & Pfahl, 2002; Yungelson, Nelemans, & van den Heuvel, 2002) – non-degenerate He star, He white dwarf, C-O or O-Ne-Mg white dwarf. As it will become clear later, from the point of view of classification of the reflected spectra, the variety of abundance patterns can be broadly divided into two types – (i) He-rich and (ii) C/O/Ne/Mg-rich.

A typical isolated C/O white dwarf is expected to consist of a core mostly made of a mixture of carbon and oxygen, surrounded by a He-rich layer of up to $10^{-2}$ M$_\odot$. On top of the helium layer there may be a thin layer of hydrogen of up to $10^{-4}$ M$_\odot$ (e.g Kawaler, 1995; Althaus et al., 2010). A late shell flash could produce a C/O-rich envelope comprised of $\sim 30\%$ of He from convective shell burning (Iben, 1983). The mass of the He-C-O mantle surrounding the C/O core can grow up to $10^{-1}$M$_\odot$, itself enveloped by a thin layer of H in the case of a hybrid white dwarf (Iben & Tutukov, 1985, 1987). On the other hand, if the initial mass of the companion star was in the $\sim 8 - 11$M$_\odot$ range, a UCXB with an O-Ne white dwarf donor may be formed (Gil-Pons & García-Berro, 2001).

In the case of a white dwarf in a binary system, this basic structure will be modified by a co-evolution with the companion star. H and He layers can either be stripped away during the initial stages of binary interaction (Kaplan, Bildsten, & Steinfadt, 2012) or be gradually depleted due to accretion. Indeed, typical luminosities of UCXBs are in the $\sim 10^{36} - 10^{38}$ erg/s range, implying the mass accretion rate in the $\sim 10^{-10} - 10^{-8}$ M$_\odot$/yr range. At this rate, a surface layer of $\lesssim 10^{-2}$ M$_\odot$ will be depleted within $\lesssim 1 - 100$ Myrs, which is (much) shorter than the expected life times of such systems.

If the white dwarf donor has been completely stripped of its H and He layers, the chemical composition of the accreting material will be determined by its core. For the purpose of this calculation we will ignore the complexity of the possible abundance patterns and assume the following mass fractions: C = O $\simeq 0.49$ and Ne $\simeq 0.02$ (e.g García-Berro et al., 2008). More massive white dwarfs are expected to have cores composed mainly of oxygen and neon (e.g Ritossa, Garcia-Berro, & Iben, 1996), in which case we assume the following composition: Ne $\simeq 0.28$, O $\simeq 0.55$, Mg $\simeq 0.05$, Na $\simeq 0.06$ (Gil-Pons & García-Berro, 2001).

The He-star and evolved secondary donor scenarios yield an accreting

material that is He-dominated, perhaps with some He burning products and traces of H depending on the phase at which the evolved secondary star started its Roche lobe overflow. Pandey et al. (2001) have performed detailed calculations for the abundances of cool He-stars and obtained the following values: He=0.99, C=0.0052, N=0.0016, O=0.0018. For an evolved main sequence star companion Nelemans et al. (2010) used the Eggleton stellar evolution code TWIN to model the abundance pattern at the donor's surface. They predict material that is He-rich with less than 0.01 O and N and traces of C.

For the purpose of this paper we will assume that the mass fractions of all other elements, not included in the above calculations, are equal to their solar values. This is equivalent to the assumption that the total masses of these elements in the star did not change in the course of its evolution towards a white dwarf. The corresponding mass fractions were then converted to the concentration abundances taking into account changed particle concentrations of H, He, C, O etc. Solar abundances for elements with Z=1-30 were adopted from Feldman (1992), elements not listed in this tabulation were taken from Grevesse & Sauval (1998). The abundance patterns for different types of white dwarfs used throughout the paper are summarized in Table 2.1. In the Table, the values obtained in the white dwarf abundance calculations described above are given in italic, abundances of elements which mass fractions were fixed at their solar value are shown in roman font.

## 2.3   Qualitative picture

In this section and in section 2.4, we consider an idealized case of reflection from cold and neutral material. Although, at a sufficiently low mass accretion rate, this is a reasonable approximation for carbon and oxygen, it breaks down for helium in the accretion disk at any luminosity relevant to UCXBs. In the case of a cold white dwarf, it may hold on its surface. The effect of ionization is discussed in detail in section 2.5.

Although the strengths of fluorescent lines depend on the number of parameters, such as spectral index of the primary radiation, incidence angle, ionization state etc., (e.g George & Fabian, 1991; Ballantyne, Fabian, & Ross, 2002) variation of these parameters within their plausible ranges leads to rather moderate changes in the equivalent widths. Much more dramatically the EWs of fluorescent lines are affected by changes in the relative abun-

dances of different elements. As it turns out, an increase in the abundances of carbon and oxygen, not only changes the strengths of fluorescent lines of these elements, but has a much easier detectable effect on the iron line. Indeed, as it will be shown below, for the typical X-ray spectra of UCXBs, the equivalent widths of carbon and oxygen lines increase by $\sim 2 - 10$ times with respect to their solar abundance values, but still remain in the hardly detectable sub-eV range. On the other hand, the iron line drops more than 10-fold, from easily observable $\sim 100$ eV to the $\sim$ few eV range.

The effect of elemental abundances on the strength of emission lines, can be illustrated by the following simple calculation. Let's consider an optically thin layer of material illuminated by a photon beam traveling along the axis normal to its surface. The probability that an incident photon with energy $E$ is absorbed due to K-shell ionization of a given element Z (rather than being absorbed by other elements or scattered by electrons) is given by the following expression:

$$P_Z(E) = \frac{A_Z\,\sigma_{K,Z}(E)}{A_Z\,[\sigma_Z(E) + Z\,\sigma_{KN}(E)] + \sum\limits_{Z' \neq Z} \sigma'(E)} \tag{2.1}$$

where $\sigma_Z$ – the total absorption cross section of element Z, $\sigma_{K,Z}$ is its K-shell absorption cross section, $A_Z$ – the abundance of element Z by number, $\sigma_{KN}$ – the Klein-Nishina cross section. For compactness of the formula we denote $\sigma'(E) = A_{Z'}[\sigma_{Z'}(E) + Z'\sigma_{KN}(E)]$ – the total cross section due to element Z', including Thomson scattering on its electrons (see Section 2.4 for further details). Obviously, the quantity $P_Z(E)$ determines what fraction of incident photons with energy E will contribute to the production of the fluorescent line of the element $Z$ and offers a simple way to qualitatively investigate the dependence of the EW of the line on element abundances. Moreover, as it will be shown in Section 2.4, a modification of eq.(2.1) gives a reasonably accurate method to analytically compute EWs of fluorescent lines.

In Fig. 2.1 we plot the probability $P_Z(E)$ for carbon, oxygen, and iron versus energy. The left panel was computed for an atmosphere with solar abundances, the right panel – for the abundances appropriate for a C/O white dwarf (Table 2.1). As one can see from the plot, in a solar abundance case, oxygen is the dominant absorbing element for photon energies of up to $\approx 7$ keV. However, above the Fe K-shell ionization threshold of 7.11 keV, the value of $P_{Fe}$ jumps and exceeds that of $P_O$, so that at higher energies the majority of photons are absorbed by iron and contribute to its fluorescent line.
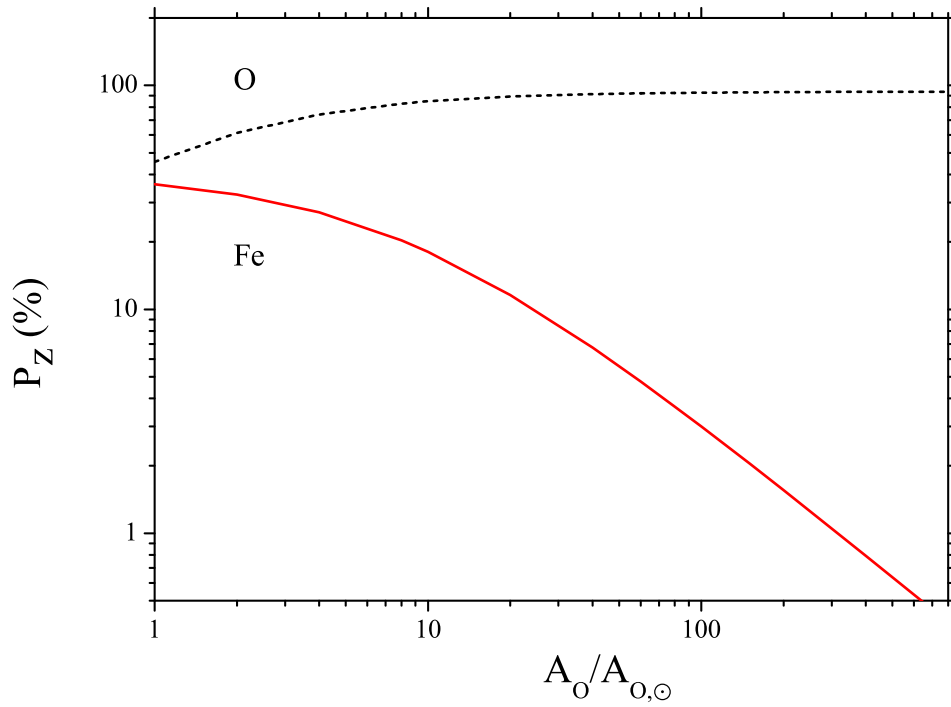
Figure 2.2: The probability of absorption by oxygen and iron calculated at the respective K-edges, versus oxygen abundance $A_O$. The latter is expressed in solar units.

For the chemical composition of a C/O WD, however, the picture changes dramatically. Even though the K-shell photo-absorption cross-section for iron is larger than the oxygen cross-section at these energies, the increased abundance of oxygen makes it the main absorbing agent in the entire energy range. As a result, the K$\alpha$ line of iron will be significantly suppressed.

As oxygen abundance increases, $P_O$ will increase linearly with $A_O$, insofar its contribution to the denominator in eq.(2.1) remains relatively small. However, at sufficiently large abundances, the oxygen term prevails and $P_O$ saturates at a value determined by the ratios of cross-sections, $P_O \sim \sigma_{K,Z}/(\sigma_Z + \sigma_{KN})$. On the contrary, $P_{Fe}$ will continue to decrease due to unlimited increase of $\sigma'$ in the denominator in eq.(2.1). This behavior is illustrated in Fig. 2.2[1] where we plot the values of $P_O$ and $P_{Fe}$ estimated at their respective K-edges, versus $A_O$. As is evident from the plot, $P_O$ increases with $A_O$ until the latter reaches a value of $\sim 20 - 25$ times solar value. At this abundance, oxygen completely dominates the opacity and nearly all incident photons that are not scattered on electrons, will be absorbed by the oxygen, regardless of their energy. Further increase of oxygen abundance does not lead to an increase of it fluorescent line strength. On the other hand, the $P_{Fe}$ curve shows unlimited decreases as $A_O$ increases, asymptotically $P_{Fe} \propto A_O^{-1}$.

## 2.4   Analytical approach in the single scattering approximation

We consider reflection from a semi-infinite atmosphere in the single scattering approximation. The spectral intensity of reflected emission $S_{refl}$ ($phot\,sec^{-1}\,cm^{-2}\,keV^{-1}\,sr^{-1}$)

---

[1] Note that for the purpose of this plot we fixed abundances of all elements except oxygen at their solar value, i.e. no condition of the nucleon number conservation was imposed. Such an abundance sequence does not represent any of the WD compositions and is employed here to investigate the behavior of equivalent widths in the limit of high $A_O$ (or, equivalently, high O/Fe). If we use the O/Fe ratios (($O/Fe)_\odot \approx 26$, $(O/Fe)_{CO} \approx 1.3 \cdot 10^3$) to characterize the oxygen overabundance, a C/O white dwarf would approximately correspond to the $A_O/A_{O,\odot} \sim 50$.
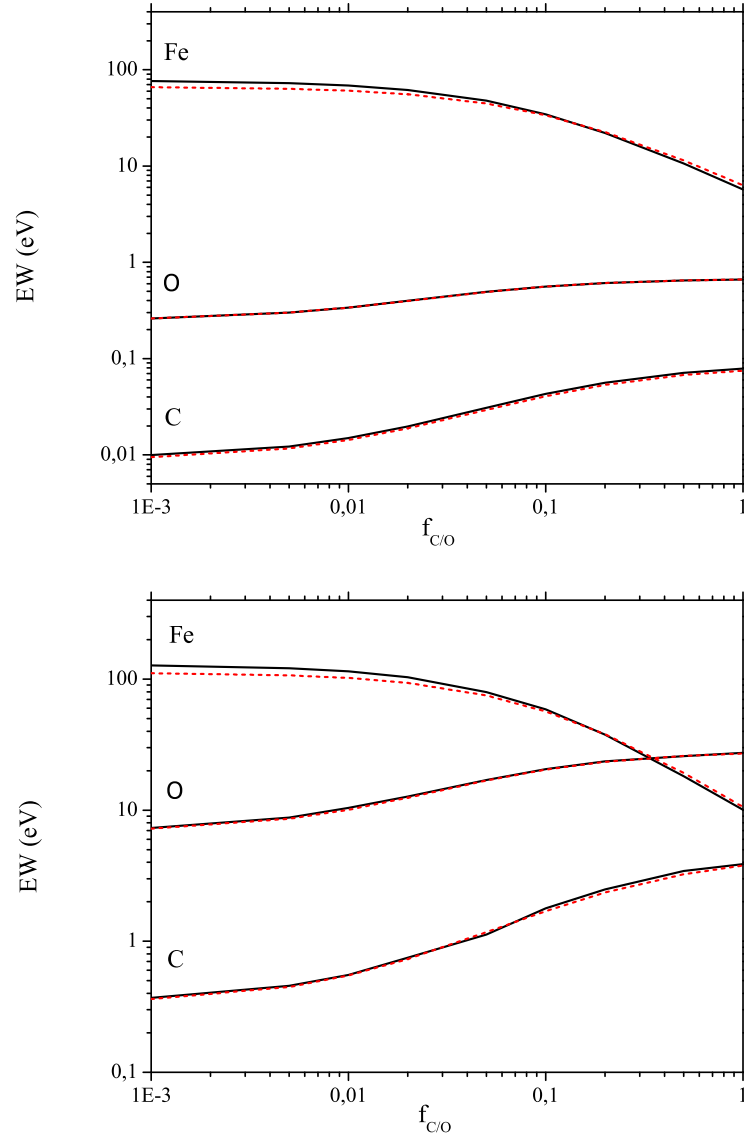
Figure 2.3:    The equivalent widths of Kα lines of C, O and Fe plotted against $f_{C/O}$, the fraction of H and He "converted" to C and O (section 2.5.2, eq.2.27).  The upper panel shows results for a power law incident spectrum with photon index of $\Gamma = 1.9$ and the lower panel – for black body radiation with kT=2.5 KeV. Black solid lines show results of Monte-Carlo calculations, the dashed lines (red in the color version) were computed in the single scattering approximation as described in Section 2.4.

is given by the following expression.

$$\delta S_{\mathrm{refl}}(E, \vec{n}_{\mathrm{out}}) = S_{\mathrm{pr}}(E, \vec{n}_{\mathrm{in}})\, \delta\Omega_{\mathrm{in}}$$

$$\int_0^\infty dz \sec\theta_{\mathrm{in}}\, e^{-n\sigma_{\mathrm{tot}}(E)z\sec\theta_{\mathrm{in}}}\, n\sigma_{\mathrm{sc}}(E) P_{\mathrm{sc}}(\vec{n}_{\mathrm{in}}, \vec{n}_{\mathrm{out}})$$

$$e^{-n\sigma_{\mathrm{tot}}(E)z\sec\theta_{\mathrm{out}}} \tag{2.2}$$

where $S_{\mathrm{pr}}(\mathrm{E}, \tilde{\mathrm{n}})$ is the spectral intensity of the primary radiation, axis $z$ is normal to the surface of the atmosphere and is directed inwards, $\delta\Omega_{\mathrm{in}}$ is an infinitesimal solid angle around the direction of incidence $\vec{n}_{\mathrm{in}}$, $\theta_{\mathrm{in}}$ is its polar angle with respect to the axis $z$. The spectral intensity of the reflected emission is computed at the direction $\vec{n}_{\mathrm{out}}$, which polar angle is $\theta_{\mathrm{out}}$. $P_{\mathrm{sc}}(\vec{n}_{\mathrm{in}}, \vec{n}_{\mathrm{out}})$ is the probability that the photon, entering the medium from the direction $\vec{n}_{\mathrm{in}}$ is scattered in the direction $\vec{n}_{\mathrm{out}}$, it is normalized so that:

$$\int P_{\mathrm{sc}}(\vec{n}_{\mathrm{in}}, \vec{n}_{\mathrm{out}})\, d\Omega_{\mathrm{out}} = 1 \tag{2.3}$$

The $n$ is the density of the material and $\sigma_{\mathrm{tot}} = \sigma_{\mathrm{abs}} + \sigma_{\mathrm{sc}}$ is the total cross section. The absorption cross section due to photoionization $\sigma_{\mathrm{abs}}$ is given by the following expression

$$\sigma_{\mathrm{abs}}(E) = \sum_{Z=1}^{30} A_Z \sigma_Z(E) \tag{2.4}$$

where we account for all elements from $Z = 1$ to $Z = 30$, $A_{\mathrm{Z}}$ is the abundance of element Z by the particle number, and $\sigma_{\mathrm{Z}}$ is the photoionization cross-section for all shells of element Z. It is calculated using the second version of the Verner et al. (1996) subroutine. $\sigma_{\mathrm{sc}}$ is the scattering cross section per hydrogen atom, given by

$$\sigma_{\mathrm{sc}}(E) = \sum_{Z=1}^{30} Z A_{\mathrm{Z}} \sigma_{\mathrm{T}} \tag{2.5}$$

where $\sigma_{\mathrm{T}}$ is the Thomson cross section. Note that we consider Compton scattering in the low energy limit and ignore change of the photon frequency during scattering in deriving eq.(2.2).

For a semi-infinite atmosphere, the reflected spectrum does not depend on the density of the material, only on its chemical composition.

We assume for simplicity that the energy and angular dependencies of the primary radiation can be factorized:

$$S_{\mathrm{pr}}(E, \vec{n}) = S_0(E)\, P_{\mathrm{pr}}(\vec{n}) \tag{2.6}$$

where the $P_{\mathrm{pr}}(\vec{n}_{\mathrm{in}})$ describes the angular distribution of the primary radiation and is normalized so that

$$\int P_{\mathrm{pr}}(\vec{n})\, d\Omega = 1 \tag{2.7}$$

and $S_0(\mathrm{E})$ is proportional to the total luminosity of the primary emission and has units of $\mathrm{phot\, sec^{-1}\, cm^{-2}\, keV^{-1}}$. We evaluate the reflected emission within solid angle $\Delta\Omega_{\mathrm{out}}$ around direction of interest $\vec{n}_{\mathrm{out}}$:

$$\tilde{S}_{\mathrm{refl}}(E) = \int_{\Delta\Omega_{\mathrm{out}}} S_{\mathrm{refl}}(E, \vec{n}_{\mathrm{out}})\, d\Omega \tag{2.8}$$

Integrating eq. A1 over ingoing and outgoing directions and from z=0 to $z = \infty$ we obtain the following expression for the reflected continuum $\tilde{S}_{\mathrm{refl}}$

$$\tilde{S}_{\mathrm{refl}}(E) = S_0(E)\, \frac{\sigma_{\mathrm{sc}}(E)}{\sigma_{\mathrm{sc}}(E) + \sigma_{\mathrm{abs}}(E)}\, R_{\mathrm{refl}} \tag{2.9}$$

where the factor $R_{\mathrm{refl}}$ accounts for the geometry of the problem and is given by

$$\begin{aligned}
R_{\mathrm{refl}} = {} & \int_{\Delta\Omega_{\mathrm{in}}} d\Omega_{\mathrm{in}} P_{\mathrm{pr}}(\vec{n}_{\mathrm{in}}) \int_{\Delta\Omega_{\mathrm{out}}} d\Omega_{\mathrm{out}} \\
& \sec\theta_{\mathrm{in}} \left(\sec\theta_{\mathrm{in}} + \sec\theta_{\mathrm{out}}\right)^{-1} P_{\mathrm{sc}}(\vec{n}_{\mathrm{in}}, \vec{n}_{\mathrm{out}}),
\end{aligned} \tag{2.10}$$

For Thomson scattering $P_{\mathrm{sc}}(\vec{n}_{\mathrm{in}}, \vec{n}_{\mathrm{out}})$ depends only on the scattering angle $\theta_{\mathrm{sc}}$ and is given by the standard Rayleigh formula

$$P_{\mathrm{sc}}(\theta_{\mathrm{sc}}) = \frac{3}{8\pi} \frac{(1 + \cos^2\theta_{\mathrm{sc}})}{2}, \tag{2.11}$$

Ignoring angular dependences,

$$R_{\mathrm{refl}} \propto \frac{\Delta\Omega_{\mathrm{in}}}{4\pi} \frac{\Delta\Omega_{\mathrm{out}}}{4\pi} \tag{2.12}$$

For the case of isotropic incident radiation and reflected emission integrated over all outgoing angles (the geometry assumed in Fig. 2.3, 2.6) eq. A9 yields $R_{\text{refl}} = 1/8$.

Using the same approach and taking into account the fluorescent yield, we can compute the fluorescent line flux $F_{\text{line}}$ (phot $\text{sec}^{-1}\,\text{cm}^{-2}\,\text{sr}$):

$$\delta F_{\text{line}}(\vec{n}_{\text{out}}) = \delta\Omega_{\text{in}} \int_{E_{\text{K}}}^{\infty} dE\, S_{\text{pr}}(E, \vec{n}_{\text{in}})$$

$$\int_{0}^{\infty} dz \sec\theta_{\text{in}}\, e^{-n\sigma_{\text{tot}}(E)z\sec\theta_{\text{in}}} A_{\text{Z}} n\, \sigma_{\text{K,Z}} Y_{\text{Z}} P_{\text{line}}(\vec{n}_{\text{out}})$$

$$e^{-n\sigma_{\text{tot}}(E_{\text{line}})z\sec\theta_{\text{out}}} \qquad (2.13)$$

In the above expression, $\sigma_{\text{K,Z}}$, is the K-shell absorption cross section of element Z and $Y_{\text{Z}}$ is the fluorescence yield of its $K_\alpha$ line, $E_{\text{line}}$ is the $K_\alpha$ line energy and $E_{\text{K}}$ is the energy of the K-edge. $P_{\text{line}}(\vec{n}_{\text{out}})$ is the angular distribution of the fluorescent emission, assumed to be isotropic ($P_{\text{line}}(\tilde{n}_{\text{out}}) = 1/4\pi$). Integrating over all angles and over $z = 0 \to \infty$ we obtain

$$\tilde{F}_{\text{line}} = \int_{E_{\text{K}}}^{\infty} S_0(E)G(E)dE \qquad (2.14)$$

where as before, tilde denotes integration over solid angle $\Delta\Omega_{\text{out}}$ and $G(E)$ is given by the following integral

$$G(E) = \int_{\Delta\Omega_{\text{in}}} d\Omega_{\text{in}} P_{\text{pr}}(\theta_{\text{in}}) \int_{\Delta\Omega_{\text{out}}} d\Omega_{\text{out}} P_{\text{line}}(\vec{n}_{\text{out}})$$
$$\left( \frac{Y_{\text{Z}} A_{\text{Z}}\, \sigma_{\text{K,Z}}(E) \sec\theta_{\text{in}}}{\sigma_{\text{tot}}(E) \sec\theta_{\text{in}} + \sigma_{\text{tot}}(E_{\text{line}}) \sec\theta_{\text{out}}} \right) \qquad (2.15)$$

A more or less similar derivation for the line flux was also derived by Churazov et al. (2008). Similarly to $R_{\text{refl}}$, for the geometry of Fig. 2.3, 2.6 (semi-infinite slab illuminated by isotropic incident radiation, reflected emission integrated over all outgoing angles), eq. 2.15 can be integrated analytically to give:

$$G(E) = Y_{\text{Z}} A_{\text{Z}}\, \sigma_{\text{K,Z}}(E)\, \frac{G1}{G2} \qquad (2.16)$$

Where G1 is given by,

$$
\begin{aligned}
G1 = {}& \sigma_{\mathrm{tot}}(E_{\mathrm{line}})[\sigma_{\mathrm{tot}}(E) + \sigma_{\mathrm{tot}}(E_{\mathrm{line}}) \ln[\sigma_{\mathrm{tot}}(E_{\mathrm{line}})]] \\
& + [\sigma_{\mathrm{tot}}(E)^2 - \sigma_{\mathrm{tot}}(E_{\mathrm{line}})^2] \ln[\sigma_{\mathrm{tot}}(E) + \sigma_{\mathrm{tot}}(E_{\mathrm{line}})] \\
& \hspace{5cm} - \sigma_{\mathrm{tot}}(E)^2 \ln[\sigma_{\mathrm{tot}}(E)]
\end{aligned}
\tag{2.17}
$$

and G2 is given by,

$$
G2 = 8\,\sigma_{\mathrm{tot}}(E)^2 \sigma_{\mathrm{tot}}(E_{\mathrm{line}})
\tag{2.18}
$$

To characterize the strength of emission lines we evaluate their equivalent widths with respect to the total continuum emitted within the solid angle $\Delta\Omega_{\mathrm{out}}$ around the direction of interest.

$$
EW = \frac{\tilde{F}_{\mathrm{line}}}{\tilde{S}_{\mathrm{tot}}(E_{\mathrm{line}})},
\tag{2.19}
$$

The total continuum includes both the reflected continuum, given by eq. (2.9) and the fraction of the primary continuum emitted in the solid angle $\Delta\Omega_{\mathrm{out}}$

$$
\tilde{S}_{\mathrm{tot}}(E) = \tilde{S}_{\mathrm{refl}}(E) + \tilde{S}_{\mathrm{pr}}(E)
\tag{2.20}
$$

where, similarly to $\tilde{S}_{\mathrm{refl}}(\mathrm{E})$,

$$
\tilde{S}_{\mathrm{pr}}(E) = \int_{\Delta\Omega_{\mathrm{out}}} S_{\mathrm{pr}}\left(E, \vec{n}_{\mathrm{out}}\right) d\Omega_{\mathrm{out}}
\tag{2.21}
$$

Thus, using equations 2.9 and 2.10 for the reflected continuum, eqs. 2.14 and 2.15 for the fluorescent line flux, the equivalent width of the fluorescent line can be computed from eqs. 2.19–2.21. Comparison with Monte-Carlo calculations show that the single scattering approximation works nearly perfectly at low energies, $E \lesssim 2$ keV, where absorption dominates scattering. At higher energies, multiple scattering becomes more important, resulting in a $\sim 10\%$ offset between analytical and Monte-Carlo results for the iron $K_\alpha$ line. This is further illustrated by Figs. 2.3 and 2.6 showing dependence of equivalent widths of various fluorescent lines on the chemical abundances computed in single scattering approximation and using the Monte-Carlo code described in the following section.
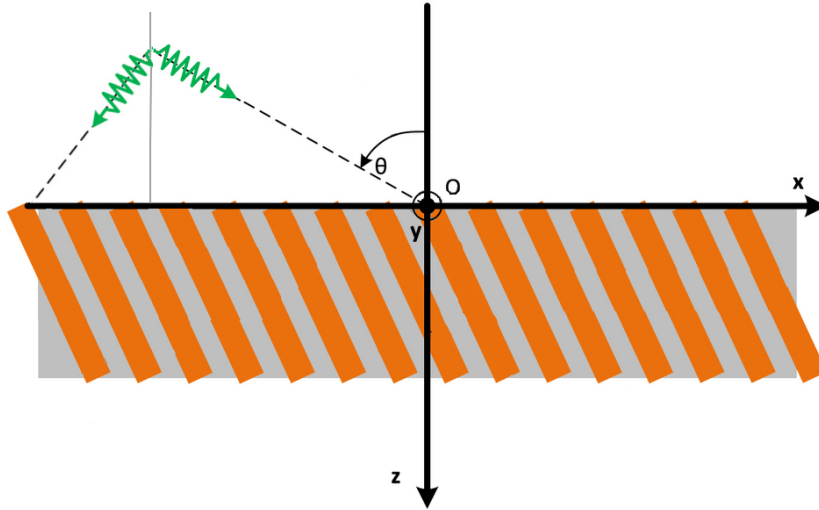
Figure 2.4: A semi-infinite plane, illuminated from the top by an isotropically emitting point source. Incident photons can only escape if they end up at $z < 0$.

## 2.5 Results

### 2.5.1 Simulations of X-ray reflection

Below, we briefly describe the main features of our X-ray reflection code. The main steps of the code and its results are discussed in this section, and its predictions are used in Chapters 3 and 4. The simulation was created using Monte Carlo techniques and is largely based on the prescription by Pozdnyakov, Sobol & Sunyaev (1983).

To simulate the illuminated disk, we assume a plane-parallel semi-infinite geometry. The plane is illuminated from the top by an isotropically emitting point source, in a lamppost configuration (Fig. 2.4). Each incident photon enters the material at a randomly selected incidence angle $\theta \in [0, \pi/2]$ and has a randomly assigned energy, selected from either a power law or a black body distribution. The energy range of the distributions, the photon index of the power law and the temperature of the black body are selected by the user.

Once a photon enters the plane of the simulated material, it traverses a distance – known as its free path – until it is either scattered or absorbed.

The free path ($s$) is selected from an exponential distribution and is given by:

$$s = -\frac{ln\xi}{(\sigma_{\mathrm{abs}} + \sigma_{\mathrm{sc}}) N_H}, \tag{2.22}$$

where $\sigma_{\mathrm{sc}}$ is the scattering cross-section, $\sigma_{\mathrm{abs}}$ the absorption cross-section, $N_H$ is the area density of the material and $\xi$ is a uniformly distributed random number, with $\xi \in [0, 1]$. The absorption cross-section is given by:

$$\sigma_{\mathrm{abs}}(E) = \sum_{Z=1}^{30} A_Z \sigma_Z(E), \tag{2.23}$$

where Z is the atomic number of each element in the disk, for hydrogen up to zinc, $\sigma_Z(E)$ is the photoionization cross-section of element Z, for a given photon energy $E$ and $A_Z$ is the abundance of the Z-element. Photoionization cross sections for given abundances are calculated using the analytical fits for partial photoionization cross-sections from Verner et al. (1996). The scattering cross-section is calculated by:

$$\sigma_{\mathrm{sc}}(E) = \sum_{Z=1}^{30} Z A_Z \sigma_{\mathrm{KN}}, \tag{2.24}$$

where $\sigma_{\mathrm{KN}}$ is the cross-section for Compton scattering, calculated using the Klein-Nishina formula (Klein & Nishina, 1929).

When the photon has traversed its free path, it will be either scattered or absorbed. The probability of absorption is given by:

$$P_{\mathrm{abs}} = \frac{\sigma_{\mathrm{abs}}}{\sigma_{\mathrm{abs}} + \sigma_{\mathrm{sc}}}. \tag{2.25}$$

If the photon is scattered, its energy after the scattering will be given by the Compton formula. Namely,

$$E_{\mathrm{n+1}} = \frac{E_{\mathrm{n}}}{1 + (E_{\mathrm{n}}/m_{\mathrm{e}} c^2)(1 - \cos\theta_{\mathrm{sc}})}, \tag{2.26}$$

where $E_{\mathrm{n}}$ and $E_{\mathrm{n+1}}$ is the photon energy before and after the scattering, $m_{\mathrm{e}}$ is the electron mass and $\theta_{\mathrm{sc}}$ the scattering angle. The latter is randomly selected from the Klein-Nishin distribution. For low energy photons (e.g. 1 keV) forwards and backwards scatterings are favored, as described by Rayleigh
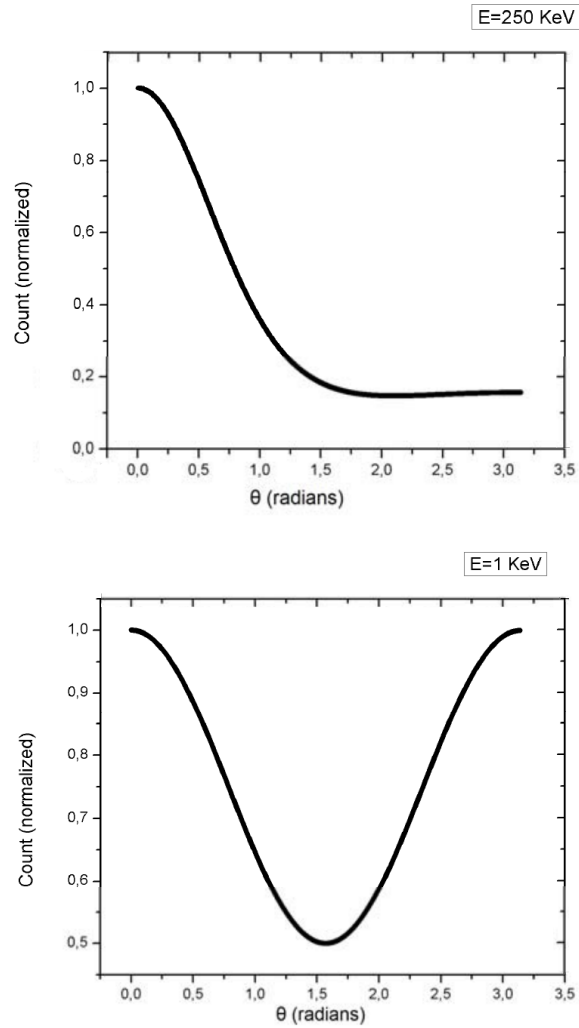
Figure 2.5: Klein-Nishina distribution for scattering angle. **Top:** The case of a high energy photon where forward scattering is favored. **Bottom:** The case of a low energy photon, where the angular distribution is the same as in Rayleigh scattering

scattering. For a high energy photon (e.g. $>100\,\text{keV}$) forward scattering is favored (Fig. 2.5)

If the photon is absorbed, the code calculates the probability of absorption by each of the different elements that compose the disk material (for details see eq. 2.1 and Section 2.4). Once the absorbing element has been determined, the probability of fluorescence is calculated, based on the known K-shell fluorescence yield of each element (Bambynek et al., 1972). If fluorescence occurs the photon is remitted at the point it was absorbed with an energy that corresponds to the K$\alpha$ or K$\beta$ emission of the element responsible for the photon's absorption. The direction of the remitted photon is randomly selected from a uniform, isotropic distribution. If the photon is not remitted, it is considered "lost", the loop closes and a new photon enters the material.

Since the disk is modeled as a semi-infinite plane, the incident photons can only escape from the illuminated surface (z<0 in Fig. 2.4). The photons that escape are registered either at a specific angle or integrated over all viewing angles. They are placed in energy bins and the reflected spectrum is formed, including K$\alpha$ and K$\beta$ emission lines for all elements from carbon to zinc. Lastly, the code calculates the equivalent width of each line with respect to the total emission, which includes the reflected emission mixed with the primary radiation (see Section 2.4). The abundances of all disk elements can vary at will, thus allowing the user to investigate the effects of different abundance patterns on the reflected continuum and the equivalent widths of the emission lines.

X-ray binaries are known to have two distinct spectral states: a bright high/soft state and a less luminous low/hard state (e.g Gilfanov, 2010). In the hard spectral state, Comptonization of soft photons on hot electrons is the most likely mechanism for the creation of the hard spectral component, which, in the energy range of interest, usually has a power law shape. In the soft state, the primary emission may originate in the accretion disk itself or in the the boundary layer on the surface of the neutron star (e.g. Sunyaev & Shakura, 1986; Inogamov & Sunyaev, 1999; Popham & Sunyaev, 2001). Correspondingly, the incident spectrum is represented by either a power law in which case it is characterized by a photon index $\Gamma$, or by a thermal component originating in the NS boundary layer. In the latter case, we approximated the boundary layer radiation with a black body spectrum with kT = 2.5 keV (Gilfanov, Revnivtsev, & Molkov, 2003).

## 2.5.2 Reflection from C/O-rich material

In order to investigate the dependence of the line strengths on the C/O abundance we consider a sequence of chemical compositions with increasing C/O abundance. Abundances of H and He were reduced along the sequence so that the total number of nucleons was conserved. Abundances of other elements (by mass) remained fixed at their solar values, as well as the abundance ratio of carbon and oxygen. The position along the sequence is defined by the parameter

$$f_{C/O} = \frac{n_C m_C + n_O m_O}{n_H m_H + n_{He} m_{He} + n_C m_C + n_O m_O} \tag{2.27}$$

where $n_i$ is concentration of the element $i$ and $m_i$ is its atomic weight. Obviously, $f_{C/O}$ has the meaning of the fraction of hydrogen and helium "converted" to carbon and oxygen and changes from 0 to 1. We performed calculations of the reflected spectrum and computed the equivalent widths of fluorescent lines on a grid of values of $f_{C/O}$ in this range. The calculations were performed with Monte-Carlo simulations and using analytical expressions from Section 2.4. The incident photons were assumed to illuminate the disk surface isotropically and the reflected emission was integrated over all outgoing directions. The results are shown in Fig. 2.3 for carbon, oxygen and iron $K_\alpha$ lines, for both types of the primary emission spectrum. The plots show the equivalent widths of lines versus $f_{C/O}$.

The overall behavior of equivalent widths is similar for both types of incident spectrum. It is mostly determined by $P_Z$ (Fig. 2.1) and, as expected, the curves have shapes similar to those in Fig. 2.2. Initially, the EWs of carbon and oxygen lines increase nearly in direct proportion to their abundance, however they quickly saturate at $f_{C/O} \sim 20\%$. This corresponds to the oxygen overabundance of $A_O/A_{O,\odot} \sim 10$ in Fig. 2.2. The initial increase of the oxygen line EW is somewhat milder than that of carbon due to screening of oxygen by carbon itself. In the case of the power law incident spectrum, the EWs of carbon and oxygen lines remain at sub-eV level, even for a totally C/O-dominated composition. For a black body incident spectrum, however, these lines can become rather prominent at large C/O-abundances, reaching a value of $\sim 20\,\mathrm{eV}$ for oxygen and $\sim 2\,\mathrm{eV}$ for carbon. The iron line is the most prominent fluorescent line for solar abundances. Nevertheless, for both types of the incident spectrum, its EW drops below $\sim 10$ eV for the C/O dominated composition.
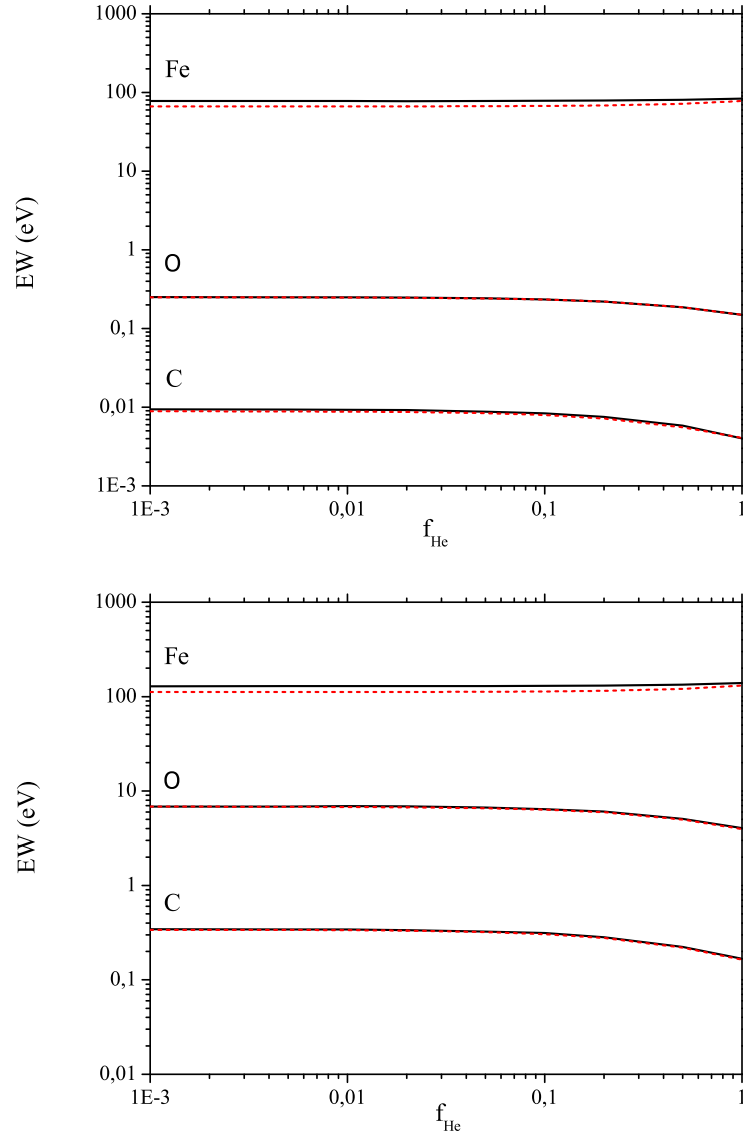
Figure 2.6: The equivalent widths of K$\alpha$ lines of C, O and Fe are plotted against $f_{He}$, the fraction of H "converted" to He (cf. eq.2.27). The upper panel shows results for a power law incident spectrum with photon index of $\Gamma = 1.9$ and the lower panel – for black body radiation with kT=2.5 keV. Black solid lines show results of Monte-Carlo calculations, the dashed lines (red in the color version) were computed in the single scattering approximation as described in Section 2.4.

### 2.5.3   Reflection from He-rich material

We follow the same approach to investigate the dependence of the fluorescent lines strengths on the helium abundance as we used for C/O. The results are presented in Fig. 2.6, where we plot equivalent widths of carbon, oxygen and iron lines against $f_{\text{He}}$, defined similarly to $f_{\text{C/O}}$ in eq.(2.27).

Similar to the C/O case, the increased abundance of He would have a screening effect on the elements with the charge $Z > 2$, however, the effect is much milder than in the case of C/O dominated material. The reason is the much larger solar abundance of helium and the significant drop of its photoabsorption cross-section at the energies corresponding to K-edges of elements which $K_\alpha$ lines are in the X-ray domain. The latter factor is especially important for iron. Correspondingly, the overall effect is stronger for lines of low-Z elements, such as carbon and oxygen and is negligible for iron. For example, the equivalent widths of carbon and oxygen lines decrease by $\sim 2$ times in the He-dominated case. In Fig. 2.6, one can also notice a slight, $\sim 10\%$, increase of the EW of the iron relative to its solar value. This is a consequence of the definition of the abundance sequence, and does not have any physical meaning. It is caused by the decrease of the number of electrons, as H is being replaced by He along the abundance sequence.

### 2.5.4   Realistic WD compositions

We now compute equivalent widths of fluorescent lines for realistic abundance patterns expected for different types of white dwarfs. For these we used the results of García-Berro et al. (2008), Gil-Pons & García-Berro (2001) and Pandey et al. (2001) as detailed in the Section 2.2 and summarised in Table 2.1. The equivalent width of lines were computed with our Monte Carlo code assuming an isotropic point source above the disk surface (lamppost configuration). The reflected spectrum was integrated over all viewing angles. The results of these calculations are presented in the Table 2.2.

The results are qualitatively similar to those obtained in the previous subsections. Perhaps a new feature is the appearance of the neon line in the case of the O/Ne white dwarf, which becomes especially prominent in the case of a black body incident spectrum, where its equivalent width can reach $\sim 15$ eV.

Table 2.2: Equivalent width of prominent fluorescent lines for realistic white dwarf compositions. Results of Monte-Carlo calculations.

| Element | Energy keV | Power law | | | | Black Body | | | |
|---|---|---|---|---|---|---|---|---|---|
| | | Solar | He | C/O | O/Ne | Solar | He | C/O | O/Ne |
| C | 0.277 | 0.01 | < 0.01 | 0.11 | - | 0.35 | 0.24 | 8.21 | - |
| O | 0.525 | 0.25 | 0.03 | 0.40 | 0.72 | 7.10 | 0.70 | 13.8 | 31.0 |
| Ne | 0.849 | 0.19 | 0.20 | 0.06 | 0.76 | 3.14 | 3.19 | 1.00 | 14.8 |
| Na | 1.041 | 0.01 | 0.01 | < 0.01 | 0.23 | 0.09 | 0.10 | < 0.01 | 3.51 |
| Mg | 1.254 | 0.25 | 0.27 | < 0.01 | 0.37 | 2.90 | 3.17 | 0.10 | 4.36 |
| Si | 1.740 | 0.84 | 0.94 | 0.03 | 0.02 | 7.23 | 8.24 | 0.26 | 0.14 |
| S | 2.307 | 1.13 | 1.30 | 0.04 | 0.02 | 7.19 | 8.36 | 0.30 | 0.14 |
| Ar | 2.957 | 0.80 | 0.94 | 0.04 | 0.02 | 3.84 | 4.50 | 0.17 | 0.08 |
| Ca | 3.690 | 1.03 | 1.22 | 0.05 | 0.03 | 3.60 | 4.30 | 0.18 | 0.09 |
| Cr | 5.415 | 0.80 | 1.00 | 0.05 | 0.03 | 1.65 | 2.14 | 0.11 | 0.05 |
| Mn | 5.899 | 0.52 | 0.65 | 0.04 | 0.02 | 0.98 | 1.24 | 0.07 | 0.04 |
| Fe | 6.397 | 76.0 | 92.8 | 6.58 | 3.11 | 127 | 157 | 10.9 | 5.17 |
| Fe ($K_\beta$) | 7.058 | 12.6 | 15.7 | 1.17 | 0.54 | 17.3 | 21.6 | 1.60 | 0.80 |
| Ni | 7.470 | 5.86 | 7.00 | 0.68 | 0.33 | 7.75 | 9.37 | 0.92 | 0.44 |
| Ni ($K_\beta$) | 8.265 | 0.93 | 1.11 | 0.12 | 0.06 | 1.04 | 1.28 | 0.13 | 0.06 |

Equivalent widths are in eV. The line energies are from Bearden (1967). The abundance patterns for different types of white dwarfs used in these calculations are summarized in Table 2.1.

## 2.6   Discussion

Results of the previous section suggest that absence of a strong $K_\alpha$ line of iron at 6.4 keV in the spectrum of a UCXB should be considered as an indication of a C/O/Ne white dwarfs whereas the presence of such a line points at a helium-rich donor. There are, however, several factors which can modify this simple picture.

### 2.6.1   Gravitational sedimentation of metals

Gravitational settling of heavy elements operates efficiently in the surface layers of white dwarfs, its time scale being considerably shorter than the evolutionary time scale of an isolated white dwarf (e.g. Schatzman, 1958; Paquette et al., 1986). The result of the gravitational sedimentation is that the outer layers of the white dwarf envelope are depleted of metals on the time scales of $\sim 10^6$ yrs or shorter (Paquette et al., 1986; Dupuis et al., 1992). This explains the purity of spectra in the majority of white dwarfs, which show only spectral lines of hydrogen and helium.

Extrapolating these results to the UCXB case, one may expect that their accretion disks should be devoid of elements other than the main constituent of the white dwarf (H/He or C/O). However, although the diffusion time scale in the outermost layers is much shorter than the cooling time of an isolated white dwarf, the time scale on which the deeper layers of the white dwarf envelope are depleted of metals is rather long, much longer than the accretion time scale. As a result, the outer layers of the white dwarf envelope are removed faster than they are depleted of metals. The time dependent calculations of gravitational settling by Dupuis et al. show that time, required to deplete the outer $\sim 10^{-3}$ (by mass) of the white dwarf exceeds $\sim 10^8$ yrs. On the other hand, for the accretion rate of $\sim 10^{-9}$ $M_\odot$/yr, the outer layer of mass $\Delta M \sim 10^{-3}$ $M_\odot$ is removed within $\Delta t \sim 10^6$ yrs. Therefore we do not expect that gravitational settling of heavy elements is an important factor determining the composition of accretion disks in UCXBs. This conclusion is confirmed by detection of iron lines in the spectra of UCXBs with He-rich donors (Asai et al., 2000; Boirin et al., 2004).

## 2.6.2   Ionization state of the accretion disk

The material on the surface of the accretion disk may be ionized due to internal heating as well as due to irradiation. This can significantly modify the shape of the reflected emission and strengths of fluorescent lines. For example, if carbon and oxygen are fully ionized, they do not contribute to the ionization cross-section and the fluorescent line of iron will have its nominal, $\sim$solar abundance strength even for the C/O-dominated disk. On the other hand, partial ionization of oxygen would lead to appearance of much stronger lines of OVII–OVIII, but would not eliminate the effect of screening of elements with higher charge $Z$. Correspondingly, the iron line would remain suppressed in this case.

   Illumination of the accretion disk by X-ray photons produced in the vicinity of the compact object (e.g. in the boundary layer) results in the appearance of the ionized skin – a thin surface layer of highly ionized material (Nayakshin, Kazanas & Kallman, 2000). Beneath this layer, the disk remains in the ionization state determined by heating due to viscous dissipation. The Thomson optical depth $\tau$ of the ionized skin is determined by the "gravity parameter",

$$A = \frac{H}{R}\frac{L_{\mathrm{Edd}}}{L_{\mathrm{x}}\cos\theta} \tag{2.28}$$

where $H/R$ is the aspect ratio of the Shakura Sunyaev accretion disk, $L_{\mathrm{x}}$ is the luminosity of the irradiating source, $L_{\mathrm{Edd}}$ – Eddington luminosity for a neutron star and $\theta$ – the angle of the incident radiation with respect to the normal to the disk surface. This parameter characterizes the strength of gravity relative to that of radiation pressure. For typical parameters of UCXBs, $H/R \sim$ few$\times 10^{-2}$, $L_{\mathrm{x}}/L_{\mathrm{Edd}} \sim 10^{-2}-10^{-1}$ and assuming $\cos\theta \sim 0.1$ we obtain $A \sim 3-30$. According to Nayakshin, Kazanas & Kallman, this value corresponds to low to moderate illumination, in which case the Thomson optical depth of the ionized skin is small and it does not significantly distort the spectrum of radiation reflected off the inner layers of the disk. The ionization state of these layers is determined by the viscous dissipation.

   The effective temperature of the Shakura-Sunyaev disk due to viscous dissipation (Shakura & Sunyaev, 1973) is

$$T_{\mathrm{eff}} = \left(\frac{3GM\dot{M}}{8\pi\sigma r_{\mathrm{o}}{}^3}\right)^{1/4}\left(\frac{r_{\mathrm{o}}}{r}\right)^{3/4}\left(1-\sqrt{r_{\mathrm{o}}/r}\right)^{1/4} \tag{2.29}$$

where $\sigma = 5.67 \cdot 10^{-5} \mathrm{erg\,cm^{-2}\,s^{-1}\,K^{-4}}$ is the Stefan-Boltzmann constant, $M$ is the mass of the accretor ($\sim 1.4\,M_\odot$ for a neutron star), $\dot{M}$ the mass accretion rate and $r_\mathrm{o}$ is the inner radius of the disk, which in the case of the soft state of a neutron star is equal to its radius. For the mass accretion rate in the $\dot{M} \sim 10^{-10} - 10^{-8}\,M_\odot/\mathrm{yr}$ range (corresponding to $L_\mathrm{X} \sim 10^{36} - 10^{38}\mathrm{erg\,s^{-1}}$) the maximum disk temperature ranges from $\sim 2 \cdot 10^6$ to $\sim 8 \cdot 10^6$ K. Obviously, hydrogen and helium are fully ionized throughout the most of the accretion disk at any value of the accretion rate relevant to UCXBs (as they should be, in order for accretion to proceed in the high viscosity regime). Iron is virtually never fully ionized, its ionization state being below FeXXIII in the entire temperature range of interest, $T_\mathrm{eff} \lesssim 8 \cdot 10^6$ K. The ionization states of carbon, oxygen and neon, however, depend critically on the mass accretion rate. Indeed, for plasma in the collisional ionization equilibrium, in coronal approximation, 90% of carbon (oxygen) is in the fully ionized state at temperatures of $\sim 1.6 \cdot 10^6$ ($\sim 3.5 \cdot 10^6$) K (Shull & van Steenberg, 1982). Therefore, even at the moderate luminosity of $\sim 10^{37}$ erg/s, carbon is expected to be ionized in a significant part of the inner disk, out to $r \sim 10 r_\mathrm{o}$. Oxygen and neon, on the other hand, are fully ionized in the inner disk at high luminosities, $\sim 10^{38}$ erg/s, but remain only partially ionized at moderate and low luminosities, $L_\mathrm{X} \sim 10^{36} - 10^{37}$ erg/s.

Thus, one should expect luminosity dependence of the iron line strength in UCXBs. At low and moderate luminosities, it is determined by the chemical composition of the accreting material, as described in the previous section. In particular, it remains at the solar value in systems with He-rich donors and is suppressed in the case of a C/O/Ne donor. As luminosity[2] approaches $\sim 10^{38}$ erg/s, the iron line should recover its nominal strength, determined by the abundance of iron in the accreting material.

### 2.6.3   Reflection from the white dwarf surface

For a binary system consisting of a $1.4 M_\odot$ NS accretor and a $0.7 M_\odot$ WD donor, the Roche lobe of the WD subtends a solid angle of $\sim 0.3\,\mathrm{sr}$ as viewed from the neutron star. In the idealized lamppost geometry the solid angle of the accretion disk is $\Omega \sim 2\pi$. Therefore, the donor star does not contribute significantly to the total reflected emission. However, the lamppost geometry

---

[2] Determination of the exact value of luminosity at which the transition happens, requires detailed calculations of the ionization state of the material at the surface of the accretion disk and is beyond the scope of this paper.

is obviously a too crude approximation. In more realistic geometries, taking into account the geometry and emission diagram of the primary emission, the role of reflection from the donor star may no longer be negligible.

For a $T_{\text{eff}} \sim 10^4$ K white dwarf, helium is expected to be partly or fully ionized, whereas carbon, oxygen and iron should be only partly ionized (Dupuis et al., 1992). Therefore, for a He white dwarf, the fluorescent line of iron should have its nominal strength. For a C/O white dwarf the iron line should be suppressed due to screening by carbon and oxygen, as described above. Depending on the exact value of the temperature in the white dwarf photosphere, carbon and oxygen may be in the medium to high ionization state. In the latter case, one may expect appearance of strong resonant lines of their highly ionized species. Among these, of special interest would be lines of oxygen.

### 2.6.4   Iron abundance

In order to determine the iron abundance, we relied on the assumption that the total mass of elements, heavier than O/Ne, in the donor star, does not change. This was motivated by the fact that nuclear reaction chains do not involve heavy elements. Moreover, the heavier elements were fixed at their solar mass fractions, in order to make comparisons between spectra originating in H-rich and H-poor atmospheres. These assumptions, along with the requirement to conserve the total number of nucleons, effectively limited the maximal C,O,Ne/Fe abundance ratios. This in turn limited the minimal value of the iron line EW at small but moderate values of $\sim$ several eV (Fig. 2.3, Table 2.2). However, if one allowed further increase of the O/Fe abundance ratio, the equivalent width of the iron line can decrease to arbitrarily small numbers, in inverse proportion to this ratio, as illustrated by the Fig. 2.2.

## 2.7   Summary and conclusions

We have shown that non-solar composition of the donor star in ultra-compact X-ray binaries may have a dramatic effect on the reflected spectral component in UCXBs, significantly modifying the strength of fluorescent lines of various elements.

To identify the main trends, we considered an idealized case of an optically thick slab of neutral material with significantly non-solar abundances. We considered two abundance patterns, corresponding to a He and C/O white dwarf. We found that from the observational point of view, the non-solar composition of the reprocessing material most pronouncedly affects the strength of the fluorescent line of iron at 6.4 keV. Although increase of the carbon and oxygen abundances does lead to some increase of the strengths of corresponding fluorescent lines, their equivalent widths saturate at the (sub-)eV level due to the effect of self-screening. On the other hand, the equivalent width of iron decreases nearly in inverse proportion to the C/O abundance and the line is expected to be significantly fainter for the chemical composition of the C/O white dwarf. This is caused by the screening of the presence of heavy elements by oxygen. In C/O-dominated material, the dominant interaction process for a $E \gtrsim 7$ keV photon is absorption by oxygen rather than by iron, contrary to the case of solar composition. Screening by helium is significantly less important, due to its lower ionization threshold. Moreover, helium is expected to be fully ionized in the accretion disks of UCXBs. Consequently, in the case of He-rich reprocessing material, fluorescent lines of major elements are near their nominal, solar abundance strength. Thus, the equivalent width of the fluorescent line of iron can be used for diagnostics of the donor star in UCXBs by means of X-ray spectroscopy.

In the realistic case of reflection in UCXBs, gravitational settling of elements and ionization of the disk material may, potentially, complicate and modify this picture. Simple comparison of the diffusion time in white dwarf envelope and the accretion time scale suggests that gravitational settling is not fast enough to deplete iron and other heavy elements in the accreting material. However, a more accurate consideration of the physical state of a Roche-lobe filling, mass losing white dwarf may still be needed for the final conclusion.

Ionization of the disk material at high mass accretion rate may lead to luminosity dependence of the discussed effects. In particular, as oxygen in the inner parts of the C/O-dominated disk becomes fully ionized at high mass accretion rate, its screening effect vanishes and the iron line should be restored to its nominal value, determined by the abundance of iron in the accretion disk. Comparison of ionization curves with the effective temperature distribution in the Shakura-Sunyaev accretion disk suggests that it should happen at the $\log(L_\mathrm{X}) \sim 37.5 - 38$ level. At lower luminosities, $\log(L_\mathrm{X}) \lesssim 37$, oxygen in the inner disk is in the low- to medium ionization state and the

idealized picture outlined above holds, at least qualitatively, and the strength of the 6.4 keV iron line may be used for diagnostics of the nature of the donor star. In particular, its absence points at the C/O or O/Ne white dwarf, while its presence suggests a He-rich donor.

# Bibliography

Althaus L. G., Córsico A. H., Isern J., García-Berro E., 2010, A&A Rev., 18, 471

Asai K., Dotani T., Nagase F., Mitsuda K., 2000, ApJS, 131, 571

Bai T., 1979, Sol. Phys., 62, 113

Ballantyne D. R., Fabian A. C., Ross R. R., 2002, MNRAS, 329, L67

Ballantyne D. R., Ross R. R., Fabian A. C., 2001, MNRAS, 327, 10

Bambynek W., Crasemann B., Fink R. W., Freund H.-U., Mark H., Swift C. D., Price R. E., Rao P. V., 1972, Reviews of Modern Physics, 44, 716

Basko M. M., 1978, ApJ, 223, 268

Basko M. M., Sunyaev R. A., Titarchuk L. G., 1974, A&A, 31, 249

Bearden J. A., 1967, Reviews of Modern Physics, 39, 78

Bildsten L., 1995, ApJ, 438, 852

Bildsten L., Deloye C. J., 2004, ApJ, 607, L119

Boirin L., Parmar A. N., Barret D., Paltani S., Grindlay J. E., 2004, A&A, 418, 1061

Cackett E. M. et al., 2010, ApJ, 720, 205

Churazov E., Sazonov S., Sunyaev R., Revnivtsev M., 2008, MNRAS, 385, 719

Costantini E. et al., 2012, A&A, 539, A32

Cumming A., 2003, ApJ, 595, 1077

Dupuis J., Fontaine G., Pelletier C., Wesemael F., 1992, ApJS, 82, 505

Feldman U., 1992, Phys. Scr, 46, 202

García-Berro E., Althaus L. G., Córsico A. H., Isern J., 2008, ApJ, 677, 473

George I. M., Fabian A. C., 1991, MNRAS, 249, 352

Gil-Pons P., García-Berro E., 2001, A&A, 375, 87

Gilfanov M., 2010, in Lecture Notes in Physics, Berlin Springer Verlag, Vol. 794, Lecture Notes in Physics, Berlin Springer Verlag, Belloni T., ed., p. 17

Gilfanov M., Churazov E., Revnivtsev M., 1999, A&A, 352, 182

Gilfanov M., Revnivtsev M., Molkov S., 2003, A&A, 410, 217

Grevesse N., Sauval A. J., 1998, Space Sci. Rev., 85, 161

Iben, Jr. I., 1983, ApJ, 275, L65

Iben, Jr. I., Tutukov A. V., 1985, ApJS, 58, 661

Iben, Jr. I., Tutukov A. V., 1987, ApJ, 313, 727

Iben, Jr. I., Tutukov A. V., Yungelson L. R., 1995, ApJS, 100, 233

Inogamov N. A., Sunyaev R. A., 1999, Astronomy Letters, 25, 269

Kaplan D. L., Bildsten L., Steinfadt J. D. R., 2012, ApJ, 758, 64

Kawaler S. D., 1995, in Saas-Fee Advanced Course 25: Stellar Remnants, Benz A. O., Courvoisier T. J.-L., eds., p. 1

Klein O., Nishina T., 1929, Zeitschrift fur Physik, 52, 853

Kuulkers E. et al., 2010, A&A, 514, A65

Lightman A. P., White T. R., 1988, ApJ, 335, 57

Madej O. K., Jonker P. G., 2011, MNRAS, 412, L11

Madej O. K., Jonker P. G., Fabian A. C., Pinto C., Verbunt F., de Plaa J., 2010, MNRAS, 407, L11

Matt G., Fabian A. C., Ross R. R., 1993, MNRAS, 262, 179

Nayakshin S., Kazanas D., Kallman T. R., 2000, ApJ, 537, 833

Nelemans G., 2005, in Astronomical Society of the Pacific Conference Series, Vol. 330, The Astrophysics of Cataclysmic Variables and Related Objects, Hameury J.-M., Lasota J.-P., eds., p. 27

Nelemans G., Jonker P. G., Marsh T. R., van der Klis M., 2004, MNRAS, 348, L7

Nelemans G., Jonker P. G., Steeghs D., 2006, MNRAS, 370, 255

Nelemans G., Yungelson L. R., van der Sluys M. V., Tout C. A., 2010, MNRAS, 401, 1347

Nelson L. A., Rappaport S. A., Joss P. C., 1986, ApJ, 311, 226

Ng C., Díaz Trigo M., Cadolle Bel M., Migliari S., 2010, A&A, 522, A96

Pandey G., Kameswara Rao N., Lambert D. L., Jeffery C. S., Asplund M., 2001, MNRAS, 324, 937

Paquette C., Pelletier C., Fontaine G., Michaud G., 1986, ApJS, 61, 197

Podsiadlowski P., Rappaport S., Pfahl E. D., 2002, ApJ, 565, 1107

Popham R., Sunyaev R., 2001, ApJ, 547, 355

Pozdnyakov L. A., Sobol I. M., Sunyaev R. A., 1983, Astrophysics and Space Physics Reviews, 2, 189

Rappaport S., Joss P. C., 1984, ApJ, 283, 232

Ritossa C., Garcia-Berro E., Iben, Jr. I., 1996, ApJ, 460, 489

Ross R. R., Fabian A. C., 1993, MNRAS, 261, 74

Savonije G. J., de Kool M., van den Heuvel E. P. J., 1986, A&A, 155, 51

Schatzman E. L., 1958, White dwarfs

Shakura N. I., Sunyaev R. A., 1973, A&A, 24, 337

Shull J. M., van Steenberg M., 1982, ApJS, 48, 95

Sunyaev R. A., Shakura N. I., 1986, Soviet Astronomy Letters, 12, 117

Tutukov A. V., Yungelson L. R., 1993, Astronomy Reports, 37, 411

Verner D. A., Ferland G. J., Korista K. T., Yakovlev D. G., 1996, ApJ, 465, 487

Werner K., Nagel T., Rauch T., Hammer N. J., Dreizler S., 2006, A&A, 450, 725

White T. R., Lightman A. P., Zdziarski A. A., 1988, ApJ, 331, 939

Yungelson L. R., Nelemans G., van den Heuvel E. P. J., 2002, A&A, 388, 546

Zycki P. T., Krolik J. H., Zdziarski A. A., Kallman T. R., 1994, ApJ, 437, 597

# Chapter 3

# X-ray diagnostics of chemical composition of the accretion disk and donor star in UCXBs II: *XMM-Newton* observations

Koliopanos, Gilfanov, Bildsten & Trigo

## 3.1   Introduction

Low mass X-ray binaries (LMXBs) with orbital periods of less than one hour are known as ultra-compact X-ray binaries. Their short orbital periods imply orbits that are so tight that only an evolved compact donor could fit (e.g. Rappaport & Joss 1984; Nelson, Rappaport, & Joss 1986). Therefore, they must consist of a white dwarf or a helium star that has filled its Roche lobe and is accreting onto a neutron star (e.g. Tutukov & Yungelson, 1993; Iben, Tutukov, & Yungelson, 1995; Verbunt & van den Heuvel, 1995; Deloye & Bildsten, 2003; Deloye, Bildsten, & Nelemans, 2005).

X-ray radiation from LMXBs usually consists of a primary and a reflected component (e.g. Gilfanov, 2010, and references therein). Primary radiation is most likely created in a hot optically thin corona, the disk itself or – in the case of a neutron star accretor – in the boundary layer that forms on the surface of the star. The reflected component is produced when primary radiation is reprocessed by the optically thick Shakura - Sunyaev accretion disk and by the surface of the donor star facing the compact object. X-ray reflection spectra originating in normal LMXBs with main sequence or red giant donors are characterized by a bright iron K$\alpha$ emission line at $\approx$ $6.4-6.9$ keV with an equivalent width (EW) typically of the order of $\approx 100$ eV (e.g. Cackett et al., 2010).

The composition of the accreting material in UCXBs is expected to be significantly different from the solar composition accretion disks of typical LMXBs with main sequence or red giant donors. Due to the nature of their compact donor, their chemical composition is expected to be consistent with the ashes of H burning (mostly He and $^{14}$N), He burning (mostly C/O) or carbon burning (mostly O/Ne). Depending on initial parameters and the environment (e.g. being part of a globular cluster) of UCXB progenitors they will follow different evolutionary channels, resulting in a variety of donors ranging from non-degenerate He stars to C-O or O-Ne-Mg white dwarfs (e.g. Savonije, de Kool, & van den Heuvel, 1986; Podsiadlowski, Rappaport, & Pfahl, 2002; Yungelson, Nelemans, & van den Heuvel, 2002; Bildsten & Deloye, 2004). Due to the fact that the different UCXB formation channels lead to degenerate donors of similar mass, determining the chemical composition of the disk (and therefore the donor star) in UCXBs can provide valuable insights into the evolutionary path that created each system.

In principle, a straight forward determination of the chemical composition of the disk and donor star in these systems could be achieved using optical

spectroscopy. A He-rich object could be identified by the presence of strong He lines in its spectrum (e.g Nelemans, Jonker & Steeghs, 2006), while a C/O-rich object can be inferred by the lack of H and He lines combined with the presence of strong C and O lines (e.g. Nelemans et al., 2004; Werner et al., 2006). However, due to their small sized accretion disks (van Paradijs & McClintock, 1994) the optical counterparts of UCXBs are quite faint, with V-band absolute magnitudes that are usually larger than ≈5 with distances ranging from ≈3-12 kpc (e.g. Nelemans et al., 2004; Nelemans, Jonker & Steeghs, 2006). Therefore, ensuring definitive proof of the donor star composition – using optical spectroscopy – is a difficult task that can only be attempted using the latest generation of >8m telescopes.

In the case of X-ray spectroscopy the presence of O and Ne emission features – that appear in the spectra of reprocessed emission from the accretion disk and white dwarf surface – (e.g. Madej et al., 2010) and K-edges stemming from absorbing material in the vicinity of the disk (e.g. Schulz et al., 2010) could also provide direct indication of a C/O or O/Ne-rich disk and donor star. However, due to increased interstellar absorption below 1 keV and contamination of the reflected component by the primary emission, detection of these features with sufficient accuracy, often proves to be difficult. On the other hand, in (Koliopanos, Gilfanov & Bildsten, 2013, see 1st chapter), we demonstrated that the most striking and readily observable consequence of an anomalous C/O abundance involves the iron K$\alpha$ line located at 6.4 keV. In particular, for a source of moderate luminosity ($L_X \lesssim$ a few $10^{37} \mathrm{erg\,s^{-1}}$) we predicted a strong suppression of the Fe K$\alpha$ line in the case of a C/O or O/Ne/Mg WD donor. This translates to a more than an order of magnitude decrease of the EW of the line. On the other hand, in the case of a He-rich donor the iron line is expected to remain unaffected with its EW similar to that observed in LMXBs with main sequence or red giant donors. As was demonstrated in Koliopanos et al. these results are luminosity dependent. Namely, for luminosities exceeding $\mathrm{LogL_X} \approx 37.5$, we expect C, O and Ne to be fully ionized in the inner parts of the disk and thus canceling their screening effect on the iron line.

In addition to spectroscopic analysis, one could indirectly infer the accretion disk and donor star composition by studying a system's bursting activity. Gradual accumulation of H and/or He on the surface of an accreting neutron star can eventually result in the ignition of the accumulated shell, producing a thermonuclear flash that is known as a type I X-ray burst (e.g. Grindlay et al. 1976; Hansen & van Horn 1975 and for a detailed review Strohmayer &

Bildsten 2006). Half of the total population of known UCXBs have exhibited bursting activity, ranging from a few sporadic bursts to frequent bursting activity with a recurrence time extending from a few hours to a few weeks. Sporadic bursts could be due to trace amounts of H and He in an otherwise C/O-rich accreted material. Frequent bursting activity, on the other hand, would require copious amounts of H and/or He to refuel the bursts. Consequently, such an activity would support arguments in favor of a He-rich donor in a particular UCXB. This is illustrated by the detection of frequent burster (Galloway et al., 2008) 4U 1916-05 (discussed in this paper) which is also an optically confirmed He-rich source (Nelemans, Jonker & Steeghs, 2006). On other hand the same approach can yield conflicting results as is the case of 4U 0614+091 (also discussed in this work) whose bursting activity (Kuulkers et al., 2010; Linares et al., 2012) seems to be inconsistent with the strong evidence in favor of a C/O-rich donor (Nelemans et al., 2004; Werner et al., 2006).

In the present paper we investigate the chemical composition of the accretion disk in five UCXBs using X-ray spectroscopy. In particular we analyze *XMM-Newton* spectra of these sources and compare our results with the findings of Koliopanos et al. in order to put a constraint on the chemical composition of their accretion disks and donor star. We also analyze the spectra of two normal LMXBs, which we use as a control sample. In Section 3.2 we present the sample of UCXBs and LMXBs chosen for our analysis. We describe the details of data extraction, report on the specifics of each observation and present our data analysis where we look for the existence and strength of a potential iron K$\alpha$ line at $\approx 6.4\,\text{keV}$. The analysis is followed by discussion and conclusions in Sections 3.3 and 3.4.

## 3.2 Observations, data analysis and results

There are 14 confirmed UCXBs with measured orbital periods of less than one hour (e.g. see van Haaften, Voss & Nelemans, 2012, for a comprehensive list of candidate and confirmed UCXBs). The majority of these sources has been observed by multiple X-ray observatories. The present work focuses on *XMM-Newton* observations.

After analyzing all *XMM* observations of confirmed UCXBs, we have selected five sources for further analysis. The details of these observations are summarized in Table 3.1. The five sources were selected due to their

Table 3.1: List of *XMM-Newton* observations

| Object | obsID | Date | Duration[1] (s) | Net count rate[2] (c/s) |
|---|---|---|---|---|
| UCXBs | | | | |
| 4U 0513-40 | 0151750101 | 2003-04-01 | 16420 | $35.40 \pm 0.05$ |
| 4U 0614+091 | 0111040101 | 2001-03-13 | 13140 | $252.1 \pm 0.17$ |
| 2S 0918-549 | 0061140101 | 2001-05-05 | 38070 | $60.47 \pm 0.06$ |
| XTE J1807-294 | 0157960101 | 2003-03-22 | 9293 | $35.42 \pm 0.11$ |
| 4U 1916-05 | 0085290301 | 2002-09-25 | 14820 | $55.47 \pm 0.11$ |
| LMXBs | | | | |
| 4U 1705-44 | 0402300201 | 2006-08-26 | 34130 | $27.23 \pm 0.05$ |
| SAX J1808.4-3658 | 0560180601 | 2008-10-01 | 45050 | $300.3 \pm 0.09$ [3] |

[1]Duration of filtered pn observation.

[2]Full bandpass.

[3]Count rate after treatment for pile-up. Initial count rate was $689 \pm 0.1$

simple, power law dominated spectrum above 2.5 keV. Due to calibration uncertainties, as well as features inherent in the source emission, most of the sources in our sample display increasing spectral complexity below 2-2.5 keV. Since the focus of our investigation lies in the high energy part of the spectrum and a detailed description of the spectral continuum is beyond the scope of this paper, we have chosen to ignore all energy channels below 2.5 keV. This configuration allows for a more reliable detection of the Fe K$\alpha$ line. The only exception to this treatment is SAX J1808.4-3658 where a thermal component is strongly required by the fit, despite our channel selection. As a result – for SAX J1808.4-3658 – we decided to exclude only energy channels below 1 keV and include the additional spectral component in our model. The two LMXBs that constitute our control sample feature similar hard-state spectra. They have been chosen in order to verify our data analysis procedures in the full range of count rates, spanned by our UCXB sample.

Data reduction was performed using the *XMM-Newton* Data Analysis software SAS version 13.5.0. The present work focuses on the hard (above 1 keV) part of the spectrum and particularly the presence or absence of iron emission features at $\approx 6 - 7$ keV. The effective area of EPIC-pn at $\approx 7$ keV is approximately five times higher than that of MOS. Furthermore, during all observations analyzed below, at least one of the MOS detectors

was operated in imaging mode. Due to the brightness of our sources, most of the observations taken in this mode were suffering from severe pile-up. On the other hand – with the exception of 4U 0513-40 – pn was operating in timing mode during all observations analyzed in this work. In this mode, photon coordinates are resolved only in one dimension, along the column axis, allowing for high speed CCD read out. Apart from offering high time resolution, the timing mode is particularly suited for observing bright sources, since it allows for a higher non-piled up count rate. For these reasons our work is based exclusively on pn data.

Source photons for all pn observations, taken in timing mode, were extracted for RAWX from 25 to 50 and background for RAWX from 3 to 5, where RAWX is the coordinate along the column axis. For 4U 0513-40, where pn was operating in imaging mode, we extracted the source spectrum from a 27" circle centered at the source. Background was extracted according to latest EPIC calibration notes[1] from a source-free region at the same RAWY position as the source region. In all cases we extract photons with pixel pattern less than 5. All pn observations were checked for pile-up, using the SAS task `epatplot`. With the exception of SAX J1808.4-3658 no signatures of pile-up were found for any of the sources in our samples. Due to the high count rate of SAX J1808.4-3658 the pn data suffered from pile-up. To minimize pile-up effects we removed the three central columns from our extraction region. A subsequent `epatplot` test confirms that pile-up effects have been adequately treated. Lastly, event files for all sources observed in timing mode were treated with `epfast`. This SAS tool is a default setting in SAS 13.5 and corrects possible Charge Transfer Inefficiency (CTI) effects, due to high count rate.

Analysis is done using the XSPEC spectral fitting package, version 12.8.0 (Arnaud, 1996). Prior to analysis, all spectra were re-binned to ensure a minimum of 25 counts per energy channel. All spectra are fitted with a simple power law, with exception of SAX J1808.4-3658 where an additional thermal black body component was required. The iron line was modeled with a Gaussian and when not detected an upper limit on its EW was calculated at 90% confidence. Best-fit parameters for the spectral continuum of all objects along with their distances and luminosities calculated in the 2.5-10 keV range are summarized in Table 3.2. Best-fit parameters and EWs for Fe K$\alpha$ emission lines (or upper limits in the case of non detection) are

---

[1]http://xmm2.esac.esa.int/docs/documents/CAL-TN-0018.pdf

presented in Table 3.3.

### 3.2.1 4U 0513-40

4U 0513-40 is located at a distance of $\approx 12.2\,\mathrm{kpc}$ (Kuulkers et al., 2003) and has an observed orbital period of $17\,\mathrm{min}$ (Fiocchi et al., 2011). It has been observed by *BeppoSAX* , *Chandra*, *INTEGRAL*, *RXTE* and *XMM-Newton*. *XMM-Newton* observations have been analyzed by Juett & Chakrabarty (2005), where they report no significant emission or absorption features in the spectrum. No constraints on the donor composition – based on optical spectroscopy – have been reported.

At least nine thermonuclear X-ray bursts have been reported for 4U 0513-40. Two of them have been observed by Chandra and BeppoSAX (Homer et al., 2001; Fiocchi et al., 2011, respectively), and another 7 by RXTE (Galloway et al., 2008). The latter have been detected after analyzing more than ten years of RXTE observations.

*XMM-Newton* observed 4U 0513-40 on 2003 April 1 for 24 ks. All EPIC-cameras were working in imaging mode with MOS1 and MOS2 suffering from considerable pile-up. The net source count rate is $35.40 \pm 0.05\,\mathrm{c/s}$.

The spectrum of 4U 0513-40 above $2.5\,\mathrm{keV}$, was adequately described by an absorbed power law. No Fe K$\alpha$ emission line was detected in the spectrum. An upper limit for the EW of the iron line was calculated by including a Gaussian with a fixed width of $0.5\,\mathrm{keV}$, centered between 6.4-$6.9\,\mathrm{keV}$. The source has a moderate luminosity.

### 3.2.2 4U 0614+091

4U 0614+091 lies close to the galactic plane, at a distance of $\approx 3.2\,\mathrm{kpc}$ (Kuulkers et al., 2010) and has a measured optical period of $\approx 50\,\mathrm{min}$ (Shahbaz et al., 2008). It has been observed by *ASCA*, *BeppoSAX*, *Chandra*, *RXTE*, *Swift* and *XMM-Newton*. Numerous authors report the detection of a broad emission-like feature near $0.7\,\mathrm{keV}$ (e.g. Christian, White & Swank, 1994; Piraino et al., 1999; Madej et al., 2010; Schulz et al., 2010). Nevertheless, using data taken with the *Chandra Low-Energy Transmission Grating Spectrometer* (LETGS), Paerels et al. (2001) failed to detect the feature. They do, however report an unusually high Ne/O abundance ratio based on absorption edges. Furthermore, Juett, Psaltis & Chakrabarty (2001), analyzing archival *ASCA* data, argue that the broad line-like feature, reported by

Table 3.2: Best-fit parameters for spectral continuum. All uncertainties are $1\,\sigma$.

| Sources | Power Law | | $\chi_\nu^2$(d.o.f) | Luminosity $L_x$[1] | Distance |
|---|---|---|---|---|---|
| | $\Gamma$ | Norm $(10^{-2}\,\mathrm{ph\,keV^{-1}\,cm^{-2}\,s^{-1}})$ | | $(10^{36}\,\mathrm{erg\,s^{-1}})$ | (kpc) |
| **With faint or no Fe K$\alpha$ line** | | | | | |
| 4U 0513-40 | $2.04^{+0.02}_{-0.01}$ | $2.29^{+0.09}_{-0.04}$ | 1.05(1065) | 0.9 | 12.2[2] |
| 2S 0918-549 | $2.19 \pm 0.05$ | $5.93 \pm 0.05$ | 1.01(1470) | 0.4 | 4.8[3] |
| XTE J1807-294 | $2.07 \pm 0.02$ | $7.22 \pm 0.3$ | 1.00(1265) | 1.1 | 8.3 |
| **With bright Fe K$\alpha$ line** | | | | | |
| 4U 0614+091 | $2.28 \pm 0.01$ | $32.91^{+0.8}_{-0.7}$ | 1.01(1490) | 0.6 | 3.2[4] |
| 4U 1916-05 | $1.84 \pm 0.02$ | $6.22 \pm 0.20$ | 1.07(1413) | 1.6 | 8.9[5] |
| **Control sample** | | | | | |
| 4U 1705-44 | $1.91 \pm 0.01$ | $8.85 \pm 0.16$ | 1.05(1493) | 1.5 | 7.4[6] |
| SAX J1808.4-3658 | $2.19 \pm 0.01$ | $76.5 \pm 0.01$ | 1.30(1795) | 2.0 | 3.5[7] |

The models used are: phabs·powerlaw (4U 0513-40, 2S 0918-549, XTE J1807-294), phabs·(powerlaw+gaussian) (4U 0614+091, 4U 1705-44, 4U 1916-05), phabs·(powerlaw+gaussian)·gabs·gabs (4U 1916-05) and phabs·(blackbody+powerlaw+gaussian) (SAX J1808.4-3658). Here phabs is the XSPEC model for photoelectric absorption and gabs is the XSPEC model for a Gaussian absorption line. The paramaters of the black body component in SAX J1808.4-3658 are kT=0.23 ± 0.003 and norm=0.007±0.0002.
[1] Calculated in the 2.5-10 keV range. [2] Kuulkers et al. (2003) [3] Jonker & Nelemans (2004) [4] Kuulkers et al. (2010) [5] Galloway et al. (2008) [6] Galloway et al. (2008) [7] Cackett et al. (2009); Papitto et al. (2009)
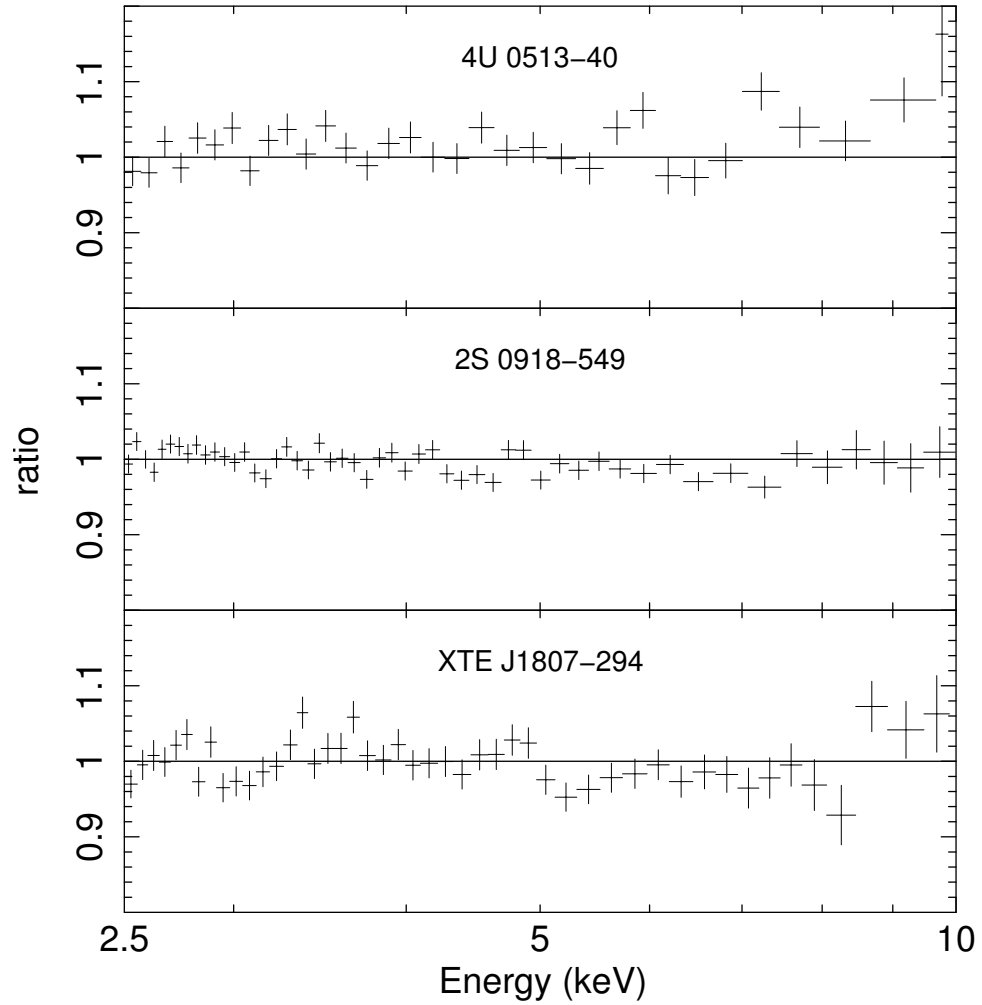
Figure 3.1: Ratio of the data to continuum model vs energy (keV) for three UCXB systems where no Fe line was detected. Best-fit parameters of the continuum models and upper limits on Fe line flux and EW are listed in Tables 3.2 and 3.3, respectively.

previous authors, can be explained by neon overabundance, attributed to neon-rich material local to the binary. Schulz et al. (2010) analyzing data taken with the *High-Energy Transmission Grating Spectrometer* (HETGS) on board *Chandra*, confirm the existence of excess optical depth near the Ne K edge. They also detect an extremely broadened OVIII Ly$\alpha$ emission feature, which they attribute to emission by highly ionized material in the inner parts of the disk. In order to account for the line broadening, the authors need to invoke the effects of gravitational broadening. Fitting a Laor profile (Laor, 1991) to the residuals reveals an inclination angle of the order of $\approx 88º$. However, there is no compelling evidence suggesting an edge-on inclination for 4U 0614+091 and there have been no dips observed in its light curve. To overcome this problem, Madej et al. (2010), suggest that a similar broad emission feature – this time detected in *XMM-Newton* RGS observations – is due to a gravitationally broadened OVIII emission line, that is the result of reflection of the source's primary spectrum off a C/O-rich disk. In this scenario, line broadening is partly due to effects of Compton scattering and their fit does not require such a high inclination angle. Madej et al. also report the absence of an iron emission line in their analysis of MOS2 data of the same observation. They propose that this could also be attributed to non solar composition of the accretion disk. Nevertheless Ng et al. (2010), analyzing pn data of the same *XMM-Newton* observation, report a broad emission feature at $\approx 6.8$ keV with an EW of the order of $\approx 160$ eV. In a more recent publication, Madej et al. (2014) reanalyze RGS observations of 4U 0614+091, this time using a modified version of the XIILVER reflection model (García & Kallman, 2010; García et al., 2013). XIILVER is adjusted to mimic a C/O-rich disk by increasing the abundances of carbon and oxygen relative to hydrogen by more than a hundredfold. This produces a disk reflection spectrum featuring a strong OVIII emission line which is then used to model RGS observations of 4U 0614+091. The authors conclude that the broad positive residuals at $\approx 0.7$ keV are due to a relativistically broadened OVIII emission line caused by reflection off a C/O-rich disk.

Absence of H or He lines, along with the presence of CI-IV and OI-III emission lines in optical spectra of 4U 0614+091, taken with *VLT*, suggest a C/O-rich accretion disk and donor star (Nelemans et al., 2004; Werner et al., 2006). In particular, Werner et al. use synthetic spectra, generated by a non-LTE accretion disk model, to place an upper limit of 10% on the abundance of H and/or He present in the accretion disk. These conclusions seem to be at odds with the fact that 4U 0614+091 is a source of multiple X-ray bursts, with

a measured recurrence time ranging from once every few weeks to once every $\approx 10$ days (Kuulkers et al., 2010; Linares et al., 2012). Namely, Kuulkers et al. – based on archival data collected from multi-instrument observations – calculate an average burst recurrence rate of about once every one to two weeks. Linares et al. use data collected with the Gamma-ray Burst Monitor (GBM) aboard the *Fermi Gamma-ray Space Telescope* to calculate a burst recurrence time of $\approx 12$ d, with the closest burst pair recorded within 2.8 d. Furthermore, by creating ignition models for type I X-ray bursts, following the work of Cumming & Bildsten (2001), Kuulkers et al. demonstrate that a H or He amount, substantially larger than the inferred upper limit of 10%, is required to simulate the characteristics of the observed bursts.

*XMM-Newton* observed 4U 0614+091 on 2001 March 13. There were two subsequent observations for $\approx 11$ ks and $\approx 17$ ks. The MOS1, MOS2 and pn detectors were only active during the second observation, therefore we focus on the second observation only. The net source count rate is $252.1 \pm 0.17$ c/s.

Modeling 4U 0614-091 with an absorbed power law leaves increased positive residuals in the 6-7 keV range (Fig. 3.2). We account for these by adding a Gaussian to our initial model. This reveals a bright and broad Fe K$\alpha$ emission line and improves our fit by a $\Delta\chi^2$ of 89, which corresponds to a more than $4\sigma$ significance for 3 d.o.f.. The line is centered at $\approx 6.64$ keV with an EW of $\approx 111$ eV and a width of $\approx 0.7$ keV.

### 3.2.3 2S 0918-549

2S 0918-549 has a measured orbital period of 17.4 min (Zhong & Wang, 2011) and lies at a distance of $\approx 4.8$ kpc (Jonker & Nelemans, 2004). It has been observed by *ASCA*, *BeppoSAX*, *Chandra*, *RXTE*, *XMM-Newton* and *VLT*. Juett, Psaltis & Chakrabarty (2001) analyzed archival *ASCA* observations of 2S 0918-549. They suggested an O/Ne chemical composition of the accreting material based on an unusual Ne/O number ratio compared to what is expected for the interstellar medium. This non-solar relative abundance of Ne was attributed to enrichment of the local ISM by the donor material. However further examination (Juett & Chakrabarty, 2003, 2005) revealed that the Ne/O ratio varies between different *Chandra*, *XMM-Newton* and *ASCA* observations of 2S 0918-549. This variability, combined with a tenfold decrease in flux between the *Chandra* and *XMM-Newton* observations and the earlier one by *ASCA*, led to the conclusion that the unusual Ne/O ratio maybe due to ionization effects and is not proof of the donor compo-

sition. In their analysis of 2S 0918-549, Juett & Chakrabarty (2003) do not comment on the existence or absence of the iron K$\alpha$ emission line. *VLT* data, analyzed by Nelemans et al. (2004) tentatively suggest a C/O-rich chemical composition of the accretion disk and donor star.

2S 0918-549 is also known to produce sporadic X-ray bursts. At least six type I X-ray bursts have been reported for this binary between 1996 and 2004. Two have been observed by Jonker et al. (2001) and Cornelisse et al. (2002) and another four by in't Zand et al. (2005). in't Zand et al. in contrast to what is suggested by optical data, suggest the possibility of a He-rich donor, based on the system's bursting activity.

*XMM-Newton* observed 2S 0918-549 on 2001 May 5 for 40 ks. MOS1 and pn cameras were operated in timing mode, while the MOS2 camera was operated in imaging mode. The net source count rate is $60.47 \pm 0.06$ c/s.

Similarly to 4U 0513-40, 2S 0918-549 has a moderate luminosity and is adequately modeled with an absorbed power law. No emission feature was required by the fit.

### 3.2.4   XTE J1807-294

XTE J1807-294 is a transient, accreting millisecond pulsar. Markwardt, Juda & Swank (2003), using *Chandra* observations, detected the source in the direction of the galactic bulge, suggesting a distance of $\approx 8.3$ kpc. X-ray pulsations observed using *RXTE* give an orbital period of $\approx 17$ min (Markwardt, Juda & Swank, 2003). *XMM-Newton* observations were analyzed by Campana et al. (2003). No emission or absorption features were detected, and an upper limit of 18-25 eV is placed on the EW of the iron line. Similarly, simultaneous *INTEGRAL*, *XMM-Newton* and *RXTE* observations by Falanga et al. (2005) revealed no evidence of emission or absorption features in the source continuum. *VLT* observations by D'Avanzo et al. (2009) failed to detected the source's optical counterpart. No type I X-ray bursts have been reported for this system.

*XMM-Newton* observed XTE J1807-294 on 2003 March 22 for $\approx 17$ ks during an outburst. MOS1 and MOS2 were operating on imaging mode and both suffered from pile-up. The net source count rate is $35.42 \pm 0.11$ c/s.

Again, the spectrum was modeled with an absorbed power law and no Fe K$\alpha$ emission line was detected. The data-to-model ratio vs energy plot for XTE J1807-294 is presented in Fig. 3.1 along with those of 4U 0513-40, 2S 0918-549 for which also no iron line was detected.

### 3.2.5   4U 1916-05

4U 1916-05 is a dipping source (its light curve exhibits periodic intensity dips), with an orbital period of 50 min (Walter et al., 1982) and a distance of $\approx 8.9$ kpc (Galloway et al., 2008). The characteristics of the source's dipping behavior indicate that it is viewed at a large inclination angle, with $i \geq 60°$ (Smale et al., 1988). *ASCA* observations of 4U 1916-05 were analyzed by Asai et al. (2000). They report a broad emission feature at 5.9 keV with an EW of $\approx 87$ eV. The presence of an emission feature in the unusual energy of 6.0 keV is also reported by Boirin et al. (2004) in their analysis of the *XMM-Newton* observation of 4U 1916-05. However this feature was not further investigated as it was not the focus of their paper. On the other hand, they report the detection of two narrow absorption lines at 6.65 and 6.95 keV that are consistent with resonant absorption from FeXXV and FeXXVI ions, respectively. This detection is repeated in *Chandra* observations analyzed by Juett & Chakrabarty (2006). The authors also report the existence of narrow absorption lines, due to the presence of H-like neon, magnesium, silicon, and sulfur. In addition to X-rays, optical observations by *VLT*, found prominent lines from HeI, HeII, NII and NIII, consistent with a He-rich accretion disk (Nelemans, Jonker & Steeghs, 2006).

4U 1916-05 is also a known X-ray burster. It exhibits short bursts that are consistent with moderate to high accretion rates, and have a recurrence time of $\approx 6.2$ hr (Galloway et al., 2008).

*XMM-Newton* observations of 4U 1916-05, analyzed in this work, were performed on September 25, 2002 for 17 ks. All EPIC cameras were operating in timing mode. The net source count rate is $55.47 \pm 0.11$ c/s.

Fitting the spectrum of 4U 1916-05 with an absorbed power law revealed a complex structure with both positive and negative residuals between $\approx 6 - 7$ keV (Fig. 3.2). As has been suggested before (e.g. Boirin et al., 2004), the negative residuals could be interpreted as absorption lines at $\approx 6.65$ and $\approx 6.95$ keV, due to resonant absorption by FeXXV and FeXXVI ions. To account for these features, we add two narrow Gaussian absorption lines to our model. The first one – corresponding to absorption due to He-like iron – is centered at $\approx 6.66$ keV and improves our fit by a $\Delta\chi^2$ of 40 for 3 d.o.f.. The second – corresponding to absorption due to H-like iron – is centered at $\approx 6.92$ keV and reduces the $\chi^2$ value by 20 for 3 d.o.f.. The two absorption lines are strongly required by the fit and are of high (more than $3\sigma$) significance. They can be attributed to highly ionized plasma in the

vicinity of the accretion disk.

The remaining positive residuals suggest a complex broad emission feature in the 5-7 keV range. Fitting this feature with a Gaussian reveals a broad emission "line" at the unexpected energy of $\approx 5.46$ keV with a width of $\approx 1.64$ keV. The EW of this feature is $\approx 595$ eV. Adding the Gaussian line to our model, improves our fit massively, by a $\Delta\chi^2$ of 187 for 3 d.o.f.. However, the unusual values of the line parameters and the fact that this is a dipping source, could indicate that this feature is an artifact resulting from our extraction of a single spectrum for the entire observation, during both dipping and persistent phases. To investigate this possibility, we extracted two additional spectral sets. One taken from events that were recorded only during the persistent phase and a second one during the dipping phase. The results are qualitatively identical to the ones obtained for the full observation. All three spectra (dipping, persistent and combined) show strong evidence of a broad emission feature located at $\approx 5.5 - 6$ keV. Obviously this feature is too complex to be fitted with a simple Gaussian. Hence the parameters obtained have no physical meaning. Nevertheless, in the framework of our model, the statistical significance of a strong iron emission line in the 6-7 keV range is beyond doubt. Further examination of the detailed spectral shape of the emission line is beyond the scope of this paper. If we fix the line energy at 6.4 keV and the line width at 0.5 keV we obtain an emission line with an EW of $\approx 95$ eV with more than $4\sigma$ significance.

### 3.2.6  Control Sample

**4U 1705-44**

4U 1705-44 is a typical LMXB containing a neutron star accretor with a weak magnetic field. Its distance is measured at $\approx 7.4$ kpc (Galloway et al., 2008). The source exhibits frequent type I X-ray bursts (e.g. Gottwald et al., 1989) and has been observed during hard and soft states. In both states its spectrum features a bright broad iron K$\alpha$ emission line (e.g Di Salvo et al., 2005, 2009; Cackett et al., 2010; Egron et al., 2013). Multiple observations of 4U 1705-44 have been performed by all major X-ray telescopes. 4U 1705-44 is a frequent burster with a recurrence time of $\approx 0.91$ hr (Galloway et al., 2008).

In the present work we reanalyze *XMM-Newton* observations performed on September 26, 2006 during a hard state. Only pn and RGS were active
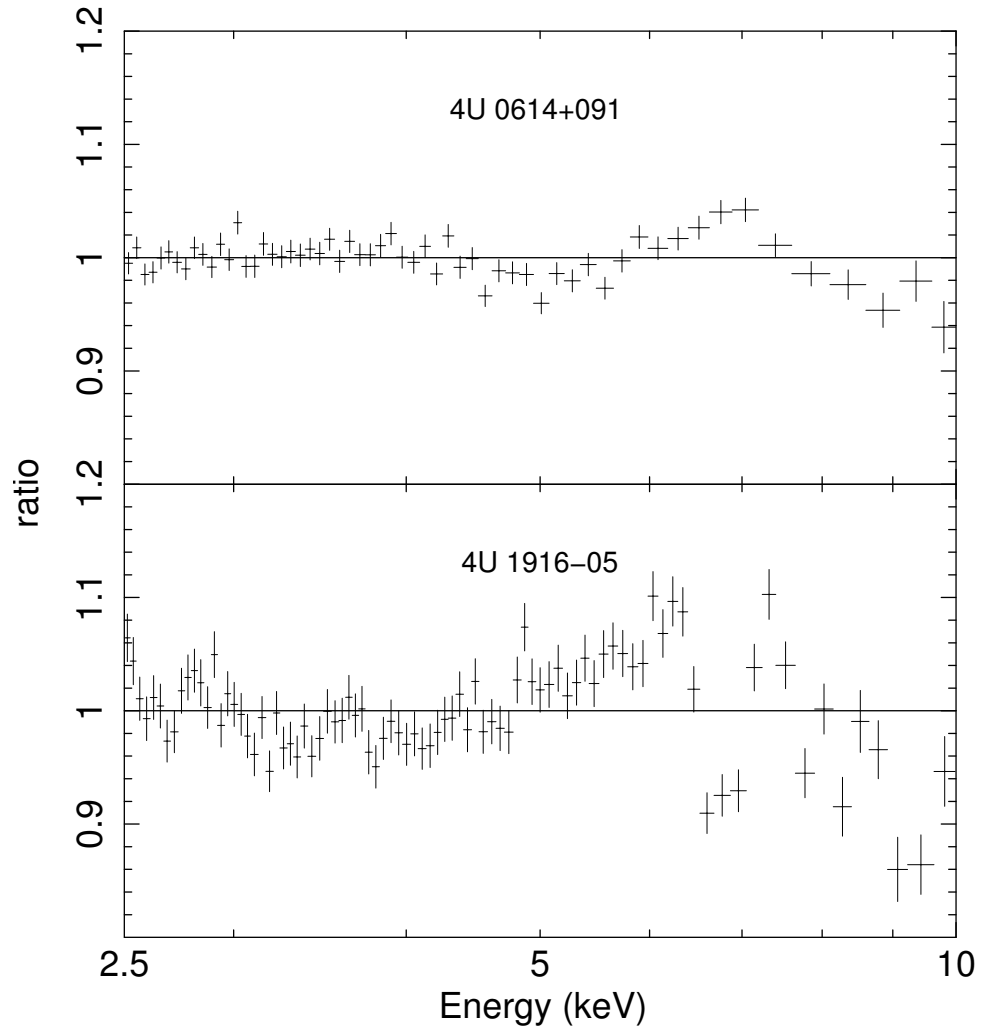
Figure 3.2: Ratio of the data to continuum model vs energy for 4U 1916-05 and 4U 0614-091 whose spectra feature a bright iron line. Best-fit parameters of the continuum models are listed in Table 3.2. Fe line flux and EW for Gaussian are listed in Table 3.3.

during the observation with pn operating in timing mode. The net source count rate is $27.23 \pm 0.05 \, \mathrm{c/s}$.

As expected for the LMXBs in our control sample, we detect strong positive residuals in the 6-7 keV range (Fig. 3.3), characteristic of a strong iron line. Fitting the emission feature with a Gaussian yields an emission line with an EW of $\approx 52 \, \mathrm{eV}$ (for details see Table 3.3).

### SAX J1808.4-3658

SAX J1808.4-3658 is a transient LMXB with an orbital period of $\approx 2.01 \, \mathrm{hrs}$ (Chakrabarty & Morgan, 1998). Its distance is measured at $\approx 3.5 \, \mathrm{kpc}$ (Cackett et al., 2009; Papitto et al., 2009). It was the first millisecond pulsar discovered (Wijnands & van der Klis, 1998). The source's quiescent periods are interrupted by short outbursts approximately every 2.5 years. SAX J1808.4-3658 has been observed by *ASCA*, *BeppoSAX*, *Chandra*, *INTEGRAL*, *Swift*, *RXTE* and *XMM-Newton* during both quiescent and bursting periods. *VLT* observations have also been performed during its 2008 September-October outburst. Analysis of source spectra during outbursts, have revealed the existence of a Fe K$\alpha$ emission line (e.g Gilfanov et al., 1998; Cackett et al., 2009; Papitto et al., 2009). Lastly, the source is a burster with a recurrence time of $\approx 21 \, \mathrm{hr}$ (Galloway et al., 2008).

We reanalyze the 63 ks *XMM-Newton* observation of October 1st 2008 during outburst. The MOS1 camera operated in imaging mode while MOS2 and pn in timing mode. The net source count rate is $300.3 \pm 0.09 \, \mathrm{c/s}$.

SAX J1808.4-3658 is fitted using a black body and a power law spectrum. Examination of the data-to-model ratio of our fit, reveals a strong emission feature at the 6-7 keV range (Fig. 3.3). Fitting this feature with a Gaussian reveals a broad emission line centered at $\approx 6.61 \, \mathrm{keV}$ with a width of $\approx 1.13 \, \mathrm{keV}$ and an EW of $\approx 246 \, \mathrm{eV}$. The emission feature is characteristic of the iron K$\alpha$ emission line expected in X-ray reflection spectra originating in typical LMXBs with main sequence or red giant donors. The broadness of the line obviously justifies further inquiry on different possible mechanisms that would explain it. However, such a task has already been accomplished by Papitto et al. (2009) and is not the focus of the present work.
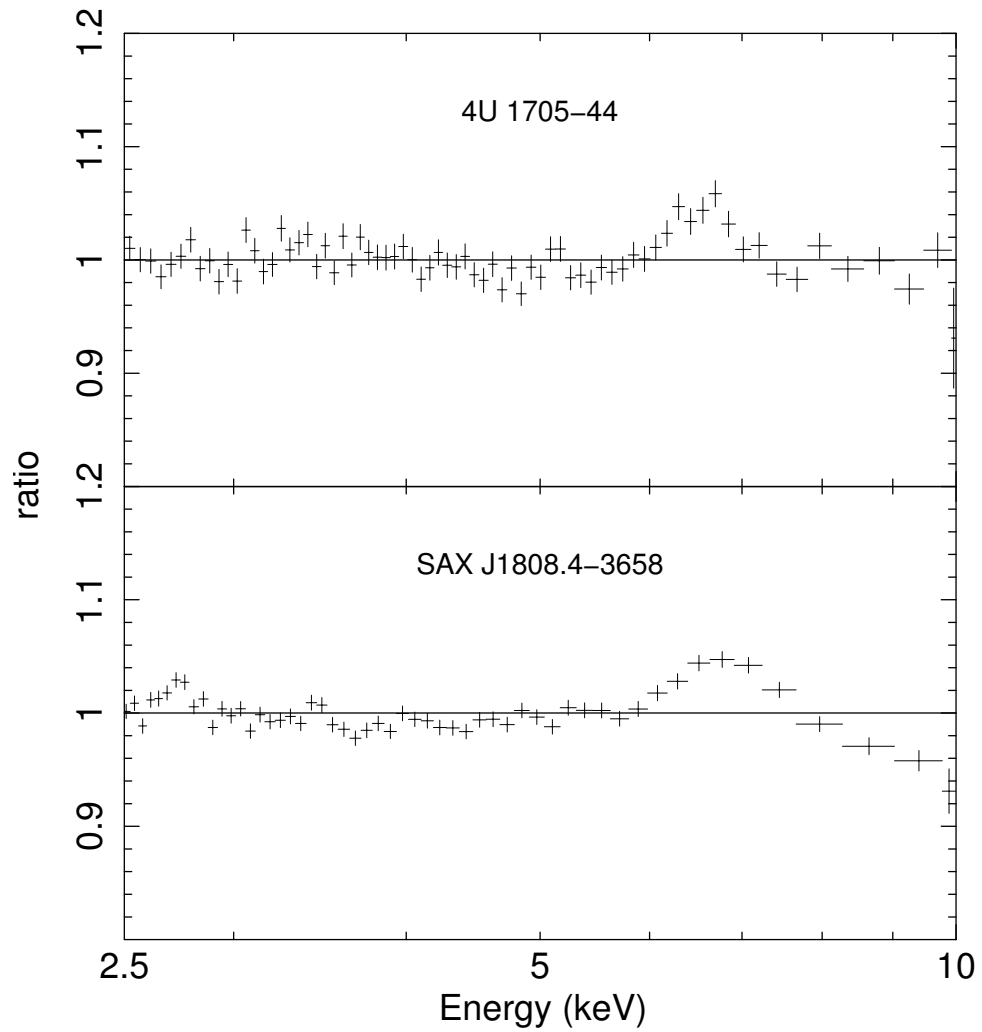
Figure 3.3: Ratio of the data to continuum model vs energy for the two LMXBs in our control sample. Best-fit parameters of the continuum models are listed in Table 3.2. Fe line flux and EWs are listed in Table 3.3.

Table 3.3: Best-fit parameters of iron K$\alpha$ emission line. In case of no detection an upper limit at 90% confidence level is given. All errors are 1$\sigma$.

| Sources | Norm $(10^{-5}\,\mathrm{ph\,cm^{-2}\,s^{-1}})$ | Gaussian LineE (keV) | $\sigma$ (keV) | EW (eV) | Bursts Rec. Time[1] |
|---|---|---|---|---|---|
| **With faint or no Fe K$\alpha$ line** | | | | | |
| 4U 0513-40 | $< 0.92$ | 6.4-6.9 | $0.5^2$ | $< 20$ | 9 bursts |
| 2S 0918-549 | $< 0.63$ | 6.4-6.9 | $0.5^2$ | $< 7$ | 6 bursts |
| XTE J1807-294 | $< 1.25$ | 6.4-6.9 | $0.5^2$ | $< 10$ | 0 bursts |
| **With Fe K$\alpha$ line** | | | | | |
| 4U 0614+091 | $32.9^{+7.9}_{-7.4}$ | $6.64 \pm 0.08$ | $0.67^{+0.10}_{-0.08}$ | $111.1^{+20}_{-17}$ | $\approx 10\,\mathrm{d}$ |
| 4U 1916-05 | $27.7 \pm 2.47$ | $6.4^2$ | $0.5^2$ | $95 \pm 12$ | $\approx 6.2\,\mathrm{hr}$ |
| **Control sample** | | | | | |
| 4U 1705-44 | $13.2^{+1.95}_{-1.82}$ | $6.53 \pm 0.05$ | $0.34 \pm 0.05$ | $51.7^{+13}_{-12}$ | $\approx 0.91\,\mathrm{hr}$ |
| SAX J1808.4-3658 | $173 \pm 27$ | $6.40 \pm 0.07$ | $0.83^{+0.10}_{-0.11}$ | $131 \pm 20$ | $\approx 21\,\mathrm{hr}$ |

[1] Recurrence time when available. Otherwise total number of recorded bursts. All references regarding bursting activity are given in Section 2.2.

[2] The parameter was fixed.

## 3.3    Discusssion

We have analyzed the spectra of 5 confirmed UCXBs with H-poor donors and low to moderate luminosities. Specifically, we investigated the existence of a Fe K$\alpha$ line in their spectra. Three objects in our sample – namely 2S 0918-549, XTE J1807-294, 4U 0513-40 – display no obvious emission features in the energy range between 6 and 7 keV. This result is in agreement with the works of previous authors (e.g. Campana et al., 2003; Juett & Chakrabarty, 2005). On the other hand, systems 4U 0614+091 and 4U 1916-05 display a bright iron K$\alpha$ line. This emission feature is broad and more complex than a simple Guassian would describe, but there is no doubt that strong iron emission is evident in both sources. The spectra of 4U 0614+091 and 4U 1916-05 are similar (e.g. see the ratio plots in figures 3.2 and 3.3) to the spectra of typical LMXBs like 4U 1705-44 and SAX J1808.4-3658, also analyzed in this work.

### 3.3.1    X-ray diagnostics

In Koliopanos et al. (2013, see previous chapter) we showed that non-solar composition of the accretion disks in UCXBs can have a powerful effect on fluorescent emission lines appearing in their spectra. Namely, the bright iron K$\alpha$ line, typically found in spectra of LMXBs with main sequence or red giant donors, is expected to be severely suppressed in the case of UCXBs with C/O or O/Ne/Mg WD donors. This is due to screening by oxygen in the C/O or O/Ne dominated material. On the other hand, due to the lower ionization threshold of He, the iron line in spectra of UCXBs with He star or He WD donors, is expected to retain its nominal strength, mostly determined by iron abundance. Ionization of the disk material at high mass accretion rates may lead to luminosity dependence of this behavior. Specifically, line suppression due to screening by oxygen, is expected to take effect in objects with moderate luminosities ($L_X \lesssim$ a few $10^{37} \mathrm{erg\,s^{-1}}$).

**Sources with no Fe K$\alpha$ emission line**

Using results of our Monte Carlo simulation from Koliopanos et al. (2013, see previous chapter) we can place constraints on the O/Fe ratio of the accretion disk in the three sources for which an iron line was not detected. The code simulates reflection off a homogeneous slab of infinite optical depth that is
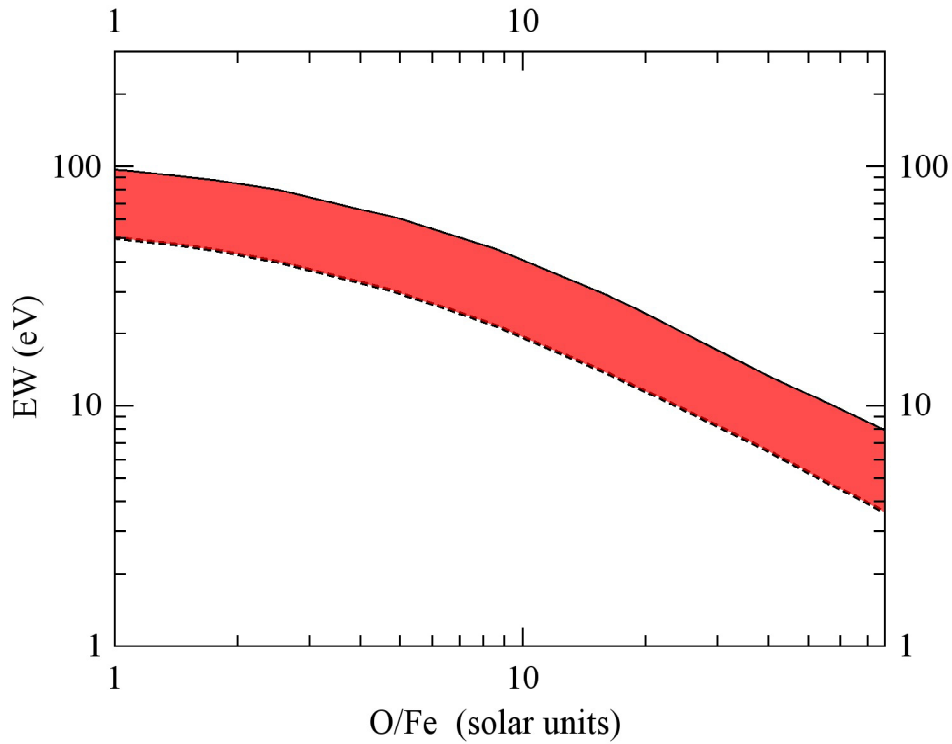
Figure 3.4: Dependence of Fe K$\alpha$ line EW (eV) on O/Fe ratio, given in units of its solar value. The curves were calculated for an incident spectrum with power law spectral shape with an index of 2.2. The solid curve is calculated for a face-on configuration (0º inclination) and the dotted line for an $\approx$edge-on configuration (80º inclination).

comprised of cold and neutral material . For this example, the primary, incident radiation has a power law shaped spectrum with a spectral index of 2.2 and is emitted isotropically from a point source above the disk surface. In order to study the whole range of possible configurations, from face-on to ≈edge-on view, we run two sets of calculations, where the reflection spectrum is registered at two distinct viewing angles of 0º and 80º respectively. Since there are no dips in the light curves of the three systems, we do not investigate a viewing angle larger than 80º. The code simulates fluorescence K$\alpha$ and K$\beta$ lines for elements from Z=3 to 30 and reports their EWs with respect to the total emission, which is a mixture of both the primary and reflected emission (for details see Section 2.4 ).

We generate a grid of EW values of the Fe K$\alpha$ fluorescence line at 6.4 keV, calculated for a sequence of increasing C/O abundance, starting with solar-like material. Abundances of H and He are reduced along the sequence, thus conserving the total number of nucleons. Similarly to Koliopanos et al. mass fractions of all other elements remain fixed at their solar values, as well as the abundance ratio of carbon and oxygen. The position along this sequence is given in terms of O/Fe ratio, in units of its solar value. Obviously, as H and He are "converted" to C and O, O/Fe ratio will increase. The maximum value of the O/Fe ratio that corresponds to a C/O-rich disk – in which all hydrogen and helium has been replaced by carbon and oxygen – is ≈ 77 times its solar value. Solar abundances for elements with Z=1-30 were adopted from Feldman (1992), elements not listed in this tabulation were taken from Grevesse & Sauval (1998). The resulting dependencies of EW on the O/Fe ratio are presented in Fig. 3.4.

As is evident from the plot, even in the marginal case of a system viewed ≈edge-on, an EW value of 20 eV – the highest upper limit measured for the three sources – corresponds to an O/Fe ratio that is more than ≈10 times higher than the solar value. The EW upper limits of 7 and 10 eV – for 2S 0918-549 and XTE J1807-294 – correspond to O/Fe ratios exceeding ≈37 and ≈20 times the solar value, respectively. Since there are no indications (e.g. a dipping light curve) of a large inclination angle for these three sources, the real lower limits are probably higher. These results place a strong constraint on the chemical composition of these systems. Namely, we conclude that the lack of an iron emission line in the spectra of 2S 0918-549, XTE J1807-294 and 4U 0513-40 is the result of a C/O or O/Ne/Mg-rich accretion disk and donor star in these systems.

A final point of interest regarding Fig. 3.4 is the fact that in this exam-

ple, our calculations predict a maximum Fe K$\alpha$ EW value of $\approx$100 eV. This value is in agreement with the values obtained by the fits of 4U 0614+091 and 4U 1705-44 but it is relatively smaller than the value obtained for SAX J1808.4-3658 and significantly smaller than the one obtained for 4U 1916-05. This apparent discrepancy is mostly due to the fact that a simple Gaussian profile was used to fit broad emission features that have a more complicated shape than a Gaussian can describe. This is particularly evident in 4U 1916+091 which is a confirmed edge-on viewed system with a dipping light curve. Implementation of more sophisticated models such a Laor profile or XSPEC model `diskline` (Fabian et al., 1989) yields smaller, more realistic EW values in the $\approx$ 100 eV range. Additionally, alternative modeling of the underlying spectral continuum – especially when the full energy range is considered – can result in different values for the EW of the line. For instance a different choice of the spectral continuum of SAX J1808.4-3658 in Ng et al. (2010) resulted in an EW of $\approx$30 eV for the iron line. A value much smaller than the one derived in this work ($\approx$ 130 eV) and in that of Papitto et al. (2009) ($\approx$ 120 eV). However, a detailed investigation of the emission line profiles and the shape of the spectral continuum was beyond the scope of this work, where we are only interested in the fact of the existence of the line. Therefore, energies below 2.5 kev were ignored and an absorbed power law and a simple Gaussian model were used to model the spectral continuum and the emission lines.

**Sources with Fe K$\alpha$ emission line**

The presence of a strong Fe K$\alpha$ line in the spectra of two remaining sources in our sample, 4U 1916-05 and 4U 0614+091 is an indication of a He-rich accretion disk and donor star in these systems. Namely, according to our model, the presence of a strong iron line, in the spectrum of a moderately luminous object, requires an O/Fe ratio that is close to the solar value. In the context of UCXBs, this would point towards a He-rich donor.

## 3.3.2 Optical spectra and X-ray bursts

Out of the three systems for which no emission line was detected, only 2S 0918-549 has been studied by means of optical spectroscopy. The analysis of Nelemans et al. (2004) tentatively suggests a C/O-rich rich donor. This is in agreement with our own conclusions. On the other hand, systems 2S

0918-549 and 4U 0513-40 have exhibited sporadic bursting activity during the previous decades (see Table 3.3 and relevant subsections). The characteristics of some of the bursts are compatible with helium burning, a fact that led in't Zand et al. (2005) to suggest the possibility of a He-rich donor in 2S 0918-549. Nevertheless, over the span of $\approx$ 10years, just a handful of bursts has been reported for these two systems (e.g. in't Zand et al., 2005; Galloway et al., 2008) and therefore they cannot provide definitive proof of donor composition. It is certainly plausible that small amounts of H and/or He in an otherwise C/O-rich disk could fuel sporadic bursts.

The strong Fe K$\alpha$ line in the spectrum of 4U 1916-05, which is an UCXB system with an optically confirmed He-rich donor (Nelemans, Jonker & Steeghs, 2006) is also in complete agreement with the theoretical predictions presented in Koliopanos et al.. Furthermore, the system's frequent bursting activity reinforces the arguments in favor of a He-rich donor. Perhaps more interestingly, however, our argument in favor of a He-rich donor star in 4U 0614+091 is at odds with the fact that the system has been classified as C/O rich, based on optical spectroscopy (Nelemans et al., 2004; Werner et al., 2006). On the other hand, our estimation readily explains the source's repeated bursting activity as reported by Kuulkers et al. (2010) and Linares et al. (2012) and is in complete agreement with the conclusions reached by these authors.

Nevertheless, the lack of He lines in the optical spectrum of 4U 0614+091 (Nelemans et al., 2004; Werner et al., 2006) and particularly the upper limit of 10% He abundance in the disk material, placed by Werner et al. are strong arguments in favor of a C/O rich donor. This upper limit is calculated for a disk $T_{eff}$ of 28000 K at a distance of 2000 stellar radii. For this temperature the dominant ionization stage of helium at $\tau = 1$ is HeII (Werner et al., 2006, Figure 6). Therefore, according to the Werner et al. model, an accretion disk with a helium abundance of more than 10%, would produce stronger He emission lines than the observed upper limits. However, their model ignores disk illumination and authors acknowledge that introducing disk irradiation from the NS surface and the comptonizing corona would affect the ionization structure of the disk. Namely, if $T_{eff}$ is high enough, helium could be fully ionized even in the outer parts of the disk. Such a scenario would promptly reconcile the lack of He-lines in the optical spectrum, the system's bursting activity and the presence of a strong iron line in the reflection spectrum.

## 3.4 Summary and conclusions

We searched for the iron K$\alpha$ in the spectra of five UCXBs with H-deficient donors. Based on the non-detection of a Fe line and the predictions of Koliopanos, Gilfanov & Bildsten (2013), we have concluded that the accretion disk material of three of the objects in our sample (2S 0918-549, XTE J1807-294 and 4U 0513-40) has an O/Fe ratio that is at least $\approx 10$ times higher than the solar value. In the context of UCXBs this suggests a C/O or O/Ne/Mg-rich donor. Furthermore, the presence of a strong Fe K$\alpha$ line in the spectra of the remaining two systems (4U 0614+091 and 4U 1916-05) indicates a He-rich donor. In the case of 2S 0918-549 and 4U 1916-05 our findings are also supported by results obtained through optical spectroscopy. On the other hand, our suggestion of a He-rich donor in 4U 0614+091 contradicts arguments in favor of a C/O-rich donor, but is consistent with the source's regular bursting activity.

# Bibliography

Arnaud K. A., 1996, in Astronomical Society of the Pacific Conference Series, Vol. 101, Astronomical Data Analysis Software and Systems V, Jacoby G. H., Barnes J., eds., p. 17

Asai K., Dotani T., Nagase F., Mitsuda K., 2000, ApJS, 131, 571

Bildsten L., Deloye C. J., 2004, ApJ, 607, L119

Boirin L., Parmar A. N., Barret D., Paltani S., Grindlay J. E., 2004, A&A, 418, 1061

Cackett E. M., Altamirano D., Patruno A., Miller J. M., Reynolds M., Linares M., Wijnands R., 2009, ApJ, 694, L21

Cackett E. M. et al., 2010, ApJ, 720, 205

Campana S., Ravasio M., Israel G. L., Mangano V., Belloni T., 2003, ApJ, 594, L39

Chakrabarty D., Morgan E. H., 1998, Nature, 394, 346

Christian D. J., White N. E., Swank J. H., 1994, ApJ, 422, 791

Cornelisse R. et al., 2002, A&A, 392, 885

Cumming A., Bildsten L., 2001, ApJ, 559, L127

D'Avanzo P., Campana S., Casares J., Covino S., Israel G. L., Stella L., 2009, A&A, 508, 297

Deloye C. J., Bildsten L., 2003, ApJ, 598, 1217

Deloye C. J., Bildsten L., Nelemans G., 2005, ApJ, 624, 934

Di Salvo T. et al., 2009, MNRAS, 398, 2022

Di Salvo T., Iaria R., Méndez M., Burderi L., Lavagetto G., Robba N. R., Stella L., van der Klis M., 2005, ApJ, 623, L121

Egron E. et al., 2013, A&A, 550, A5

Fabian A. C., Rees M. J., Stella L., White N. E., 1989, MNRAS, 238, 729

Falanga M. et al., 2005, A&A, 436, 647

Feldman U., 1992, Phys. Scr, 46, 202

Fiocchi M., Bazzano A., Natalucci L., Landi R., Ubertini P., 2011, MNRAS, 414, L41

Galloway D. K., Muno M. P., Hartman J. M., Psaltis D., Chakrabarty D., 2008, ApJS, 179, 360

García J., Dauser T., Reynolds C. S., Kallman T. R., McClintock J. E., Wilms J., Eikmann W., 2013, ApJ, 768, 146

García J., Kallman T. R., 2010, ApJ, 718, 695

Gilfanov M., 2010, in Lecture Notes in Physics, Berlin Springer Verlag, Vol. 794, Lecture Notes in Physics, Berlin Springer Verlag, Belloni T., ed., p. 17

Gilfanov M., Revnivtsev M., Sunyaev R., Churazov E., 1998, A&A, 338, L83

Gottwald M., Haberl F., Langmeier A., Hasinger G., Lewin W. H. G., van Paradijs J., 1989, ApJ, 339, 1044

Grevesse N., Sauval A. J., 1998, Space Sci. Rev., 85, 161

Grindlay J., Gursky H., Schnopper H., Parsignault D. R., Heise J., Brinkman A. C., Schrijver J., 1976, ApJ, 205, L127

Hansen C. J., van Horn H. M., 1975, ApJ, 195, 735

Homer L., Anderson S. F., Margon B., Deutsch E. W., Downes R. A., 2001, ApJ, 550, L155

Iben, Jr. I., Tutukov A. V., Yungelson L. R., 1995, ApJS, 100, 233

in't Zand J. J. M., Cumming A., van der Sluys M. V., Verbunt F., Pols O. R., 2005, A&A, 441, 675

Jonker P. G., Nelemans G., 2004, MNRAS, 354, 355

Jonker P. G. et al., 2001, ApJ, 553, 335

Juett A. M., Chakrabarty D., 2003, ApJ, 599, 498

Juett A. M., Chakrabarty D., 2005, ApJ, 627, 926

Juett A. M., Chakrabarty D., 2006, ApJ, 646, 493

Juett A. M., Psaltis D., Chakrabarty D., 2001, ApJ, 560, L59

Koliopanos F., Gilfanov M., Bildsten L., 2013, MNRAS, 432, 1264

Kuulkers E., den Hartog P. R., in't Zand J. J. M., Verbunt F. W. M., Harris W. E., Cocchi M., 2003, A&A, 399, 663

Kuulkers E. et al., 2010, A&A, 514, A65

Laor A., 1991, ApJ, 376, 90

Linares M. et al., 2012, ApJ, 760, 133

Madej O. K., Garcia J., Jonker P. G., Parker M. L., Ross R., Fabian A. C., Chenevez J., 2014, ArXiv e-prints

Madej O. K., Jonker P. G., Fabian A. C., Pinto C., Verbunt F., de Plaa J., 2010, MNRAS, 407, L11

Markwardt C. B., Juda M., Swank J. H., 2003, The Astronomer's Telegram, 127, 1

Nelemans G., Jonker P. G., Marsh T. R., van der Klis M., 2004, MNRAS, 348, L7

Nelemans G., Jonker P. G., Steeghs D., 2006, MNRAS, 370, 255

Nelson L. A., Rappaport S. A., Joss P. C., 1986, ApJ, 311, 226

Ng C., Díaz Trigo M., Cadolle Bel M., Migliari S., 2010, A&A, 522, A96

Paerels F. et al., 2001, ApJ, 546, 338

Papitto A., Di Salvo T., D'Aì A., Iaria R., Burderi L., Riggio A., Menna M. T., Robba N. R., 2009, A&A, 493, L39

Paul B., Jaaffery S. N. A., Naik S., Agrawal P. C., 2004, ApJ, 602, 913

Piraino S., Santangelo A., Ford E. C., Kaaret P., 1999, A&A, 349, L77

Podsiadlowski P., Rappaport S., Pfahl E. D., 2002, ApJ, 565, 1107

Rappaport S., Joss P. C., 1984, ApJ, 283, 232

Savonije G. J., de Kool M., van den Heuvel E. P. J., 1986, A&A, 155, 51

Schulz N. S., Nowak M. A., Chakrabarty D., Canizares C. R., 2010, ApJ, 725, 2417

Shahbaz T., Watson C. A., Zurita C., Villaver E., Hernandez-Peralta H., 2008, PASP, 120, 848

Smale A. P., Mason K. O., White N. E., Gottwald M., 1988, MNRAS, 232, 647

Strohmayer T., Bildsten L., 2006, New views of thermonuclear bursts, Lewin W. H. G., van der Klis M., eds., pp. 113–156

Tutukov A. V., Yungelson L. R., 1993, Astronomy Reports, 37, 411

van Haaften L. M., Voss R., Nelemans G., 2012, A&A, 543, A121

van Paradijs J., McClintock J. E., 1994, A&A, 290, 133

Verbunt F., van den Heuvel E. P. J., 1995, X-ray Binaries, 457

Walter F. M., Mason K. O., Clarke J. T., Halpern J., Grindlay J. E., Bowyer S., Henry J. P., 1982, ApJ, 253, L67

Werner K., Nagel T., Rauch T., Hammer N. J., Dreizler S., 2006, A&A, 450, 725

Wijnands R., van der Klis M., 1998, Nature, 394, 344

Yungelson L. R., Nelemans G., van den Heuvel E. P. J., 2002, A&A, 388, 546

Zhong J., Wang Z., 2011, ApJ, 729, 8

# Chapter 4

# Luminosity dependent change of the emission diagram in X-ray pulsar 4U 1626-67

## 4.1 Introduction

4U 1626-67 is an accreting X-ray pulsar located at a distance of $\sim 5 - 13\,\mathrm{kpc}$ from the Sun (Chakrabarty, 1998). It has a pulsation period of $\approx 7.7\,\mathrm{s}$ and an orbital period of $\approx 42$ min, (Middleditch et al., 1981; Chakrabarty, 1998). Its short orbital period classifies it as an ultra compact X-ray binary (UCXB), a subgroup of low mass X-ray binaries (LMXBs) with orbital periods of less than one hour. The short orbital periods of UCXBs suggest such tight orbits that only an evolved compact donor can fit. UCXBs, most likely, consist of a white dwarf or a helium star that is accreting onto a neutron star due to Roche lobe overflow (e.g. Tutukov & Yungelson, 1993; Iben, Tutukov, & Yungelson, 1995; Verbunt & van den Heuvel, 1995; Deloye & Bildsten, 2003; Deloye, Bildsten, & Nelemans, 2005). Due to their evolved nature, UCXB donors are expected to be hydrogen deficient. Depending on the initial conditions and the environment in which they are created (e.g. being part of a globular cluster) their donors can follow different evolutionary paths, leading to a variety of objects, ranging from non-degenerate He stars to C/O or O/Ne/Mg white dwarfs (e.g. Savonije, de Kool, & van den Heuvel, 1986; Podsiadlowski, Rappaport, & Pfahl, 2002; Yungelson, Nelemans, & van den Heuvel, 2002; Bildsten & Deloye, 2004).

Since its discovery (Giacconi et al., 1972; Rappaport et al., 1977), 4U 1626-67 has been observed by all major X-ray observatories. Furthermore, UV and optical spectra have been obtained by the *Hubble Space Telescope* and the *Very Large Telescope*, respectively. Analysis of BeppoSAX observations by Orlandini et al. (1998) revealed the presence of cyclotron absorption lines, suggesting strong magnetic field of $\approx 3 \times 10^{12}\,\mathrm{G}$, making the source the only strongly magnetised neutron star in an ultracompact binary known so far. Another intriguing feature of its X-ray spectrum is the presence of prominent Ne and O emission lines. First detected in ASCA data, analyzed by Angelini et al. (1995), they have been studied extensively using high resolution spectroscopy (Schulz et al., 2001; Krauss et al., 2007). The lines are believed to originate in C/O or O/Ne dominated hot plasma in the vicinity of the compact object, and suggest a donor whose chemical composition is enriched by products of later stages of nuclear burning, most likely, a C-O-Ne or O-Ne-Mg white dwarf. These findings are further corroborated by the HST UV spectrum that revealed both emission and absorption features from C, O, and Si but lacked He emission lines (Homer et al., 2002) and by the VLT optical spectrum that featured prominent C and O emission lines, but

showed no evidence of H or He (Werner et al., 2006).

The timing properties and the shape of the pulse profile of 4U 1626-67 have also been studied extensively since its discovery in 1977. Since then, 4U 1626-67 has transitioned through steady episodes of both spin-down and spin-up phases and and is currently in a spin-up period. During its first spin-up period between 1977 and 1990 the source's luminosity was estimated at $\approx 10^{37}$ erg/sec and its pulse profile displayed a characteristic double peaked shape (White, Swank & Holt, 1983; Beri et al., 2014). As the source moved closer to its first observed torque reversal, its pulse profile shape started to gradually lose its double peaked shape (Beri et al., 2014). After the first torque reversal in 1990 the source entered a spin-down period, its flux decreased (Chakrabarty et al., 1997) and the pulse profile changed to a broader shape that did not display the previously observed distinct peaks (Krauss et al., 2007). In 2008, 4U 1626-67 underwent a new torque reversal and entered a new spin-up phase that is ongoing until today (Jain, Paul & Dutta, 2010; Camero-Arranz et al., 2012). During the second spin-up period the source luminosity increased by $\sim$2-3 times and the pulse profile shape returned to the double peaked shape (Jain, Paul & Dutta, 2010; Camero-Arranz et al., 2012; Beri et al., 2014).

The pulse profiles of accreting X-ray pulsars exhibit a variety of shapes, ranging from simple sinusoidal-like profiles, to clear double-peaked shapes, and to more complicated broadened profiles with multiple peaks. The observed variety of pulses among different – or sometimes same sources, reflects a variety of possible emission patterns of the polar region of an accreting neutron star. Depending on the mass accretion rate ($\sim$ source luminosity), the emission diagram of the accretion column may switch from a pencil-beam to a fan-beam pattern (Basko & Sunyaev, 1975, 1976). At low luminosities, below $\approx 10^{37}$ erg/sec, the high anisotropy of the photon-electron scattering cross-sections in a high magnetic field of the order of $10^{12}$ G (Canuto, Lodenquai & Ruderman, 1971; Lodenquai et al., 1974), leads to formation of the pencil beam pattern of radiation, oriented parallel to the accretion column (Basko & Sunyaev, 1975). However, at high mass accretion rates, corresponding to luminosities above the critical value of $L_c \sim 10^{37}$ erg/sec (Basko & Sunyaev, 1976; Wang & Frank, 1981), a radiation dominated shock is formed at the distance of a $\sim$few km above the neutron star surface. At high luminosities, the accretion funnel is filled with high density plasma slowly sinking in the gravitational field of the neutron star, resulting in increased opacity in the direction along the magnetic field axis. Consequently, the

emerging X-ray photons predominantly escape from the – optically thin – sides of the accretion funnel and the fan beam pattern of radiation is formed (Fig. 4.3). Pencil-beamed emission is usually associated with single-pulse profiles or more complex shapes if one includes gravitational effects, and different obscuration mechanisms (e.g. Mészáros 1992). Double peaked profiles are indicative of an emission pattern that is fan-beam dominated (e.g. Nagel, 1981; White, Swank & Holt, 1983; Paul et al., 1996, 1997; Rea et al., 2004).

In the present paper we investigate the X-ray spectrum and pulse profile of 4U 1626-67 during two different luminosity states. We present results of spectroscopic and timing analysis of an *XMM-Newton* observation performed in 2003 – during the spin-down low luminosity period, and the latest simultaneous *Chandra* and *RXTE* observations performed in 2010, during the current high luminosity, spin-up period. In Section 4.2 we describe details of our data extraction along with their spectral and timing analysis, followed by interpretation of our results and discussion in Section 4.3 and conclusions in Section 4.4.

## 4.2 Observations, data analysis and results

4U 1626-67 has been observed multiple times by all major X-ray telescopes. For the present work we focus on the *XMM-Newton* observation performed in August 2003, the latest *Chandra* HETGs observation performed in January 2010 and the *RXTE* observation that was performed simultaneously with the *Chandra* observation. The details of the observations used in our analysis are listed in table 4.1. The temporal resolution of the EPIC pn instrument aboard *XMM-Newton* was sufficient for timing analysis of the 2003 data. For the 2010 data, simultaneous *RXTE* observation allowed for high quality timing analysis of the source's light curve during the *Chandra* grating observation. Spectral analysis was carried out using the XSPEC spectral fitting package, version 12.8.2 (Arnaud, 1996). Timing analysis was performed using the standard tools of the XRONOS timing analysis software package, version 5.22.

### 4.2.1 XMM-Newton 2003 observation

During the *XMM-Newton* observation MOS1 detector was operating in timing mode, while MOS2 and pn detectors were operating in imaging mode.

Table 4.1: Details of observations analyzed in this Chapter

| Instrument | obsID | Date | Duration[1] (ks) |
|---|---|---|---|
| *XMM-Newton* | 0152620101 | 2003-08-20 | 58 |
| *Chandra* | 11058 | 2010-01-14 | 77 |
| *RXTE* | P95338-05-01-00 | 2010-01-14 | 10 |

[1]Duration of filtered observations.

The MOS2 detector showed evidence of pile up. For this reason and since the effective area of pn at $\approx 7\,\mathrm{keV}$ is approximately five times higher, we only use the pn data for the present analysis.

### Spectral extraction and analysis

We extracted the source spectrum from a $30''$ circle centered at the source. Background was extracted in compliance with the latest EPIC calibration notes[1] from a source-free region at the same RAWY position as the source region. Spectral extraction was performed using the standard tools provided by the *XMM-Newton* Data Analysis software SAS, version 13.5.0. The resulting spectrum was re-binned to ensure a minimum of 25 counts per energy channel. 4U 1626-67 is known for displaying strong emission features in the 0.5-1.5 keV range. The study of the low energy part of the spectrum of this source is beyond the scope of this paper and has already been performed by Schulz et al. (2001) and Krauss et al. (2007). Therefore, in order to simplify our analysis, we ignored energy channels below 1.5 keV. The remaining channels are sufficient to constrain the source continuum around the iron line.

The spectral continuum was fit with an absorbed black body plus power law model. The temperature of the black body was $\approx 0.3\,\mathrm{keV}$ and the power law photon index $\approx 0.7$. Our fit also required an exponential cutoff at $\approx 8\,\mathrm{keV}$ with a folding energy of $\approx 30\,\mathrm{keV}$. The spectral shape at this energy resembles a mild break in the power law, rather than a genuine exponential cutoff. Addition of the exponential cutoff model improves our fit by a $\Delta\chi^2$ of 30 for 2 dof. Best fit parameters are presented in table 4.2 and are in agreement with the findings of previous authors (e.g. Angelini et al., 1995; Orlandini et al., 1998; Krauss et al., 2007) for the spin-down era of 4U 1626-67. We do

---

[1]http://xmm2.esac.esa.int/docs/documents/CAL-TN-0018.pdf

not detect the iron line, placing an upper limit of $\approx 2.4\,$eV at 90% confidence, for the equivalent width (EW) of a Gaussian emission line centered at 6.4 keV with a 36 eV width. The choice of the values for the line centroid and width was motivated by the corresponding best fit values in the 2010 data, which are described in section 4.2.2. Non-detection of the iron fluorescent line is in agreement with the analysis of Torrejón et al. (2010) based on *Chandra* observations performed a few months before. The 1.5-10 keV luminosity, calculated from the fit, is $\approx 1.3 \times 10^{36}$ erg/sec, assuming a distance of 9 kpc (Chakrabarty, 1998). Luminosity in the 0.01-100 keV, extrapolated from the best fit model, is $\approx 8.4 \times 10^{36}$ erg/sec. The data-to-model ratio vs energy is presented in Fig. 4.1.

**Light curve extraction and analysis**

For our timing analysis we extracted a 2-12 keV light curve from the pn data using standard SAS tools. Photon arrival times were corrected to the solar system barycentre. Using the tools provided in the XRONOS package version 5.22, we determined the pulse period during the *XMM-Newton* observation and created the pulse profile of the source in the 2-12 keV range. The pulse period is measured at $\approx 7.67547(2)$ sec and the corresponding pulse profile is presented in Fig. 4.2.

## 4.2.2 Chandra and RXTE 2010 observation

The January 2010 *Chandra* observation of 4U 1627-67 was performed with the high energy grating. During the *Chandra* observation a simultaneous 10 ks observation was also performed by *RXTE*. For our spectral analysis we used the data obtained by both *Chandra* and *RXTE*. The *RXTE* data were also used for timing analysis.

**Spectral extraction and analysis**

We extracted the spectra of both the medium energy gratings (MEGs) and the high energy gratings (HEGs). The energy range of MEGs is 0.4-5.0 keV and of HEGs is 0.8-10 keV. Extraction was executed using the standard tools[2] provided by the latest CIAO software (vers. 4.6.1). In order to remain consistent with the *XMM-Newton* data analysis, we chose to ignore energy channels

---

[2]http://cxc.harvard.edu/ciao/threads/pointlike/

bellow $1.5\,$keV in the *Chandra* data as well. The *Chandra* data were not re-grouped and were fitted using the standard $\chi^2$ method and the weighting technique suggested by Churazov et al. (1996). We also extracted the source spectrum from *RXTE*-PCA standard-2 data. Spectral extraction and background subtraction were performed using the standard routines provided by the FTOOLS package, following the guidelines described in the *RXTE* Guest Observer Facility[3].

Our analysis of the 2010 *Chandra* spectrum shows that since the 2003 *XMM-Newton* observation the photon index of the power law component has increased to a value of $\approx 1.1$ and the black body temperature to $\approx 0.43\,$keV. Most importantly, our analysis of the *Chandra* spectrum reveals the presence of an iron K$\alpha$ line that was not present in the *XMM-Newton* observation of 2003. The line – modeled using a simple Gaussian – is located at $\approx 6.4\,$keV, has a width of $\sigma \approx 36\,$eV and an EW of $\approx 20\,$eV. Addition of the Gaussian line improves our fit by a $\delta\chi^2$ of 13 for 3 dof, giving the detection of the feature a $2.8\,\sigma$ significance. The presence of the line is confirmed by our fit of the 3-20 keV, *RXTE*-PCA data, which strongly required the presence of a line with the best fit energy of $\approx 6.6\pm 0.2\,$keV and with a $1\,\sigma$ upper limit of $0.4\,$keV for its width. The EW of the line in the *RXTE* fit, has a value of $\approx 35\,$eV and is consistent – within $1\,\sigma$ errors – with the *Chandra* value. While *RXTE* lacks the spectral resolution to constrain the line with the accuracy of *Chandra*, its larger effective area yields a spectrum with substantially higher signal-to-noise ratio, thus providing a detection of the line with more than $4\,\sigma$ significance. The data-to-model ratios for the *Chandra* and *RXTE* observations are presented in Fig. 4.1. The plots are for the best-fit model of the continuum, without the Gaussian emission line. The presence of the iron emission line can be seen clearly, particularly in the *RXTE* data that have higher signal-to-noise ratio. The 1.5-10 keV luminosity, calculated from the *Chandra* fit, is $\approx 4 \times 10^{36}$ erg/sec. Luminosity in the 0.01-100 keV, extrapolated from the best fit model, is $\approx 3 \times 10^{37}$ erg/sec. Best fit values for the spectral parameters obtained from *Chandra* and *RXTE* spectral analysis are presented in table 4.2.

---

[3]http://heasarc.gsfc.nasa.gov/docs/xte/recipes/pca_spectra.html

**Light curve extraction and analysis**

For the timing analysis of the 2010 observation we made use of the *RXTE*-PCA good xenon data that have a time resolution of $1\,\mu$s. Using the standard tools described in the previous sections, we extracted and analyzed the source's light curve. We measured the pulsation period at $\approx 7.67797(6)\,$sec and produced the corresponding pulse profile in the 2-12 keV range. The pulse profile is presented in Fig. 4.2.

## 4.3 Discussion

We have performed spectral and timing analysis of two different observations of 4U 1626-67 taken during low and high luminosity periods of the source. We detected a faint, narrow K$\alpha$ emission line of iron at 6.4 keV in the 2010 *Chandra* and *RXTE* data, during the high luminosity state of the source. This feature was not present in 2003 (Fig. 4.1) when the source luminosity was less than $10^{37}$ erg/sec. Furthermore, the appearance of the line coincides with a major alteration in the source's pulse profile. During the 2010 observation – in which the iron line is detected – the pulse profile of the source has a characteristic double peaked shape that is radically different from the pulse profile of the 2003 observation. Below, we discuss the details of the iron emission line and propose that its appearance is caused by the modification of the emission diagram of the accretion column caused by the change of the mass accretion rate. The same modification of the emission diagram leads to changes in the shape of the pulse profile.

### 4.3.1 The iron K$\alpha$ line

The iron K$\alpha$ line detected in the spectrum of the 2010 *Chandra* observation is centered at 6.4 keV, has a small width of the order of $\approx$36 eV and an EW of $\approx$18 eV. Parameters of iron lines observed in the spectra of accreting X-ray pulsars can vary significantly from source to source. They are typically observed at energies of $\approx 6.4 - 6.8$ keV with widths that can be in excess of 0.5 keV and EWs of the order of 0.1 to 0.4 keV (e.g. White, Swank & Holt, 1983; Tanaka, 1986). These emission lines may be due reflection off the accretion disk and/or the donor star (e.g. Basko, Sunyaev & Titarchuk, 1974). They can also be due to Alfvén shell emission, as proposed by Basko (1980). In his work, Basko argues that iron emission lines originating in

Table 4.2: Best fit parameters for the XMM-Newton, Chandra and RXTE-PCA spectra. All errors are $1\sigma$.

| Model parameters | XMM-Newton 2003 | Chandra 2010 | RXTE-PCA 2010 |
|---|---|---|---|
| $nH^a$ ($10^{21}$ cm$^{-2}$) | 1.00 | 1.00 | 1.00 |
| *Power Law* | | | |
| $\Gamma$ | $0.70^b \pm 0.01$ | $1.13 \pm 0.03$ | $1.04 \pm 0.02$ |
| norm$^c$ | $5.81 \pm 0.07$ | $34.9 \pm 1.5$ | $14.7^{+0.5}_{-0.6}$ |
| *Black Body* | | | |
| kT (keV) | $0.30 \pm 0.01$ | $0.43 \pm 0.01$ | $0.61 \pm 0.07$ |
| norm$^d$ | $1.19 \pm 0.04$ | $6.95 \pm 0.41$ | $2.56^{+0.59}_{-0.38}$ |
| *Iron Line* | | | |
| Centroid E (keV) | $6.39^e$ | $6.39^{+0.02}_{-0.01}$ | $6.64^{+0.20}_{-0.25}$ |
| Width $\sigma$ (eV) | $36.4^e$ | $36.4^{+3.25}_{-4.11}$ | $<400$ |
| Flux$^f$ | $<0.39$ | $7.66^{+0.26}_{-0.24}$ | $7.53^{+3.73}_{-3.64}$ |
| EW (eV) | $<2.41$ | $18.0^{+6.2}_{-5.6}$ | $35.1^{+17.4}_{-16.9}$ |
| $L^g_{1.5-10\text{keV}}$ | 1.29 | 4.00 | $2.02^h$ |
| $\chi^2$/dof | 1731/1693 | 3073/3008 | 38.15/38 |

[a] Parameter frozen at total galactic HI column density provided by the HEASARC nH tool (Dickey & Lockman, 1990; Kalberla et al., 2005).

[b] With a high energy cut off at $7.91^{+0.30}_{-0.23}$ keV with an e-folding energy of $29.2^{+8.70}_{-8.36}$ keV, modeled using XSPEC model **highecut.**

[c] $10^{-3}$ ph keV$^{-1}$ cm$^{-2}$ s$^{-1}$.

[d] $10^{-4}$ L$_{39}$/D$^2_{10\text{kpc}}$ were L$_{39}$ is luminosity in units of $10^{39}$ erg/sec and D$_{10\text{kpc}}$ is distance in units of 10kpc.

[e] Parameter frozen.

[f] $10^{-5}$ ph cm$^{-2}$s$^{-1}$.

[g] $10^{36}$ erg/sec.

[h] Calculated in the 3-20 keV range.
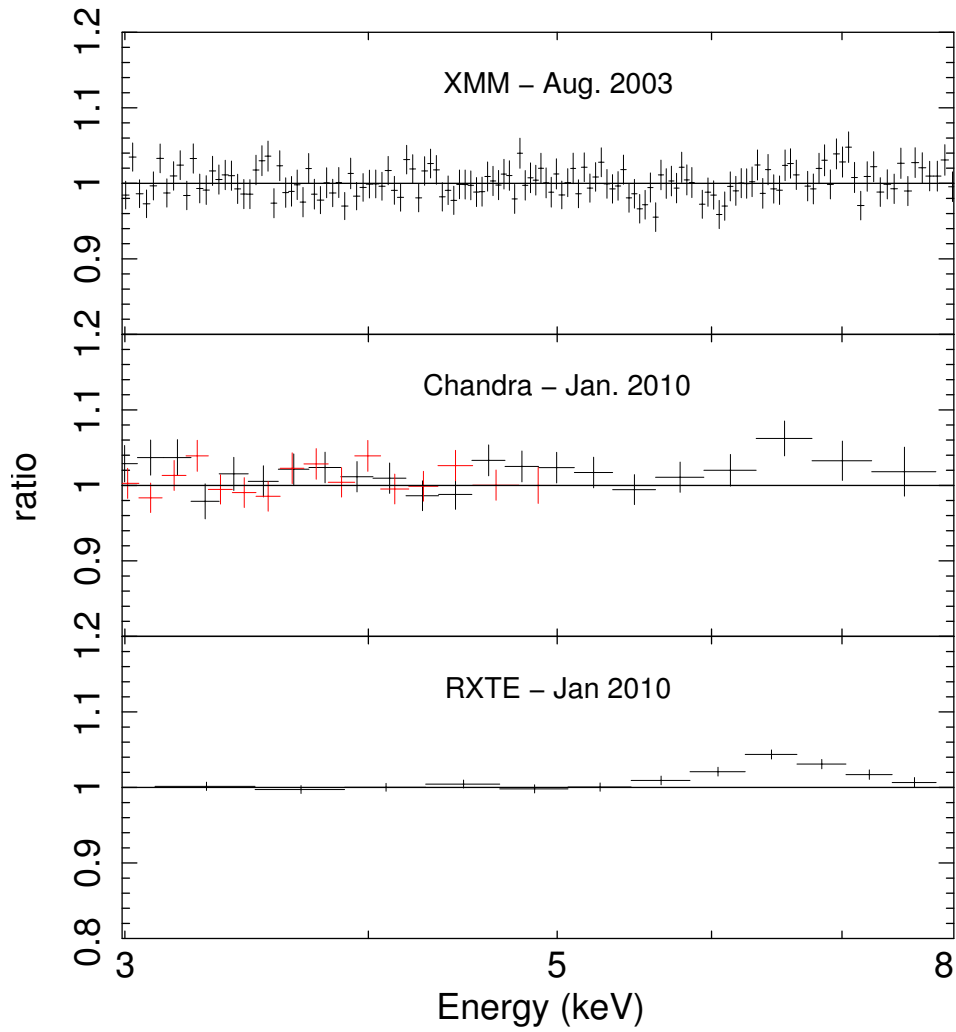
Figure 4.1: Ratio of the data to the continuum model for the 2003 XMM and 2010 Chandra and RXTE observations. The data have been rebinned for clarity; the 3-8 keV energy range is shown.
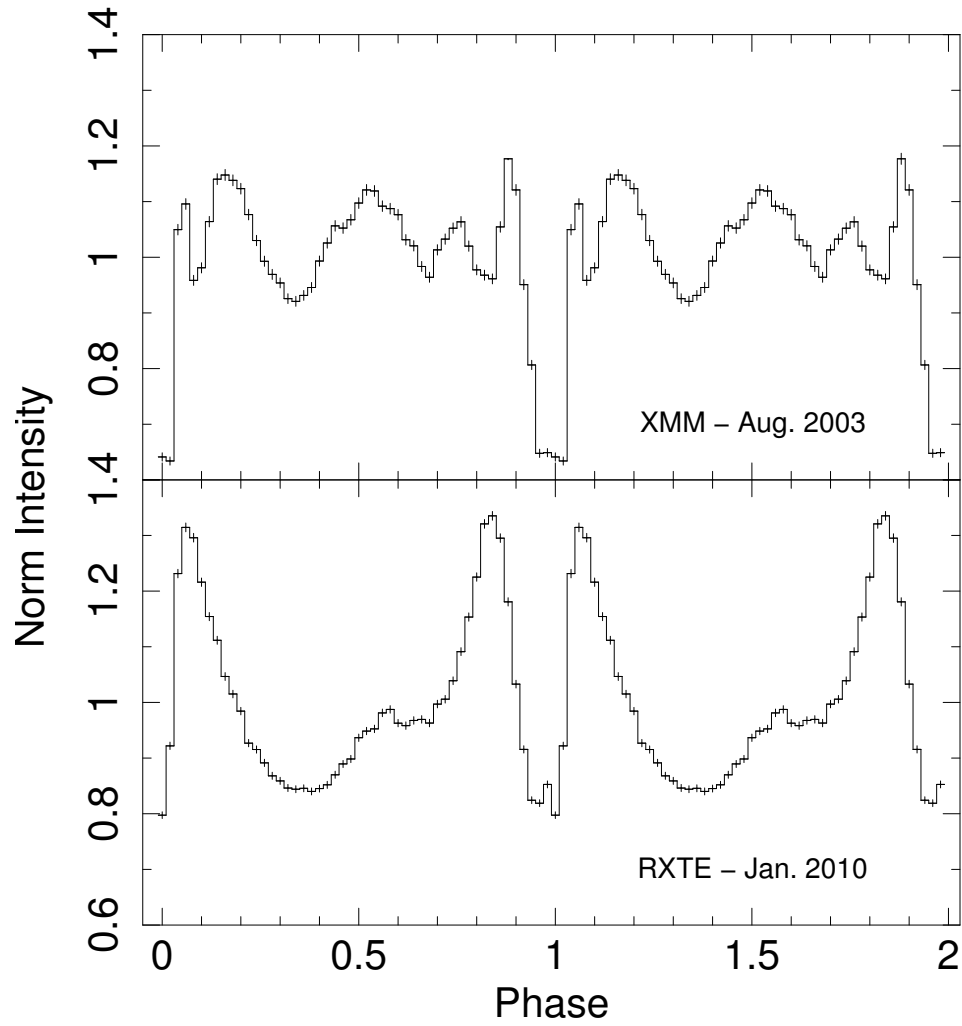
Figure 4.2: The 2-12 keV pulse profile of 4U 1626-67 from XMM and RXTE observations. The switch to a distinct double horned shape in the 2010 RXTE observation is evident. The profiles have been arbitrarily shifted in phase so that the minimum appears at the pulse phase 1.0.

the Alfvén shell are expected to be centered at $> 6.5\,\mathrm{keV}$ are broader and brighter, with EWs exceeding $0.3\,\mathrm{keV}$. On the other hand, fluorescent iron lines in pulsars produced by reflection, are generally narrower, centered at $\approx 6.4\,\mathrm{keV}$ and have EWs of the order of 50-100 eV. The line properties of the 2010 *Chandra* observation are more consistent with reflection from either the cool surface of the donor star or the outer parts of the accretion disk.

For a binary system consisting of a $1.4\mathrm{M}_\odot$ NS accretor and a $0.02\mathrm{M}_\odot$ WD donor (e.g. Chakrabarty, 1998), the Roche lobe of the WD subtends a solid angle of $\sim 5.1 \times 10^{-2}\,\mathrm{sr}$ as viewed from the neutron star. Assuming that the emission source is located in the accretion column, at $\sim 15\,\mathrm{km}$ above the the disk plane and that the disk is truncated at the magnetospheric radius (see eq. 4.1 and discussion below), the disk will subtend a solid angle of $\sim 1.3 \times 10^{-2}\,\mathrm{sr}$ as viewed from the emission source, ignoring possible flaring of the disk. This is smaller than the solid angle subtended by the WD donor, however, disk flaring and non-isotropic emission pattern can change this number and the relative contributions of the disk and the surface of the donor star. Indeed, the width of the line measured by the high energy grating, $\approx 36$ eV, corresponds to velocities of $\approx 1700$ km/s. Such velocities are more typical for the accretion accretion disk, rather than for the surface of the donor star, suggesting that the majority of the line emission originates from the disk. Furthermore, actual contributions of the accretion disk and the donor star to the observed fluorescent line flux are determined by not only the solid angle, but also depend on the emission diagram of the primary emission and the angles of the line of sight to the normal of the surfaces of the disk and the star. The latter are mainly defined by the inclination of the binary system. As for the former, in the case of the fan beam, for example, it is quite possible that much larger fraction of the accretion column emission is intercepted by the accretion disk, rather than by the donor star.

The truncation radius of the accretion disk due to the magnetic field of the neutron star can be estimated as follows (e.g. Ghosh, Pethick & Lamb, 1977).

$$R_m = \left( \frac{B^2 R_{NS}{}^6}{\dot{M}\sqrt{2GM_{NS}}} \right)^{2/7} \tag{4.1}$$

The magnetic field of the neutron star in 4U1626–67 is known from the cyclotron line measurements, $B \approx 3 \times 10^{12}$ (e.g. Orlandini et al., 1998). Assuming a $1.4M_\odot$ neutron star of the radius of $R_{NS} \approx 12$ km, accreting at the mass accretion rate of $\dot{M} \approx 2.7 \times 10^{-9}\,M_\odot/yr$ corresponding to the

observed luminosity of $\approx 3 \times 10^{37}$ erg/sec, the magnetospheric radius is $R_m \approx$ $7.3 \times 10^8$ cm or $R_m \approx 1750\,R_s$, where $R_s$ is the Schwarzschild radius ($R_s = 2G\mathrm{M_{NS}}/c^2$). The outer disk radius will extend to a substantial fraction (up to 0.8, e.g. Lasota, 2001) of the Roche lobe radius, which is $\approx 2.2 \times 10^{10}$ cm, assuming a white dwarf donor of $0.02\,M_\odot$ (e.g. Chakrabarty, 1998).

The observed line width of $\approx 36.4$ eV corresponds to a line-of-sight velocity of $\approx$1700 km/sec. For a disk inclination angle of $20^o$ (e.g. Verbunt, Wijers & Burm, 1990; Chakrabarty, 1998), the 3D velocity is $\approx$5000 km/sec. Keplerian velocity reaches this value at the distance of $\approx$1800 $R_s$ from the compact object. This value is in good agreement with our estimate of the magnetospheric radius, suggesting that the fluorescent line is produced near the inner edge of the accretion disk truncated by the magnetic field of the neutron star. An accretion disk that is heated through viscus dissipation (Shakura & Sunyaev, 1973) and is truncated at this radius, cannot reach a temperature higher than $\approx 5 - 6\times\ 10^4\,K$. Obviously, at these temperatures any iron that is present in the disk will be in a low ionization or neutral state and its fluorescent K-alpha line will be centered at $\approx$6.4 keV (e.g. Bearden, 1967) as observed.

Although the observed line energy and width, are consistent with what should be expected for this system, the line itself is quite faint. With an EW of $\approx$18 eV, it is significantly fainter than the EWs of $\approx$ 40-100 eV of iron lines usually observed in disk reflection spectra of non-pulsar LMXBs (e.g. Cackett et al., 2010). This could be due to the fact that the truncated accretion disk around the highly magnetised neutron star subtends a significantly smaller solid angle than in the case of "normal" LMXBs. However, the non-isotropic emission diagram of the accretion column can compensate for the smaller solid angle, for example in the case of the fan-beam as discussed above (Fig. 4.3). Indeed, narrow fluorescent lines of iron, of appreciable equivalent width in the $\sim$ 70 eV range, were previously detected in the spectra of some accreting X-ray pulsars in low-mass X-ray binary systems. For example, a narrow line at $\approx$6.4 keV was detected in GX 1+4 ( EW$\sim$70 eV, Paul et al., 2005) and in Her X-1 (EW$\sim$65 eV Endo, Nagase & Mihara, 2000; Naik & Paul, 2003). The 6.4 keV line, we found in 4U 1626-67, is significantly fainter than in those sources.

If the reflected component is not strongly reduced due to the geometry of the system (the detection of O and Ne emission features by Krauss et al. (2007) and Schulz et al. (2001) suggests it is not), then the faintness of the iron line can be explained by the fact that 4U 1626-67 is an UCXB with a

C/O-rich donor (Schulz et al., 2001; Homer et al., 2002; Nelemans, Jonker & Steeghs, 2006; Werner et al., 2006). In chapters 2 and 3 (see also Koliopanos, Gilfanov & Bildsten, 2013; Koliopanos et al., 2014) we demonstrated that the iron K$\alpha$ line is strongly attenuated in reflection spectra of C/O or O/Ne dominated disks. This is due to screening of the presence of iron by the overabundant oxygen. In particular, in the C/O dominated material the main interaction process for an $E \approx 7$ keV photon is absorption by oxygen rather than by iron, contrary to the case of "standard" LMXBs with main sequence or red giant donors where the accretion disk has the chemical composition close to Solar.

To further investigate this hypothesis, we ran our simulation from Koliopanos et al. 2013 for a primary radiation with a power law spectrum with a photon index of 1.1. For simplicity, we assumed that the primary radiation is emitted isotropically by a point source above the disk surface, in a lamppost configuration. We have collected the reflected emission for viewing angles in the range $15^{\circ} - 25^{\circ}$. We found that in order to produce an output spectrum with the iron K$\alpha$ line with an EW of $\approx 18$ eV – as observed – we need an O/Fe ratio in the disk that is 68 times the solar value. Note that the maximum value of the O/Fe ratio that corresponds to the chemical composition of a C/O white dwarf – in which all hydrogen and helium has been converted to carbon and oxygen – is $\approx 77$ times the solar value. This result suggests that the donor star in 4U1626–67 is a C/O or O/Ne/Mg white dwarf, in a perfect agreement with the previous work which proposed that this source is a UCXB with a C/O white dwarf donor (Schulz et al., 2001; Krauss et al., 2007). To conclude, we note that a lamppost geometry is obviously not an accurate representation of the emission of the accretion column. However, it can serve as a sufficient first approximation which demonstrates that the small equivalent width of the iron line in the spectrum of 4U 1626-67 can be easily explained in terms of reflection from a C/O rich disk.

### 4.3.2 The origin of the iron line variability.

The iron line was not detected in the 2003 *XMM-Newton* spectrum, with a tight upper limit of $\approx 2.4$ eV ($1\sigma$). A possible explanation for the line variability is suggested by the timing analysis of the source. In particular, we notice that the line is present during the high luminosity state of the source in which the pulse profile has switched to a characteristic double peaked shape.
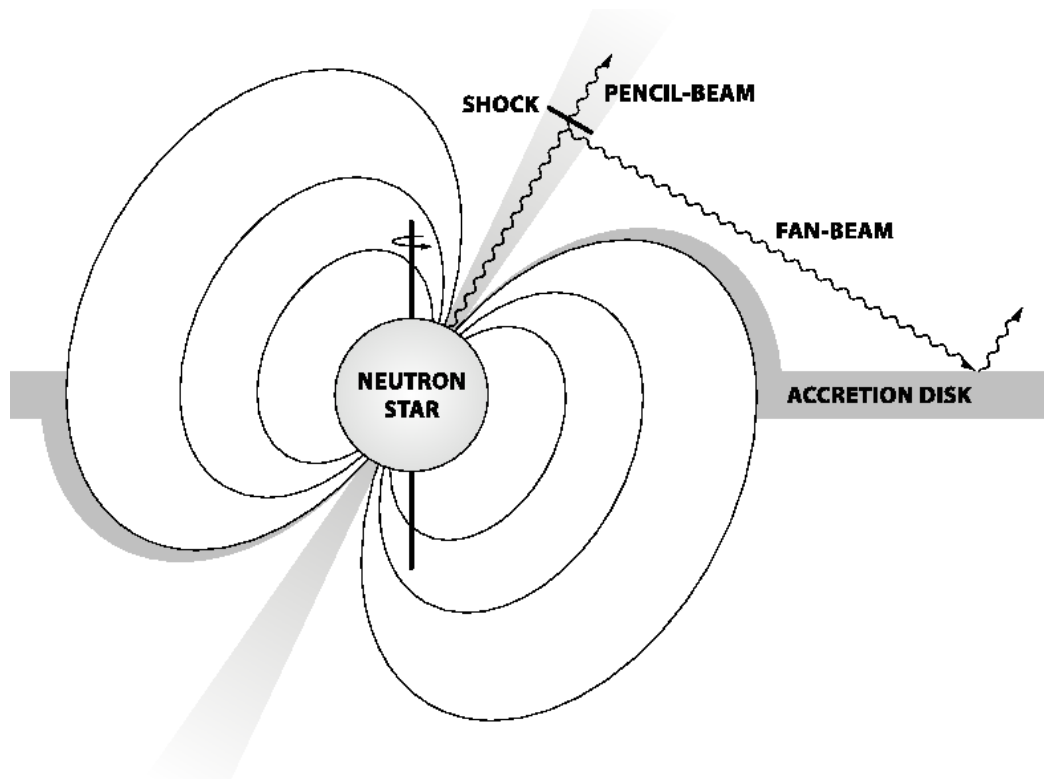
Figure 4.3: Schematic representation of the pencil and fan-beam emission in an accreting X-ray pulsar. Note that the drawing is only aimed to illustrate the difference of the disk illumination at different emission patterns of the accretion column and is not meant to realistically reproduce the geometry of an accreting strongly magnetised neutron star. In particular, for viewing clarity, the distance of the shock from the NS surface has been exaggerated, as well as the size of the neutron star itself, whereas the inner disk radius has been depreciated.

We argue that both the appearance of the fluorescent line of iron and the change of the shape of the pulse profile are the result of a major modification in the emission diagram of the accretion column. Such a modification may be caused by the increase of the mass accretion rate, as proposed by Basko & Sunyaev (1975). Observationally, in the case of 4U1626–67, the increase of the mass accretion rate manifests itself as a more than 3-fold increase of the source luminosity and acceleration of the neutron star spin.

At low luminosity, the emission of the accretion column is concentrated in a beam that is oriented along the magnetic field axis (pencil-beam emission) Basko & Sunyaev (1975). Depending on the angle between the rotation axis and magnetic dipole of the neutron star, the magnetic field axis – and hence the beamed radiation – will be mostly directed away from the accretion disk (Fig. 4.3). Due to the decreased flux towards the disk, disk reflection features in the observed spectrum will be significantly suppressed, including the iron line emission. Note that the latter is weakened further due to the C/O dominated chemical composition of the accretion disk.

As mass accretion rate increases, the emission diagram of the accretion column changes to the fan-beam pattern Basko & Sunyaev (1976). This modification in the emission diagram of the accretion column, causes most of the radiation to be beamed towards the accretion disk (Fig. 4.3), resulting in a significant boost of the emission that is reflected off the disk and the appearance of the detectable K$\alpha$ line of iron. As the disk is truncated by the magnetic field of the neutron star at large distance form the latter, relativistic broadening of the line is insignificant and the line is rather narrow. The line is also rather faint, due to the fact that the disk is made of C/O-enriched material. The fan-beam diagram of the emission from the accretion column further manifests itself throughout the characteristic double peaked shape of the pulse profile.

## 4.4   Summary and conclusions

We have discovered the appearance of a narrow Fe K$\alpha$ emission line in the spectrum of 4U 1626-67 correlated with a major change in the shape of its pulse profile. The line was detected at a moderate level of $EW \approx 18$ eV during a period of high luminosity in 2010, when the pulse profile of the source had a characteristic double peaked shape. The line was not detected in 2003 with a tight upper limit of 2.4 eV ($1\sigma$) when the source was in a

low luminosity state and the shape of its pulse profile had a clearly different, broader shape. We argue that both changes are caused by the same reason – a significant modification of the emission diagram of the accretion column, from a pencil beam to a fan beam pattern. This change was caused by an increase in the mass accretion rate, as was theoretically predicted by Basko & Sunyaev in 1976. The lower than typical equivalent width of the iron line in the high luminosity state is due to C/O dominated chemical composition of the accretion disk.

# Bibliography

Angelini L., White N. E., Nagase F., Kallman T. R., Yoshida A., Takeshima T., Becker C., Paerels F., 1995, ApJ, 449, L41

Arnaud K. A., 1996, in Astronomical Society of the Pacific Conference Series, Vol. 101, Astronomical Data Analysis Software and Systems V, Jacoby G. H., Barnes J., eds., p. 17

Basko M. M., 1980, A&A, 87, 330

Basko M. M., Sunyaev R. A., 1975, A&A, 42, 311

Basko M. M., Sunyaev R. A., 1976, MNRAS, 175, 395

Basko M. M., Sunyaev R. A., Titarchuk L. G., 1974, A&A, 31, 249

Bearden J. A., 1967, Reviews of Modern Physics, 39, 78

Beri A., Jain C., Paul B., Raichur H., 2014, MNRAS, 439, 1940

Bildsten L., Deloye C. J., 2004, ApJ, 607, L119

Cackett E. M. et al., 2010, ApJ, 720, 205

Camero-Arranz A., Pottschmidt K., Finger M. H., Ikhsanov N. R., Wilson-Hodge C. A., Marcu D. M., 2012, A&A, 546, A40

Canuto V., Lodenquai J., Ruderman M., 1971, Phys. Rev. D, 3, 2303

Chakrabarty D., 1998, ApJ, 492, 342

Chakrabarty D. et al., 1997, ApJ, 474, 414

Churazov E., Gilfanov M., Forman W., Jones C., 1996, ApJ, 471, 673

Degenaar N., Miller J. M., Harrison F. A., Kennea J. A., Kouveliotou C., Younes G., 2014, ApJ, 796, L9

Deloye C. J., Bildsten L., 2003, ApJ, 598, 1217

Deloye C. J., Bildsten L., Nelemans G., 2005, ApJ, 624, 934

Dickey J. M., Lockman F. J., 1990, ARA&A, 28, 215

Endo, T., Nagase, F., & Mihara, T. 2000, PASJ, 52, 223

Ghosh P., Pethick C. J., Lamb F. K., 1977, ApJ, 217, 578

Giacconi R., Murray S., Gursky H., Kellogg E., Schreier E., Tananbaum H., 1972, ApJ, 178, 281

Homer L., Anderson S. F., Wachter S., Margon B., 2002, AJ, 124, 3348

Iben, Jr. I., Tutukov A. V., Yungelson L. R., 1995, ApJS, 100, 233

Jain C., Paul B., Dutta A., 2010, MNRAS, 403, 920

Kalberla P. M. W., Burton W. B., Hartmann D., Arnal E. M., Bajaja E., Morras R., Pöppel W. G. L., 2005, A&A, 440, 775

Koliopanos F., Gilfanov M., Bildsten L., 2013, MNRAS, 432, 1264

Koliopanos F., Gilfanov M., Bildsten L., Trigo M. D., 2014, MNRAS, 442, 2817

Krauss M. I., Schulz N. S., Chakrabarty D., Juett A. M., Cottam J., 2007, ApJ, 660, 605

Lasota, J.-P. 2001, New A Rev., 45, 449

Lodenquai J., Canuto V., Ruderman M., Tsuruta S., 1974, ApJ, 190, 141

Mészáros P., 1992, High-energy radiation from magnetized neutron stars.

Middleditch J., Mason K. O., Nelson J. E., White N. E., 1981, ApJ, 244, 1001

Nagel W., 1981, ApJ, 251, 288

Naik S., Paul B., 2003, A&A, 401, 265

Nelemans G., Jonker P. G., Steeghs D., 2006, MNRAS, 370, 255

Orlandini M. et al., 1998, ApJ, 500, L163

Paul B., Agrawal P. C., Rao A. R., Manchanda R. K., 1996, Bulletin of the Astronomical Society of India, 24, 729

Paul B., Agrawal P. C., Rao A. R., Manchanda R. K., 1997, A&A, 319, 507

Paul B., Dotani T., Nagase F., Mukherjee U., Naik S., 2005, ApJ, 627, 915

Podsiadlowski P., Rappaport S., Pfahl E. D., 2002, ApJ, 565, 1107

Rappaport S., Markert T., Li F. K., Clark G. W., Jernigan J. G., McClintock J. E., 1977, ApJ, 217, L29

Rea N., Israel G. L., Di Salvo T., Burderi L., Cocozza G., 2004, A&A, 421, 235

Savonije G. J., de Kool M., van den Heuvel E. P. J., 1986, A&A, 155, 51

Schulz N. S., Chakrabarty D., Marshall H. L., Canizares C. R., Lee J. C., Houck J., 2001, ApJ, 563, 941

Shakura N. I., Sunyaev R. A., 1973, A&A, 24, 337

Tanaka Y., 1986, in Lecture Notes in Physics, Berlin Springer Verlag, Vol. 255, IAU Colloq. 89: Radiation Hydrodynamics in Stars and Compact Objects, Mihalas D., Winkler K.-H. A., eds., p. 198

Torrejón J. M., Schulz N. S., Nowak M. A., Kallman T. R., 2010, ApJ, 715, 947

Tutukov A. V., Yungelson L. R., 1993, Astronomy Reports, 37, 411

Verbunt F., van den Heuvel E. P. J., 1995, X-ray Binaries, 457

Verbunt F., Wijers R. A. M. J., Burm H. M. G., 1990, A&A, 234, 195

Wang Y.-M., Frank J., 1981, A&A, 93, 255

Werner K., Nagel T., Rauch T., Hammer N. J., Dreizler S., 2006, A&A, 450, 725

White N. E., Swank J. H., Holt S. S., 1983, ApJ, 270, 711

Yungelson L. R., Nelemans G., van den Heuvel E. P. J., 2002, A&A, 388, 546

# Chapter 5

# Conclusions

In this dissertation we studied the spectral and timing properties of ultra compact X-ray binaries (UCXBs). We showed that the iron K$\alpha$ fluorescent emission line, often detected in the spectra of X-ray binaries, can be used as a diagnostic for the nature of the donor star in UCXBs. Furthermore, we make an important discovery concerning the emission diagram of the accretion column of a unique UCXB that contains a neutron star with a high magnetic field.

The primary X-ray radiation of accreting X-ray binaries is often reflected off the accretion disk that encompasses the neutron star or black hole accretor. The reflected component also enters the line of sight of the observer. The shape of the reflected emission and more importantly the shape and strength of emission lines with which it is enriched, is an invaluable source of information regarding the chemical composition of the disk. In this dissertation, we showed that the non-solar composition of the donor star in UCXBs may have a dramatic effect on the reflected spectra. Specifically, we expect a significant modification of the strength of the fluorescent lines of various elements, compared to their strengths in the case of accretion disks with solar-like chemical composition.

To investigate the effects of non-solar composition on the reflected emission, we assumed the hypothetical case of a slab of neutral material with infinite depth and two abundance patterns, that simulate a He and a C/O white dwarf. We found that non-solar composition of the reprocessing material, mostly affects the strength of the fluorescent line of iron at $6.4\,\mathrm{keV}$. As their abundances increase, the strength of the fluorescent lines of carbon and oxygen also increase. However, their equivalent widths saturate at the (sub-

)eV level due to the effect of self-screening. On the other hand, the increasing amounts of oxygen in the disk intensifies its screening effects on the presence of heavy elements. As a result the equivalent width of the iron emission line decreases significantly, and for the chemical composition that corresponds to a C/O white dwarf, the iron fluorescent line is expected to become very faint. Namely, in a C/O-dominated material, incident photons with energies $\gtrsim 7\,\mathrm{keV}$, will be mostly absorbed by oxygen rather than by iron, contrary to the case of solar composition. This effect is significantly milder in the case of helium-rich material due to its lower ionization threshold. Furthermore, helium will be fully ionized throughout the inner parts of UCXB accretion disks. Therefore, in the case of UCXBs with He-rich donors, the equivalent widths of fluorescent lines of all major elements will have their nominal solar abundance value, while in the case of UCXBs with C/O or O/Ne/Mg-rich donors the strength of the iron fluorescent line is expected to be $\sim$ ten times less than its usually observed value. Therefore, measuring the strength of the fluorescent line of iron, is a useful diagnostic of the chemical composition of the donor star in UCXBs

These effects are dependent on the ionization state of the disk. Namely, if oxygen in the inner parts of a C/O rich disk becomes full ionized then its screening effect on the emission line of iron will seize to exist. By comparing ionization curves with the distribution of the effective temperature in the Shakura-Sunyaev disk, we demonstrated that this should happen at mass accretion rates that correspond to a luminosity of $\log(L_\mathrm{X}) \sim 37.5 - 38$. For $\log(L_\mathrm{X}) \lesssim 37$ oxygen will only be partially ionized and so our above conclusions will hold. Namely, the strength of the 6.4 keV line of iron can be an effective diagnostic of the nature of the donor star in UCXBs. In particular, a faint or absent line points towards a C/O or O/Ne/Mg white dwarf, while the presence of a strong iron line, suggests a He-rich donor.

Following up on our theoretical estimations, we investigated X-ray observations of five UCXBs, searching for the iron line in their spectra. Based on our model, we concluded that three objects in our sample (2S 0918-549, XTE J1807-294 and 4U 0513-40) have an accretion disk with an O/Fe ratio that is at least $\approx 10$ times higher than the solar value. Since, these sources are known UCXBs, these findings suggests a C/O or O/Ne/Mg-rich donor. Furthermore, we confirm the presence of a strong Fe K$\alpha$ line in the spectra of the remaining two systems (4U 0614+091 and 4U 1916-05) which, based on our predictions, is an indication of a He-rich donor. Our findings are supported by optical spectroscopy in the case of 2S 0918-549 and 4U 1916-05.

Our estimation of a He-rich donor in 4U 0614+091 deviated from previous assertions that favored a C/O-rich donor. However, the presence of He-rich accreting material can readily explain the source's frequent bursting activity.

In accreting neutron star X-ray binaries with high magnetic fields (of the order of $10^{12}$ G), the primary emission originates in an accretion column that is formed in the vicinity the neutron star polar caps. The emission diagram of the accretion column will have a beamed pattern. Its direction and shape – which largely dependents on the mass accretion rate of the source – affects the shape of the pulse profile of the source and – as we advocate in this dissertation – its spectral features. Particularly, the iron K$\alpha$ emission line. In the final chapter of this dissertation we discover the emergence of a narrow Fe K$\alpha$ emission line in the spectrum of X-ray pulsar 4U 1626-67. The appearance is correlated with an increase in the source luminosity and a crucial modification in the shape of its pulse profile. Namely, we detect the line during a high luminosity phase, when the pulse profile of the source has a distinctive double peaked shape. The line was not present during previous observations, when the source luminosity was $\sim$ four times lower and the pulse profile was missing its two characteristic peaks. We maintain that the appearance of the line and the change of the pulse profile shape are both the result of an extensive alteration of the emission diagram of the accretion column, from a pencil beam to a fan beam pattern. This change was caused by an increase in the mass accretion rate, in agreement with the predictions of Basko & Sunyaev in 1976.

.

# Bibliography

Althaus L. G., Córsico A. H., Isern J., García-Berro E., 2010, A&A Rev., 18, 471

Angelini L., White N. E., Nagase F., Kallman T. R., Yoshida A., Takeshima T., Becker C., Paerels F., 1995, ApJ, 449, L41

Arnaud K. A., 1996, in Astronomical Society of the Pacific Conference Series, Vol. 101, Astronomical Data Analysis Software and Systems V, Jacoby G. H., Barnes J., eds., p. 17

Asai K., Dotani T., Nagase F., Mitsuda K., 2000, ApJS, 131, 571

Bachetti M. et al., 2014, Nature, 514, 202

Bai T., 1979, Sol. Phys., 62, 113

Ballantyne D. R., Fabian A. C., Ross R. R., 2002, MNRAS, 329, L67

Ballantyne D. R., Ross R. R., Fabian A. C., 2001, MNRAS, 327, 10

Bambynek W., Crasemann B., Fink R. W., Freund H.-U., Mark H., Swift C. D., Price R. E., Rao P. V., 1972, Reviews of Modern Physics, 44, 716

Basko M. M., 1978, ApJ, 223, 268

Basko M. M., 1980, A&A, 87, 330

Basko M. M., Sunyaev R. A., 1975, A&A, 42, 311

Basko M. M., Sunyaev R. A., 1976, MNRAS, 175, 395

Basko M. M., Sunyaev R. A., Titarchuk L. G., 1974, A&A, 31, 249

Bearden J. A., 1967, Reviews of Modern Physics, 39, 78

Beri A., Jain C., Paul B., Raichur H., 2014, MNRAS, 439, 1940

Bildsten L., 1995, ApJ, 438, 852

Bildsten L. et al., 1997, ApJS, 113, 367

Bildsten L., Deloye C. J., 2004, ApJ, 607, L119

Boirin L., Parmar A. N., Barret D., Paltani S., Grindlay J. E., 2004, A&A, 418, 1061

Cackett E. M., Altamirano D., Patruno A., Miller J. M., Reynolds M., Linares M., Wijnands R., 2009, ApJ, 694, L21

Cackett E. M. et al., 2010, ApJ, 720, 205

Camero-Arranz A., Pottschmidt K., Finger M. H., Ikhsanov N. R., Wilson-Hodge C. A., Marcu D. M., 2012, A&A, 546, A40

Campana S., Ravasio M., Israel G. L., Mangano V., Belloni T., 2003, ApJ, 594, L39

Canuto V., Lodenquai J., Ruderman M., 1971, Phys. Rev. D, 3, 2303

Chakrabarty D., 1998, ApJ, 492, 342

Chakrabarty D. et al., 1997, ApJ, 474, 414

Chakrabarty D., Morgan E. H., 1998, Nature, 394, 346

Christian D. J., White N. E., Swank J. H., 1994, ApJ, 422, 791

Churazov E., Gilfanov M., Forman W., Jones C., 1996, ApJ, 471, 673

Churazov E., Sazonov S., Sunyaev R., Revnivtsev M., 2008, MNRAS, 385, 719

Cornelisse R. et al., 2002, A&A, 392, 885

Cumming A., 2003, ApJ, 595, 1077

Cumming A., Bildsten L., 2001, ApJ, 559, L127

D'Avanzo P., Campana S., Casares J., Covino S., Israel G. L., Stella L., 2009, A&A, 508, 297

Deloye C. J., Bildsten L., 2003, ApJ, 598, 1217

Deloye C. J., Bildsten L., Nelemans G., 2005, ApJ, 624, 934

den Herder J. W. et al., 2001, A&A, 365, L7

Di Salvo T. et al., 2009, MNRAS, 398, 2022

Di Salvo T., Iaria R., Méndez M., Burderi L., Lavagetto G., Robba N. R., Stella L., van der Klis M., 2005, ApJ, 623, L121

Dickey J. M., Lockman F. J., 1990, ARA&A, 28, 215

Done C., Gierliński M., Kubota A., 2007, A&A Rev., 15, 1

Dupuis J., Fontaine G., Pelletier C., Wesemael F., 1992, ApJS, 82, 505

Egron E. et al., 2013, A&A, 550, A5

Endo T., Nagase F., Mihara T., 2000, PASJ, 52, 223

Fabian A. C., Rees M. J., Stella L., White N. E., 1989, MNRAS, 238, 729

Falanga M. et al., 2005, A&A, 436, 647

Feldman U., 1992, Phys. Scr, 46, 202

Fiocchi M., Bazzano A., Natalucci L., Landi R., Ubertini P., 2011, MNRAS, 414, L41

Galloway D. K., Muno M. P., Hartman J. M., Psaltis D., Chakrabarty D., 2008, ApJS, 179, 360

García J., Dauser T., Reynolds C. S., Kallman T. R., McClintock J. E., Wilms J., Eikmann W., 2013, ApJ, 768, 146

García J., Kallman T. R., 2010, ApJ, 718, 695

García-Berro E., Althaus L. G., Córsico A. H., Isern J., 2008, ApJ, 677, 473

Garmire G. P., Bautz M. W., Ford P. G., Nousek J. A., Ricker, Jr. G. R., 2003, in Society of Photo-Optical Instrumentation Engineers (SPIE) Conference Series, Vol. 4851, X-Ray and Gamma-Ray Telescopes and Instruments for Astronomy., Truemper J. E., Tananbaum H. D., eds., pp. 28–44

George I. M., Fabian A. C., 1991, MNRAS, 249, 352

Ghosh P., Pethick C. J., Lamb F. K., 1977, ApJ, 217, 578

Giacconi R., Gursky H., Paolini F. R., Rossi B. B., 1962, Physical Review Letters, 9, 439

Giacconi R., Murray S., Gursky H., Kellogg E., Schreier E., Tananbaum H., 1972, ApJ, 178, 281

Giacconi R., Rossi B., 1960, J. Geophys. Res., 65, 773

Gil-Pons P., García-Berro E., 2001, A&A, 375, 87

Gilfanov M., 2010, in Lecture Notes in Physics, Berlin Springer Verlag, Vol. 794, Lecture Notes in Physics, Berlin Springer Verlag, Belloni T., ed., p. 17

Gilfanov M., Churazov E., Revnivtsev M., 1999, A&A, 352, 182

Gilfanov M., Revnivtsev M., Molkov S., 2003, A&A, 410, 217

Gilfanov M., Revnivtsev M., Sunyaev R., Churazov E., 1998, A&A, 338, L83

Gottwald M., Haberl F., Langmeier A., Hasinger G., Lewin W. H. G., van Paradijs J., 1989, ApJ, 339, 1044

Grevesse N., Sauval A. J., 1998, Space Sci. Rev., 85, 161

Grindlay J., Gursky H., Schnopper H., Parsignault D. R., Heise J., Brinkman A. C., Schrijver J., 1976, ApJ, 205, L127

Gursky H., Giacconi R., Paolini F. R., Rossi B. B., 1963, Physical Review Letters, 11, 530

Hansen C. J., van Horn H. M., 1975, ApJ, 195, 735

Homer L., Anderson S. F., Margon B., Deutsch E. W., Downes R. A., 2001, ApJ, 550, L155

Homer L., Anderson S. F., Wachter S., Margon B., 2002, AJ, 124, 3348

Iben, Jr. I., 1983, ApJ, 275, L65

Iben, Jr. I., Tutukov A. V., 1985, ApJS, 58, 661

Iben, Jr. I., Tutukov A. V., 1987, ApJ, 313, 727

Iben, Jr. I., Tutukov A. V., Yungelson L. R., 1995, ApJS, 100, 233

Inogamov N. A., Sunyaev R. A., 1999, Astronomy Letters, 25, 269

in't Zand J. J. M., Cumming A., van der Sluys M. V., Verbunt F., Pols O. R., 2005, A&A, 441, 675

Jahoda K., Swank J. H., Giles A. B., Stark M. J., Strohmayer T., Zhang W., Morgan E. H., 1996, in Society of Photo-Optical Instrumentation Engineers (SPIE) Conference Series, Vol. 2808, EUV, X-Ray, and Gamma-Ray Instrumentation for Astronomy VII, Siegmund O. H., Gummin M. A., eds., pp. 59–70

Jain C., Paul B., Dutta A., 2010, MNRAS, 403, 920

Jansen F. et al., 2001, A&A, 365, L1

Jonker P. G., Nelemans G., 2004, MNRAS, 354, 355

Jonker P. G. et al., 2001, ApJ, 553, 335

Juett A. M., Chakrabarty D., 2003, ApJ, 599, 498

Juett A. M., Chakrabarty D., 2005, ApJ, 627, 926

Juett A. M., Chakrabarty D., 2006, ApJ, 646, 493

Juett A. M., Psaltis D., Chakrabarty D., 2001, ApJ, 560, L59

Kalberla P. M. W., Burton W. B., Hartmann D., Arnal E. M., Bajaja E., Morras R., Pöppel W. G. L., 2005, A&A, 440, 775

Kaplan D. L., Bildsten L., Steinfadt J. D. R., 2012, ApJ, 758, 64

Kawaler S. D., 1995, in Saas-Fee Advanced Course 25: Stellar Remnants, Benz A. O., Courvoisier T. J.-L., eds., p. 1

Klein O., Nishina T., 1929, Zeitschrift fur Physik, 52, 853

Knoll G. F., 2000, Radiation detection and measurement

Koliopanos F., Gilfanov M., Bildsten L., 2013, MNRAS, 432, 1264

Koliopanos F., Gilfanov M., Bildsten L., Trigo M. D., 2014, MNRAS, 442, 2817

Krauss M. I., Schulz N. S., Chakrabarty D., Juett A. M., Cottam J., 2007, ApJ, 660, 605

Kuulkers E., den Hartog P. R., in't Zand J. J. M., Verbunt F. W. M., Harris W. E., Cocchi M., 2003, A&A, 399, 663

Kuulkers E. et al., 2010, A&A, 514, A65

Laor A., 1991, ApJ, 376, 90

Lasota J.-P., 2001, New A Rev., 45, 449

Levine A. M., Bradt H., Cui W., Jernigan J. G., Morgan E. H., Remillard R., Shirey R. E., Smith D. A., 1996, ApJ, 469, L33

Lewin W. H. G., van Paradijs J., van den Heuvel E. P. J., 1995, X-ray Binaries

Lightman A. P., White T. R., 1988, ApJ, 335, 57

Linares M. et al., 2012, ApJ, 760, 133

Lodenquai J., Canuto V., Ruderman M., Tsuruta S., 1974, ApJ, 190, 141

Madej O. K., Garcia J., Jonker P. G., Parker M. L., Ross R., Fabian A. C., Chenevez J., 2014, ArXiv e-prints

Madej O. K., Jonker P. G., Fabian A. C., Pinto C., Verbunt F., de Plaa J., 2010, MNRAS, 407, L11

Markwardt C. B., Juda M., Swank J. H., 2003, The Astronomer's Telegram, 127, 1

Martin-Carrillo A. et al., 2012, A&A, 545, A126

Matt G., Fabian A. C., Ross R. R., 1993, MNRAS, 262, 179

Mészáros P., 1992, High-energy radiation from magnetized neutron stars.

Middleditch J., Mason K. O., Nelson J. E., White N. E., 1981, ApJ, 244, 1001

Murray S. S. et al., 1997, in Society of Photo-Optical Instrumentation Engineers (SPIE) Conference Series, Vol. 3114, EUV, X-Ray, and Gamma-Ray Instrumentation for Astronomy VIII, Siegmund O. H., Gummin M. A., eds., pp. 11–25

Nagel W., 1981, ApJ, 251, 288

Naik S., Paul B., 2003, A&A, 401, 265

Nayakshin S., Kazanas D., Kallman T. R., 2000, ApJ, 537, 833

Nelemans G., 2005, in Astronomical Society of the Pacific Conference Series, Vol. 330, The Astrophysics of Cataclysmic Variables and Related Objects, Hameury J.-M., Lasota J.-P., eds., p. 27

Nelemans G., Jonker P. G., Marsh T. R., van der Klis M., 2004, MNRAS, 348, L7

Nelemans G., Jonker P. G., Steeghs D., 2006, MNRAS, 370, 255

Nelemans G., Yungelson L. R., van der Sluys M. V., Tout C. A., 2010, MNRAS, 401, 1347

Nelson L. A., Rappaport S. A., Joss P. C., 1986, ApJ, 311, 226

Ng C., Díaz Trigo M., Cadolle Bel M., Migliari S., 2010, A&A, 522, A96

Orlandini M. et al., 1998, ApJ, 500, L163

Paerels F. et al., 2001, ApJ, 546, 338

Pandey G., Kameswara Rao N., Lambert D. L., Jeffery C. S., Asplund M., 2001, MNRAS, 324, 937

Papitto A., Di Salvo T., D'Aì A., Iaria R., Burderi L., Riggio A., Menna M. T., Robba N. R., 2009, A&A, 493, L39

Paquette C., Pelletier C., Fontaine G., Michaud G., 1986, ApJS, 61, 197

Paul B., Agrawal P. C., Rao A. R., Manchanda R. K., 1996, Bulletin of the Astronomical Society of India, 24, 729

Paul B., Agrawal P. C., Rao A. R., Manchanda R. K., 1997, A&A, 319, 507

Paul B., Dotani T., Nagase F., Mukherjee U., Naik S., 2005, ApJ, 627, 915

Piraino S., Santangelo A., Ford E. C., Kaaret P., 1999, A&A, 349, L77

Podsiadlowski P., Rappaport S., Pfahl E. D., 2002, ApJ, 565, 1107

Popham R., Sunyaev R., 2001, ApJ, 547, 355

Pozdnyakov L. A., Sobol I. M., Sunyaev R. A., 1983, Astrophysics and Space Physics Reviews, 2, 189

Rappaport S., Joss P. C., 1984, ApJ, 283, 232

Rappaport S., Markert T., Li F. K., Clark G. W., Jernigan J. G., McClintock J. E., 1977, ApJ, 217, L29

Rea N., Israel G. L., Di Salvo T., Burderi L., Cocozza G., 2004, A&A, 421, 235

Revnivtsev M., Gilfanov M., Sunyaev R., Jahoda K., Markwardt C., 2003, A&A, 411, 329

Revnivtsev M., Sazonov S., Gilfanov M., Churazov E., Sunyaev R., 2006, A&A, 452, 169

Ritossa C., Garcia-Berro E., Iben, Jr. I., 1996, ApJ, 460, 489

Roelofs G. H. A., Groot P. J., Nelemans G., Marsh T. R., Steeghs D., 2006, MNRAS, 371, 1231

Ross R. R., Fabian A. C., 1993, MNRAS, 261, 74

Rothschild R. E. et al., 1998, ApJ, 496, 538

Savonije G. J., de Kool M., van den Heuvel E. P. J., 1986, A&A, 155, 51

Schatzman E. L., 1958, White dwarfs

Schönherr G., Wilms J., Kretschmar P., Kreykenbohm I., Santangelo A., Rothschild R. E., Coburn W., Staubert R., 2007, A&A, 472, 353

Schulz N. S., Chakrabarty D., Marshall H. L., Canizares C. R., Lee J. C., Houck J., 2001, ApJ, 563, 941

Schulz N. S., Nowak M. A., Chakrabarty D., Canizares C. R., 2010, ApJ, 725, 2417

Shahbaz T., Watson C. A., Zurita C., Villaver E., Hernandez-Peralta H., 2008, PASP, 120, 848

Shakura N. I., Sunyaev R. A., 1973, A&A, 24, 337

Shull J. M., van Steenberg M., 1982, ApJS, 48, 95

Smale A. P., Mason K. O., White N. E., Gottwald M., 1988, MNRAS, 232, 647

Strohmayer T., Bildsten L., 2006, New views of thermonuclear bursts, Lewin W. H. G., van der Klis M., eds., pp. 113–156

Strüder L. et al., 2001, A&A, 365, L18

Sunyaev R. A., Shakura N. I., 1986, Soviet Astronomy Letters, 12, 117

Sunyaev R. A., Titarchuk L. G., 1980, A&A, 86, 121

Tanaka Y., 1986, in Lecture Notes in Physics, Berlin Springer Verlag, Vol. 255, IAU Colloq. 89: Radiation Hydrodynamics in Stars and Compact Objects, Mihalas D., Winkler K.-H. A., eds., p. 198

Torrejón J. M., Schulz N. S., Nowak M. A., Kallman T. R., 2010, ApJ, 715, 947

Turner M. J. L. et al., 2001, A&A, 365, L27

Tutukov A. V., Yungelson L. R., 1993, Astronomy Reports, 37, 411

van der Klis M., Swank J. H., Zhang W., Jahoda K., Morgan E. H., Lewin W. H. G., Vaughan B., van Paradijs J., 1996, ApJ, 469, L1

van Haaften L. M., Voss R., Nelemans G., 2012, A&A, 543, A121

van Paradijs J., McClintock J. E., 1994, A&A, 290, 133

Verbunt F., van den Heuvel E. P. J., 1995, X-ray Binaries, 457

Verbunt F., Wijers R. A. M. J., Burm H. M. G., 1990, A&A, 234, 195

Verner D. A., Ferland G. J., Korista K. T., Yakovlev D. G., 1996, ApJ, 465, 487

Walter F. M., Mason K. O., Clarke J. T., Halpern J., Grindlay J. E., Bowyer S., Henry J. P., 1982, ApJ, 253, L67

Wang Y.-M., Frank J., 1981, A&A, 93, 255

Werner K., Nagel T., Rauch T., Hammer N. J., Dreizler S., 2006, A&A, 450, 725

White N. E., Swank J. H., Holt S. S., 1983, ApJ, 270, 711

White T. R., Lightman A. P., Zdziarski A. A., 1988, ApJ, 331, 939

Wijnands R., van der Klis M., 1998, Nature, 394, 344

Wolter H., 1952, Annalen der Physik, 445, 94

Yungelson L. R., Nelemans G., van den Heuvel E. P. J., 2002, A&A, 388, 546

Zhong J., Wang Z., 2011, ApJ, 729, 8

Zycki P. T., Krolik J. H., Zdziarski A. A., Kallman T. R., 1994, ApJ, 437, 597

# Thanks

This work is dedicated to my loving parents Panagioti and Panagiota and my beloved wife Myriam. I would not be here if it wasn't for them.

I would like to thank Rashid Sunyaev for giving me the opportunity to become part of his group and for his constant and warm support.

And last but definitely not least, I would like to express my deepest gratitude to my supervisor Marat Gilfanov. He has been a source of inspiration, a great motivator and a fantastic teacher. Interacting with Marat the past 3.5 years, I have watched myself evolve both as a scientist and a person. He will always be close to my heart.

# Lebenslauf

Filippos Koliopanos

2011 – 2015   PhD, Max Planck Institute for Astrophysics

Dissertation title: X-ray diagnostics of ultra compact X-ray binaries

Research supervisors: Marat Gilfanov
Rashid Sunyaev

2008 – 2011   Msc, University of Athens - Athens Observatory, Greece

Thesis title: Monte Carlo simulation of absorption and
scattering processes in the torus of obscured AGN.

Research supervisor: Apostolos Mastichiadis

2004 – 2008   Bsc, University of Athens, Greece

Majored in Astrophysics, Astronomy and Mechanics.